NUMERICAL GAUGE / GRAVITY DUALITY

Disorder in strongly coupled matter

Mario Araújo Edo

München 2015

NUMERICAL GAUGE / GRAVITY DUALITY

Disorder in strongly coupled matter

Dissertation
an der Fakultät für Physik
der Ludwig–Maximilians–Universität
München

vorgelegt von
Mario Araújo Edo
aus Barcelona

München, den 30.09.2015

Dissertation

an der Fakultät für Physik
der Ludwig-Maximilians-Universität München
vorgelegt von Mario Araújo Edo
aus Barcelona am 30. September 2015.

Erstgutachter: Prof. Dr. Johanna Erdmenger

Zweitgutachter: Prof. Dr. Dieter Lüst

Tag der mündlichen Prüfung: 16. November 2015

Max-Planck-Institut für Physik,
München, den 30. September 2015.

Zusammenfassung

In der vorliegenden Dissertation werden elektrische Eigenschaften stark gekoppelter Systeme in Anwesenheit von Störungen untersucht. Dies erfolgt anhand der Dualität zwischen Eich- und Gravitationstheorien, die eine Beschreibung solcher Systeme mittels einer schwach gekoppelten Gravitationstheorie ermöglicht. Besondere Aufmerksamkeit wird hierbei der Berechnung von Ladungsdichten und Leitfähigkeiten gewidmet, sowie der Untersuchung der von den Störungen hervorgerufenen Auswirkungen auf diese.

Unseren Rechnungen liegt die AdS/CFT-Korrespondenz zugrunde. Diese besagt, dass konforme Quantenfeldtheorien im flachen Minkowskiraum höherdimensionalen Stringtheorien im Anti-de-Sitter Raum gleichzusetzen sind. Einen besonders interessanten Grenzfall stellt der Limes dar, in dem die Quantenfeldtheorie einer sehr stark gekoppelten mit vielen internen Freiheitsgraden ausgestatteten Eichsymmetrie unterliegt. Die duale Stringtheorie kann in diesem Falle zu einer klassischen Gravitationstheorie im Anti-de-Sitter Raum vereinfacht werden. Ein relevantes Merkmal, aus dem der große praktische Wert der Dualität entspringt, liegt hierbei in der Tatsache, dass aus schwach gekoppelten Gravitationstheorien stammende Ergebnisse im Rahmen stark gekoppelter Quantenfeldtheorien interpretierbar sind. Angesichts des hohen technischen Schwierigkeitsgrades, den stark gekoppelte Theorien aufweisen, macht diese Eigenschaft die Dualität zu einem mächtigen mathematischen Werkzeug hinsichtlich eines besseren Verständnisses der Physik letzterer.
Trotz fehlendem formellem Beweis ihrer allgemeinen Gültigkeit hat die AdS/CFT-Korrespondenz im Laufe der letzten Jahre wichtige Fortschritte in diesem Zusammenhang zuwege gebracht. Hervorzuheben sind Berechnungen von Transportkoeffizienten stark gekoppelter Theorien wie Viskositäten, Leitfähigkeiten und Diffusionskonstanten.

Störungen treten in realen physikalischen Systemen immer auf. Jedoch ist wenig über deren Auswirkungen auf stark gekoppelte Materie bekannt. Die AdS/CFT-Korrespondenz ebnet den Weg zu einem besseren Verständnis hiervon.

Um den Einfluß von Unreiheiten auf die oben genannten Transporteigenschaften stark gekoppelter Systeme mithilfe der AdS/CFT-Korrespondenz zu untersuchen muss die Abhängigkeit der Felder von mindestens zwei Koordinaten vorausgesetzt werden. Die zugehörigen Bewegungsgleichungen sind partielle Differentialgleichungen, deren analytische Handhabung technisch nicht durchfürchbar ist. Rechnergestützte numerische Methoden stellen die einzige Möglichkeit dar, diesem Problem beizukommen. Besonders geeignet hierfür erweisen sich die sogenannten Spektralmethoden, deren Anwendung auf Rechnungen im Rahmen der AdS/CFT-Korrespondenz in Detail erläutert wird.

In der vorliegenden Arbeit bedienen wir uns der oben erwähnten Methoden, um numerische Lösungen von Gravitationstheorien zu ermitteln, die aufgrund der Dualität inhomogenen stark gekoppelten Systemen fundamentaler Teilchen entsprechen. Die Störungen, deren Auswirkungen auf die Transporteigenschaften des dualen Systems zu untersuchen sind, werden durch eine nichttriviale räumliche Struktur von physikalischen Größen der Gravitationstheorie eingeführt. Diese wird in einer ersten Ausführung von einem stufigen raumabhängigen Massenprofil dargestellt, das eine lokalisierte Störung in Form einer Grenzoberfläche bildet. Der Analyse der resultierenden Ladungsdichten und Leitfähigkeiten kann entnommen werden, dass die Präsenz der Grenzoberfläche eine Lokalisierung der Ladungsdichte in derer unmittelbaren Umgebung bewirkt. Des Weiteren wird eine lokale Erhöhung der Leitfähigkeit bei niedrigen Frequenzen in der zur Grenzoberfläche parallelen Richtung festgestellt. In der senkrechten Richtung nimmt die Leitfähigkeit bei niedrigen Frequenzen einen konstanten Wert an und wird in Vergleich zur parallelen Richtung abgeschwächt. Das Hochfrequenzverhalten der Leitfähigkeiten in beiden Richtungen wird nicht von der Inhomogenität gestört und weist keine Unterschiede auf.
In einem zweiten Fall wird die nichttriviale räumliche Struktur in Form einer zufälligen Raumabhängigkeit des chemischen Potenzials entlang einer Richtung eingeführt, die die Störungen in der lokalen Energie der Ladungsträger nachbildet. Dabei wird festgestellt, dass diese Art von delokalisierten Störungen ein globales Anwachsen der Ladungsdichte des Systems herbeiführt. Die Leitfähigkeit wird von den Störungen abgeschwächt und ihr Verhalten weist qualitative Übereinstimmung mit Modellen der Transporteigenschaften von Graphen in der Physik der kondensierten Materie.

Resumen

En la presente tesis se estudian propiedades eléctricas de sistemas fuertemente acoplados en presencia de desorden. Dicho estudio se lleva a cabo mediante la dualidad entre teorías de gauge y teorías de gravedad que posibilita una descripción de tales sistemas en términos de una teoría de gravedad con acople débil. Reciben especial atención el cálculo de densidades de carga y de conductividades, así como el análisis de los efectos provocados por el desorden sobre ellas.

Nuestros cálculos se basan en la correspondencia AdS/CFT. Ésta establece la equivalencia entre teorías cuánticas de campos conformes en espaciotiempos planos de Minkowski y teorías de cuerdas en espacios Anti de Sitter con un mayor número de dimensiones. Un caso límite particularmente interesante es aquél en el que la teoría cuántica de campos está muy fuertemente acoplada y regida por una simetría interna de gauge con muchos grados de libertad. La teoría gravitacional dual puede en este caso reducirse a una teoría clásica de gravedad en un espacio Anti de Sitter. Una característica destacable, de la cual se deriva la gran utilidad práctica de la dualidad, radica en la posibilidad de interpretar resultados procedentes de teorías gravitacionales con acople débil en el marco de teorías cuánticas de campos con acople fuerte. Dadas las dificultades técnicas ligadas a las teorías fuertemente acopladas, esta propiedad hace de la dualidad una poderosa herramienta matemática de cara a un mejor entendimiento de la física de tales teorías.
Aún a falta de pruebas formales de su validez general, la correspondencia AdS/CFT ha posibilitado en los últimos años avances importantes en este contexto. Cabe destacar el cálculo de coeficientes de transporte de teorías con acople fuerte tales como viscosidades, conductividades y constantes de difusión.

A pesar de ser un rasgo común de sistemas reales, se sabe bien poco acerca de los efectos que el desorden tiene sobre la materia fuertemente acoplada. La correspondencia AdS/CFT abre por ello la puerta a una mejor comprensión de éstos.
El estudio del efecto de las impurezas sobre las mencionadas propiedades de

transporte en sistemas con acople fuerte mediante la correspondencia AdS/CFT implica la dependencia de los campos de al menos dos coordenadas. Las ecuaciones de movimiento resultantes son ecuaciones diferenciales parciales, cuyo tratamiento analítico resulta técnicamente irrealizable. El uso de técnicas numéricas computacionales supone la única posibilidad de atacar este problema. Especialmente adecuados para tales fines resultan ser los conocidos como métodos espectrales, cuya aplicación a cálculos en el marco de la dualidad AdS/CFT presentamos detalladamente.

En la presente tesis nos servimos de los métodos arriba mencionados para hallar soluciones numéricas de teorías gravitacionales que son mediante la dualidad equivalentes a teorías cuánticas de campos inhomogéneas y fuertemente acopladas de partículas fundamentales. Las impurezas, cuyos efectos sobre las propiedades de transporte del sistema dual se desea analizar, se introducen mediante una estructura espacial no trivial de las cantidades físicas de la teoría de gravedad. Ésta viene representada en una primera realización por un perfil de masas con una dependencia espacial en forma de escalón que constituye una impureza localizada en la forma de una interfaz. El estudio de la densidad de carga y las conductividades resultantes revela que la presencia de la interfaz induce una localización de la densidad de carga en las inmediaciones de aquélla. Así mismo se observa que la presencia del perfil de masas inhomogéneo considerado provoca un incremento local de la conductividad a bajas frecuencias en la dirección paralela a la interfaz. En la dirección perpendicular a ella la conductividad a bajas frecuencias adquiere un valor constante y se ve debilitada en comparación a la dirección paralela. El comportamiento a altas frecuencias de ambas conductividades no se ve afectado por la inhomogeneidad y no se aprecian diferencias entre ellas.
En un segundo caso la estructura espacial no trivial viene introducida mediante una dependencia espacial aleatoria del potencial químico en una dirección que reproduce el desorden en la energía local de los portadores de carga. En este caso se advierte que este tipo de impureza deslocalizada provoca un crecimiento global de la densidad de carga del sistema. La conductividad se ve debilitada por el desorden y su comportamiento coincide cualitativamente con modelos sobre las propiedades de transporte del grafeno en física de la materia condensada.

Abstract

In this thesis electrical properties of strongly coupled systems are studied in the presence of disorder. This is done by means of the duality between gauge theories and gravity theories, which allows a description of such systems in terms of a weakly coupled gravity theory. Special attention is devoted to the computation of charge densities and conductivities as well as to the analysis of the effects triggered by the disorder upon these.

Our computations are based on the AdS/CFT correspondence. It establishes that conformal quantum field theories in flat Minkowski space are equivalent to string theories in a higher dimensional Anti-de-Sitter space. A particularly interesting extremal case is given by the limit in which the quantum field theory is underpinned by a very strongly coupled gauge symmetry with great many internal degrees of freedom. In that case the dual string theory may be simplified to a classical theory of gravity in Anti-de-Sitter space. A remarkable feature hereof giving rise to the great practical value of the duality is the fact that results stemming from a weakly coupled theory of gravity find an interpretation within a strongly coupled quantum field theory. Given the technical difficulties inherent to strongly coupled theories, this property renders the duality a powerful mathematical tool with regard to the physics of the latter.
Despite lacking formal proofs of its general validity, during the last years the AdS/CFT correspondence has brought about important progresses in this context. The computation of transport coefficients in strongly coupled theories such as viscosities, conductivities and diffusion constants are some examples worth emphasising.

In spite of its being a common feature in real world systems, little is known about the effects disorder has on strongly coupled matter. The AdS/CFT correspondence paves the way to a better understanding thereof.
The study of the effects of impurities upon the transport properties mentioned above in strongly coupled systems by means of the AdS/CFT correspondence implies the dependence of the fields on at least two coordinates. The resulting equations of motion are partial differential equations, whose analytical treat-

ment is technically unfeasible. The use of computational numerical techniques provides the only way of attacking this problem. The so-called spectral methods turn out to be specially well-suited for this purpose. We cover in detail their application to computations within the AdS/CFT correspondence.

In the present thesis we make use of the mentioned methods to find numerical solutions to gravity theories which correspond via the duality to inhomogeneous strongly coupled systems of fundamental particles. The disorder, whose effects upon the transport properties of the dual system are to be analysed, is introduced by a non-trivial spatial structure of physical quantities in the gravity theory. This is given in a first realisation by a step-like spatially dependent mass profile which constitutes a localised impurity in the form of an interface. The study of the resulting charge density and conductivities reveals that the presence of the interface induces a localisation of the charge density in its vicinity. Furthermore, a local increase of the conductivity at low frequencies in the direction parallel to the interface caused by the presence of the interface is observed. In the direction transverse to it the conductivity at low frequencies takes a constant value and is supressed in comparison to the parallel direction. The high frequency behaviour of both conductivities is not affected by the inhomogeneity and no differences between them are found.
In a second case the non-trivial spatial structure is introduced by a random spatial dependence of the chemical potential along a differentiated direction that mimics disorder in the on-site energy of the charge carriers. In this case it is observed that this kind of impurity leads to a global enhancement of the charge density of the system. The conductivity is suppressed by the disorder and its behaviour displays qualitative agreement with models within condensed matter physics for the transport properties of graphene.

Contents

Chapter 1

Introduction

String theory is nowadays one of the most promising candidates to a theory accounting for all interactions we observe in nature, including gravity. How can such a fundamental theory be employed to explore the properties of strongly coupled matter in the presence of impurities or disorder? What is the sense of such an unexpected usage? We would like to take the reader on a trip through the beauties of theoretical physics whose final stop shall be an answer to this question.

In this first chapter we present a review of the current state of fundamental physics concerning its current goals, still unaccomplished aims and successful achievements. It is aimed at non-specialised readers and no technical skills are required to read it in accordance with the author's opinion that science should be made as accessible as possible to the broad public. It reflects to some extent the personal opinion of the author on the different topics and is therefore subject to criticism and disagreement. The reason why we start with such a general introduction is so as to provide a logical access to the line of reasoning that allows for an answer to the question risen in the previous paragraph. A more technical introduction to this thesis is presented in chapter 2.

1.1 What is physics?

About three million years ago a spectacular process of far-reaching consequences for the human race was set in motion for which no scientific explanation has yet been found. The development of the brain became one of the most remarkable traits of our biological evolution up to present days. As it seems, this evolution was not just driven by the need to adapt to a changing environment. Many other species have successfully adapted to varying life conditions without having to resort to an explosively fast evolving brain. Evolution gave other animals a sharp vision, a great strength or a dazzling sense of smell. We humans were blessed with a powerful mind. As a result of this

we evolved to become beings not just able to master our ecosystem in order to survive but also capable of abstract thinking. In the course of time, we stopped seeing nature as a mere source of the necessary nutrients for life and of regrettable deadly threats to avoid. We began to feel the urge to render that entire environment around us understandable to our mind. We started asking ourselves questions about things. That mixture of seemingly unjustified biological capacity and emergent inherent curiosity derived into what we nowadays call physics.

Physics is an attempt to describe how nature works. Emphasis should be made in the use of an indeterminate article as well as in the words *describe* and *how*. A description does not always comprise an explanation, nor does it imply a justification. A *how* question is essentially different to a *what* or a *why* question. Physics, as we understand it nowadays, is not about why nature works or what it ultimately is but rather about how it works and about how we can understand the regular patterns we observe in it. Physicists try to make use of these regularities to establish models of the universe. At the most fundamental level, this comprises the elementary components of matter and the interactions they are subject to.
Since the formulation of physical laws is based on the recognition of regularity patterns, we resort to the most eminent case of a general language to express objective regularities. This is the language of mathematics. Whenever a scientist wishes to formulate a law, that means that they want to make a statement as general and broad as possible about how things work. This requires a minimum degree of universality, for a law cannot be called such if it needs to be applied in a distinct way to each particular case. Whenever universality comes into play, mathematics arises as the natural tool to resort to. A mathematical statement is by definition one which applies to any element of its domain of validity.
Whether mathematics is an objective truth in the platonic sense [1], with an existence not dependent on the presence of any conscious observer to appreciate its beauties or if, as naturalism defends, it is a creation of the human mind due to its very structure [2] remains an interesting ongoing discussion among philosophers of science. Be it as it may, the power of mathematics along these lines is incontestable. As it is its capacity to flourish by itself to evolve later on to more and more complex sub-disciplines and to find applications within the most different fields of knowledge. It is what Wigner called the unreasonable effectiveness of mathematics [3]. The question about its ultimate character remains a mystery and is one that escapes for the time being the realm of physically addressable questions. Interesting and legitimate as they are, questions like this, together with the ones about the meaning of existence, the distinction between good and evil, the possibility of a God in any of its versions or the true sense of life are intrinsically impossible to address through the methods of the physical sciences. It is so due to the impossibility

of putting any thinkable answers to the validity test of experience, on which natural sciences ultimately rely.

What renders physics distinct as a method to explore reality is indeed, apart from the universality of its mathematical character, the solidity provided by the validity criterion of observational experience.
The requirement that the consequences of a predicted scientific model be observed experimentally creates the need for a rubbish bin in the office of a theoretical physicist as opposed to that of a philosopher. It provides us with a convenient criterion to tell scientifically acceptable theories from non-acceptable ones. While it is by no means true that human sensory experience is always a reliable validity criterion, we must concede that we do not have many other possibilities to put reasonable limits to our abstraction. It is a guiding principle in modern physics that theories which are contradicted by experiment be declared invalid. On the same grounds, a theoretical model which cannot possibly be experimentally tested by any means is not considered to be a scientifically valid theory.

Scientific progress is mostly achieved by a mixture of experimental evidence and theoretical looking ahead. Mostly several rebounds and retries are needed until a theory is finally satisfactory enough to be accepted. Theory and experiment are interwoven. They backreact upon each other and guide us towards scientific advances. Sometimes, unexpected experimental results might lead to new theoretical perspectives. In other occasions, the beauty and elegance of a given theoretical model can suggest experimentalists which evidences to look for. True physics can only evolve when both theory and experiment agree. A single rigorous experimental contradiction suffices to throw overboard an entire theoretical model, beautiful and elegant as it may be. Good examples of mathematically elegant theories that have been discarded due to the lack of experimental evidences in its favour are the symmetric Maxwell equations with magnetic monopoles and great unification theories using the $SO(10)$ group. Instead, in other occasions it is mathematical elegance what paves the way to a successful theory and to the corresponding experimental results. The most eminent example is probably Einstein's theory of general relativity.
In fundamental physics this interplay between experiment and theory has been guided by the latter for a long time now. Experimentalists focus their attention towards the empirical confirmation of theoretically predicted models. These are somewhat directed by aesthetic criteria. A theory is said to be beautiful when it can be reduced to simple equations which apply to as general a field as possible.

The possibility of trading the object of a mathematical statement by another is called symmetry. Symmetry is thus the most key concept in our fundamental description of nature. Indeed whether we should talk about laws of nature

or rather just about symmetries seems to be a matter of controversy among philosophers of science [4, 5]. Whatever the case is, it is through the concept of symmetry that laws about the working principles of the universe can be formulated.

1.2 Symmetry

Symmetry allows to exchange the objects to which a law is applied, giving rise to the objectivity of the law and the possibility of classifying or labelling objects with regard to it. This general interpretation of symmetry has a particular realisation in physics which acts as a cornerstone of our entire comprehension of nature.
In physics, a symmetry is a transformation that can be made to a system without changing the outcomes of physical observation. The laws of physics should be the same no matter how the phenomena are described. Simple as it may sound, this assertion reveals itself as a really powerful and profound one. It was probably Einstein who first eminently profited from his belief in such important a role for symmetry. In a sense, he changed the way physics is done by bringing his theory of relativity into being basing it on symmetry considerations, namely on the beautiful assumption that the laws of physics may not depend on the observer. The confirmation of some of the predictions of the theory of relativity, like the deviation of Mercury's perihelion, sealed the success of the principle. Later on Emmy Noether proved her celebrated theorem connecting symmetry to conserved quantities. According to it, every continuous symmetry in physics allows to define a quantity which is conserved in time. It is through Noether's theorem that we now know that conserved quantities usually mentioned in everyday life such as "energy" or "charge" are a consequence of symmetry. By then, the paradigm had already been changed. Symmetries were no longer seen as a special property of some of the laws of physics. It is precisely what respects symmetries that we call ever since a law of physics.
Nevertheless, physics remains a science subject to the experimental criterion of validity mentioned above. Observable predictions must be possible. Then they must be observed. Only then is joy allowed to a physicist.

It is in the very concept of symmetry where the entire physical information about a system is contained from a theoretical point of view, namely what forms of matter and energy are present and how they evolve and interact in space-time.
It is by no means exaggerated to state that what the hammer is to the carpenter is the concept of symmetry to the theoretical physicist. Whenever a model is attempted to describe nature, the question about the present symmetries is the first to be posed, for models ought to be as simple and elegant as nature itself allows. Indeed some think that the ultimate goal of physics is the formu-

lation of a universal theory, namely one with no need for external parameters or fine adjusting. Just symmetry as the ultimate essence of the laws of nature.

Symmetries may be classified according to the stage on which they play their role. According to this criterion, in elementary particle theory it is common to distinguish two general types of symmetry: space-time symmetries and internal symmetries.

Space-time symmetries

In high energy physics entities - particles - sharing a given number of properties are called a field. A field might come in several variants according to the different ways of transporting energy and momentum through space-time. Every distinct way that a field can transport energy and momentum in space-time is known as a degree of freedom. We also say that a field may represent several particles, that is one for each distinct way of moving energy in space-time. Space-time symmetries change the mathematical description of space-time itself without affecting the physical output. So for example when the outcome of a measurement does not depend on the precise moment in which it is carried out, we say that translations in time are a symmetry of the system. Analogously, whenever the result of physical measurements is not affected by the precise location in space where the measurement takes place, we talk about spatial translations as of a symmetry of the system.
Once a space-time symmetry of the system has been identified, it might be so that this transformation affects different particles in different ways, even though by definition, the results of physical observation do not vary. So for example it may well be that a particular particle remains unchanged under the transformation, in which case physicists call it scalar. Or maybe it changes the orientation of some physical quantity, like it happens to the photon with its polarisation, which is called a vector particle. This is what is meant by the earlier expression "different ways of transporting energy and momentum in space-time". In the mathematical jargon, particles transforming differently under the same space-time symmetry are said to be transforming in different "representations" of the symmetry group, as it is within group theory where symmetry considerations are realised mathematically.

When formulating general physical laws, we must assume that both translations in time and in space cannot affect the outcome of physical observation, for which both symmetries are often assumed. Furthermore, Einstein taught us through his theory of special relativity that the laws of physics are the same for observers moving with respect to one another at constant velocity and that space and time are actually two sides of the same coin and cannot be understood as separate entities. This is a symmetry which is in fact required in fundamental physics for general formulations about the (3+1)-dimensional

world we perceive. It goes under the name of Poincaré symmetry.
Nonetheless, there exist some physical systems for which such symmetries are not verified. For example, inside a solid material atoms are arranged in a lattice structure which breaks translational symmetry, for not all points of space are equivalent. Only some of them belong to the lattice. In this thesis, such systems, in which translational invariance is broken, will be the main object of our attention.

Internal symmetries

Internal symmetries are not concerned with space-time but with the particles themselves. They relate different ways of mathematically representing the degrees of freedom of the fields, not grouping them according to how they respond to different descriptions of space-time but to how they interact with other particles. So for example, if an experiment can be done with different sets of particles while delivering the same result, there is bound to be an internal symmetry relating the different sets of particles to each other. It is sometimes useful to think of this as a relabelling of the fields, for we are exchanging entities which display identical properties with respect to a given kind of interaction. It is possible though, that two particles behave the same way with respect to a given interaction but react differently by means of another one, which can then be used to tell one particle from the other. We then say that they respectively have equal or different charges under the interaction with respect to which they behave equally, or, recovering the mathematical jargon, that they transform under the same or a different representation of the corresponding symmetry group.
This relabelling of the fields, or transformation in the internal space, may furthermore be applied differently at each point in space-time. The requirement that such local transformations have no effects upon the physical laws is a beautiful symmetric principle known as the "gauge principle", which is the base of our understanding of all interactions among particles we know of.
Thanks to the gauge principle, we have by now quite a good understanding of the kind of interactions to which the fundamental constituents of nature are subject.

It sometimes happens that the number of degrees of freedom of a field does not match the number of components in the mathematical object chosen to describe it. This might be due to the extra components making the description more convenient. For example, even though the photon has just two degrees of freedom or polarisation modes, it is commonly described by a four-component vector. Space-time being four-dimensional, this turns out to make things easier. Still, this adding extra components is just on behalf of convenience and should by no means change the physical content of the theory. Hence there must be a symmetry behind it allowing non-physical information or redundan-

cies to be disposed of. The setting of this overload of information goes under the name of "gauge fixing" and is nothing but a choice among equivalent descriptions of a system. This concept of "gauge fixing" should nonetheless not be confused with the more general "gauge principle" referred to above.

Supersymmetry

According to their space-time symmetry properties, particles may additionally be classified into two general categories: bosons and fermions. Fermions are the elementary matter particles, like the electron or the quarks that make up the protons. Bosons are the particles which mediate the interactions among the fermions, like the photon mediating the electromagnetic interaction. Both families of particles display quite different physical behaviours and have correspondingly a different mathematical treatment for their description.
Fermions underlie the so called Pauli exclusion principle, which states the impossibility of two identical fermions being mathematically represented in exactly the same way, that is being assigned the same descriptive labels, and finding themselves at the same point of space-time. This interesting feature, which is not observed in bosons, is reflected in the mathematical objects that properly describe such a behaviour by a property called anticommutation. We say that two elements commute when they can be exchanged without consequences. Instead, we speak about anticommutation when in the process of exchanging the two elements a minus sign appears, which means that one version of the ordered pair is equal to minus the other version of the ordered pair.
During the second half of the 20th century, it was noticed that the mathematical description of the Poincaré symmetry might be consistently extended to include objects having fermionic properties, namely obeying anticommutation rules. Physically this implies the mixing of bosons and fermions by a symmetry, so that each matter particle is predicted to have a force carrier partner particle, a so-called "superpartner", and *vice versa*, always in fermion-boson pairs. So the electron, being a fermion, should have according to supersymmetry a bosonic partner, the selectron. This applies to all existing particles. The general idea is that the laws of physics are invariant under the swap of matter for force.
Supersymmetry is a beautiful and elegant theoretical consideration. It presents several conceptual advantages and solves some of the open problems of the currently accepted models, which makes it very appealing to theorists. Mathematically, it is a normal thing to expect, for is a natural generalisation of space-time symmetries. Nonetheless, it is facing a major shortcoming for its acceptance: lack of experimental confirmation. No superpartner particles have yet been detected. Nevertheless, because they are predicted by symmetry considerations, superparticles are one of the things scientists are currently looking for.

Symmetry breaking

In some cases, symmetry does not enter the game by being present but rather by being surprisingly absent. A mechanism known as symmetry breaking is as conceptually important as symmetry itself. Symmetry breaking might happen at the level of the equations of motion, that is of the theory itself, in which case we talk about an explicit symmetry breaking. In this thesis we are concerned with systems in which translational symmetry is explicitly broken in a given direction of space-time and about the consequences this may have.
Symmetry may also be broken spontaneously by the ground state, also called vacuum, of the theory. This phenomenon, known as spontaneous symmetry breaking is behind phenomena such as the by now famous Higgs mechanism that explains how the mediators of the electroweak interaction acquire their mass. The question of why a given symmetry spontaneously breaks in a particular way remains a mystery. Physical constants are actually a consequence of symmetries breaking the way they do.
Symmetry breakings are ubiquitous in physics. They somewhat disturb the formal elegance of a theory but produce at the same time predictable phenomena that are in agreement with experiment.

Gravity

As mentioned above, Einstein revealed to us at the beginning of the 20th century that space and time are part of the same entity, space-time, and that observers uniformly moving with respect to one another perceive the same physics. That is part of his theory of special relativity, which is very well integrated into our current models to describe the fundamental constituents of matter or particles. But Einstein actually went far beyond that in the way he changed our view of nature. Some years after publishing the theory of special relativity, he presented a more general version of it, the theory of general relativity. According to it, space-time is not flat but curved and its curvature is determined by its energy and matter content. The key idea here was the realisation that different observers at different points of a curved space-time might use different coordinate systems to describe what they see and still the observed realities must agree to each other. In a sense, it is an extension of the gauge principle we introduced above for the internal field space to the case of space-time.
General relativity produced explanations to various phenomena that were not correctly predicted at the time and was quickly accepted as a valid theory. Nowadays physics undergraduates learn general relativity and are astonished at its beauty. There is no doubt about its validity or its theoretical foundations. Still, it has been impossible this far to bring general relativity and quantum mechanics together in a consistent way, the way it was done with special relativity. Both theories work perfectly separately. Quantum mechanics accounts for the physics of very high energies at a microscopic level whereas

general relativity accounts for the macroscopic phenomena of objects moving at velocities close to that of light, like it is commonly the case in cosmology. Nevertheless, a theory of quantum gravity that combines both is missing and remains one of the biggest challenges of theoretical physics.

Thus our current understanding of nature very much relies upon the concept of symmetry. Our theories are characterised by the global symmetries underpinning them. Matter and energy quanta, namely particles, are classified according to their transformation properties under space-time symmetries and the way they interact with each other is dictated by their different behaviours under the internal symmetries. The intensities of each interaction, which are determined by the constants in the theory, can be mostly derived from symmetry breakings. Gravity itself, despite our problems in conciliating it with the remaining fundamental theories of nature, is purely based on symmetric principles.

Symmetry is a beautiful concept of far-reaching consequences. The belief in it led Einstein to the theory of general relativity, which changed our conception of physics forever. It also led to the hunt and later discovery of the Higgs boson and leads us nowadays to keep seeking supersymmetric particles. It is all motivated by our confidence in the predicting power of our mathematical models of reality. Theorists stick to them once they are formulated until the experimental evidences against their validity are undeniable. No deviation from this method is in sight, since it is by means of this method that the most precise and powerful models of nature mankind ever had have been produced.

1.3 The state of the art

The 20th century was the century of physics. Our vision of the world was substantially changed by the irruption of quantum theory and of relativity. Both new theories introduced deep changes in our conception of reality. They both revealed themselves as more complete theories than the ones we had been using previously while tending to the latter in the corresponding limits. Both theories have also been able to provide very good experimental predictions and have hitherto withstand all tests of their validity based on experimental evidence. The marriage of quantum mechanics and special relativity resulted in the advent of quantum field theory. Despite initial scepticism about its correctness due to internal inconsistencies, quantum field theory managed not only to survive as a model, but to improve and to deliver the most precise predictions of physical measurement human beings have produced. In particular, quantum field theory provides the foundations on which the standard model of particle physics rests. It provides a successful model of nature at the most fundamental level up to energies of around 100 GeV. By combining our entire knowledge about the mathematical structure of nature, high energy physicists

were able to combine the concepts of relativity, quantum theory, symmetry breaking and unification to give rise to a theory that satisfactorily accounts for three of the four known interactions at the most fundamental level. Its latest culmination was the very celebrated discovery of the Higgs boson in 2012 at the Large Hadron Collider at CERN [6, 7]. It confirmed a long-anticipated result based on the concept of spontaneous symmetry breaking that had been theoretically predicted in 1964 by three independent groups: by Robert Brout and François Englert [8], by Peter Higgs [9] and by Gerald Guralnik, C. R. Hagen, and Tom Kibble [10].
All in all, the standard model of particle physics based on quantum field theory has granted us a good command of the electroweak and the strong interaction as well as precise knowledge of the fundamental particles subject to them making up observable matter.

Gravity continues to resist its incorporation to the quantum theory and hence its combination with the standard model of particle physics. Still, since its formulation within the context of Einstein's general theory of relativity in 1915 it has provided a large list of successful predictions and results and has passed all experimental tests it has been subject to. General relativity provides satisfactory theoretical foundations on which to build macroscopic explanations for the behaviour of the physics escaping the quantum regime. A model that has risen in its light to provide a solid theoretical background on which to develop cosmology is the so-called Lambda Cold Dark Matter Model (Lambda-CDM-Model). It gives good account of the main properties of the cosmos that have been observationally established and can consistently incorporate inflation. Inflation is a model suggesting that the universe experienced a phase of exponential expansion right after the Big Bang. It provides explanations to many a cosmological observation and is therefore normally assumed. The Lambda-CDM-Model based on general relativity offers a conceptual ground on which our current understanding of the cosmological structure of the universe rests.

Unification

The history of physics has evolved as an ever-expanding place for symmetry in the understanding of the universe. In a reductionist attempt to simplify the laws that allow us to predict the behaviour of nature we see the ultimate goal of physics in the unification of an ever-larger amount of phenomena under a single theoretical domain. Every time physical phenomena that had previously been assumed to be independent of each other are brought under the same conceptual framework we talk about unification. One of the first relevant examples occurring in physics was the realisation by Newton that the interaction responsible for the fall of objects on Earth is the same that the one governing the orbit of celestial objects. An even more eminent case was the unification by Maxwell of electricity and magnetism under the broader

concept of electromagnetism based on the insight that they are nothing but two manifestations of the same phenomenon, as seen by observers in different reference frames. Such a realisation is mostly triggered by the unveiling of a formerly unknown underlying symmetry that allows to convert between the affected phenomena.

From this reductionist perspective, the natural hope arises that physics be one day culminated by a theory of everything. A theory of everything would unify all fundamental interactions under a single mathematical tenet. It would furthermore reduce to the known theories in the corresponding limits and should not require the introduction by hand of any external parameters.
Whether such a theory shall some day be in reach remains an open question. Whether the mere remote possibility of getting it is worth the effort is beyond any doubt.

The missing pieces

Despite the tremendous success they represent, our most fundamental theories of nature are far from being complete. Both the standard model of particle physics and the Lambda-CDM-Model present a long list of phenomena and facts they provide no explanation for.
The standard model requires the ad-hoc introduction of 18 parameters that must be determined experimentally and inserted into the model. This requires a high degree of fine-tuning and no satisfactory theoretical understanding beyond anthropic arguments is available to justify an apparent conspiration to make the universe we observe possible. It is also unknown why the forces of nature seem to be linked to the symmetry group $U(1) \times SU(2) \times SU(3)$, why we can distinguish three families of fermions and four fundamental interactions or why the scales of masses of the fundamental particles differ by up to five orders of magnitude.
The Lambda-CDM-Model also requires the introduction of external parameters, 6 in total and fails to address the microscopic origin of dark matter and dark energy, which account respectively for 27% and 68% of the content of the universe.
Further aspects of our fundamental understanding of nature not being considered complete comprise the part of the standard model accounting for the strong interaction, namely quantum chromodynamics or QCD. At low energies the coupling constant of QCD becomes large and bound states of the fundamental degrees of freedom of the theory form. Since the coupling is strong, the theory is not accessible through the common perturbative methods used for the electroweak interaction. This is the reason why a complete understanding of the strong interaction, and concretely of the mechanism bounding the fundamental degrees of freedom together, which also goes under the name of confinement, is lacking.

Another side of QCD that currently escapes the domain of our physical understanding due to its strong coupling is the physics of the quark-gluon plasma. It is a newly discovered state of matter arising under extremely high temperatures and baryon densities. Such conditions might have been relevant during the early stages of the universe evolution and are believed to play a role in the physics of heavy ion collisions at large particle accelerators like the LHC and at the interior of neutron stars.
However, QCD is not the only field in which strong coupling impedes a complete command of the underlying physics. The strongly correlated regime of many field theories arising in condensed matter systems cannot be described by the traditional effective theory methods applied to other condensed matter phenomena. Interesting cases of which a full theoretical explanation is lacking comprise high temperature superconductivity [11] and the fractional quantum Hall effect [12].
A further aspect of strongly coupled condensed matter systems for which no satisfactory conceptual framework has been found is that of disordered systems. Disorder is a common feature of real world physical systems but it is not known yet how to model it at strong coupling using conventional field theoretical methods. Such systems are of particular relevance to this thesis.

It is legitimate to also list gravitational waves among the topics predicted by well-established theories which are still awaiting an experimental confirmation. Early celebrations of the results provided by the BICEPS experiment, which contained at first glance the first empirical evidences of gravitational radiation, were later faced with disappointment when the responsible groups professionally admitted that their conclusions were due to systematic errors [13, 14]. The existence of gravitational waves is nonetheless beyond doubt for most theoreticians due to the solid foundation on which it stands namely general relativity. Still, their detection remains an unaccomplished task.

Another piece of the theoretical puzzle which for the moment is not fitting properly is supersymmetry. Experimental evidence of supersymmetry has been sought for many years at the biggest existing testing devices, like the LHC at CERN. So far though, no traces of superparticles have been observed. Both the ATLAS and the CMS experiments have published reviews of the current situation of searches for supersymmetry and the corresponding limits on parameters [15, 16]. Depite all these efforts the search for supersymmetric particles has been fruitless up to date. This however seems not to be an obstacle for theorists, who apart from appreciating the undeniable conceptual appealing of supersymmetry, see in it a tool that enables them to access terrains of mathematics that would otherwise be impenetrable. A good example comes by the hand of another aspect of the current state of the art in theoretical physics falling short of completeness, the aforementioned quantisation of gravity.

1.4 String theory

Probably the most remarkable missing piece in our current understanding of nature is the absence of a complete quantum theory of gravity. The quantisation of space-time reveals itself indeed as an arduous problem which has this far resisted all attempts to approach it from a field theoretical point of view. Gravity adamantly resists quantisation attempts following the path of effective field theories based on the renormalisation group flow. Its coupling constant has positive dimensions and hence render the theory non-renormalisable. Excluding the high energy sector and seeing gravity as an effective theory valid within a given range of energies is an approach falling afoul of fundamentality and is not entirely satisfactory from a conceptual point of view.

String theory is nowadays the most promising candidate to a framework that comprises all known interactions, including gravity, at the quantum level. It includes Einstein's gravity as a limiting case and can furthermore account for the rest of the known interactions. Its main idea is quite a simple one: replacing point particles by extended strings. Yet the consequences of such a seemingly innocent step are far-reaching. Among other things, this has the consequence that the one-dimensional word-lines of traditional particles are replaced by two-dimensional world-sheets. Upon quantisation of these two-dimensional world-sheets a restriction upon the number of space-time dimensions is found. In the presence of supersymmetry, which guarantees the stability of the theory, this number is found to be ten.

Fundamental strings may furthermore have two different topologies according to whether they are open or closed. Open strings are assumed to have their endpoints fixed on surfaces in space-time which go under the name of branes. An open string ending on such an object is seen by an observer whose perspective is limited to the brane as a charged particle sourcing a gauge field. In these regards, the physics of gauge fields accounting for fundamental interactions like the ones known from common quantum field theories unfold within string theory. Closed strings instead are not subject to such boundary conditions and may propagate freely in space-time. They have the relevant property that one of their oscillating modes corresponds to a massless field of spin two, which is interpreted as the graviton, the boson mediating the gravitational force. Hence both the kind of quantum field theories we use in our most precise models of nature and Einstein's theory of gravity seem to be contained within string theory. This is the reason why so many hopes have been put on it as a candidate to a theory describing all known interactions. Yet in order for string theory to be accepted as such further requirements should be fulfilled. Firstly, it ought to reproduce the structure of nature and hence not only contain general quantum field theories but be able to reproduce the standard model of particle physics in particular. The field of research known

as string phenomenology is devoted to seeking connecting threads between string theoretic models and particle physics [17]. Moreover supersymmetry is an essential ingredient of superstring theory. As explained above, the lack of experimental evidences in its favour continues to be an important barrier on the way towards the definitive upgrade of supersymmetry from a useful mathematical tool to a true feature of nature.

In this context it is worth emphasising that string theory may not only be seen as a candidate to a theory of everything. Contrarily to the traditional order of things, string theory has allowed mathematics for the first time to benefit directly from theoretical physics. Along these lines, many see string theory as a mathematical tool that may open new perspectives in our mathematisation of reality irrespective of its capacity to describe physically observable phenomena. A remarkable example of this usefulness is provided by the field of gauge/gravity duality, which lays the theoretical foundations of this thesis.

1.5 Gauge/gravity duality

Towards the end of the 1990s symmetry considerations led to the conjecture that some superstring theories on certain ten-dimensional background geometries are equivalent to supersymmetric gauge theories in a common-life four-dimensional space-time. The conjecture was originally formulated by Juan Martín Maldacena [18] and made precise in technical terms shortly thereafter by Steven Gubser, Igor Klebanov, Alexander M. Polyakov and Edward Witten [19, 20]. Since the mentioned background geometries are those of a so-called *Anti de Sitter* space-time and the supersymmetric gauge theory in four dimensions displays a symmetry known as *conformal symmetry* and may hence be called a conformal field theory, this equivalence was given the name of *AdS/CFT correspondence*. Additionally, given the fact that by its virtue a theory in a higher number of dimensions is mapped to a lower-dimensional one, which is somewhat reminiscent of what an hologram does, the correspondence is sometimes referred to as *holographic* and the entire field of research about its consequences as *holography*.
This conjectured AdS/CFT correspondence caught very quickly the interest of theorists given the many research directions it might make accessible. Firstly, it relates a theory containing gravity, superstring theory, to one in which gravity is not present. Furthermore, the main advantage of the correspondence consists in the fact that it relates both theories in such a way that whenever one of them is in its technically hardest regime to tackle the other one happens to be in the regime in which calculations are most easy to deal with. Hence the equivalence might be used as a dictionary translating between two different equivalent descriptions in two different languages, but turning a difficult description to an easy one and the other way around. The implications of this easy-to-hard translation are many. Most notably the possibility to explore

the not yet understood quantum regime of gravity, mapping it to a tractable quantum field theory, and the feasibility of using the regime in which gravity theories are simple to better understand complicated theories of matter. This thesis explores ways in the latter direction.

When taken to its simplest form via convenient limit cases, restrictions and assumptions, the AdS/CFT correspondence offers a very good playground on which to create models for quantum field theories which are otherwise either impossible or technically very involved to handle. While the resulting physics is sometimes distant from the original rigorous formulation of the correspondence, which is by itself far away enough from being an experimentally testable theory, such toy-models may help grasping some aspects of physics that are not accessible by other means. Examples of this are holographic models for condensed matter physics phenomena our current understanding of which is not yet complete. Some representative instances are theories of strongly coupled matter displaying superconductivity, superfluidity or disorder. This is done with awareness of the leap of faith it implies but in the hope that the produced results contribute to a better understanding of the surveyed theories. In fact, there have already been some results which might be enlightening in this sense. In some cases, the holographic approach to a theory rendered more accessible by specially convenient symmetry considerations might have more of a direct connection to real-world physics than apparent at first glance. This happens whenever the studied properties overlap with the universal behaviour occasionally displayed by field theories, which makes the resulting features independent of the particular regime at which they are found. This means that the properties at hand, addressed by means of gauge/gravity duality, may indeed belong to a class of characteristics common to a broad range of field theories. The most celebrated result in this direction is the computation of the ratio of shear viscosity to entropy density for strongly coupled field theories with a gravity dual [21]

$$\frac{\eta}{s} = \frac{1}{4\pi}\frac{\hbar}{k_B}, \tag{1.5.1}$$

about which more shall be said below. Were any of such results to find experimental confirmation, the physicists community would agree to add it to the list of arguments in favour of string theory as a powerful mathematical tool to further expand our theoretical knowledge about nature.

It is with this idea in mind that AdS/CFT has evolved from a purely theoretical field to a kind of an applied theoretical discipline. Some researchers, to which the author of this thesis counts himself, do not point their work towards an ultimate mathematical proof of the duality. Instead, the correspondence is assumed to work and results extracted from it are applied to different quantum field theories that might be related to real-world physics via the universal behaviours mentioned above. This is done in the hope that

mutual feedback between the duality and the addressed field theories results not only in a better understanding of the duality itself but eventually in useful insights into the physics modelled by those very field theories.
This thesis clearly finds a place inside this kind of research. We benefit from gauge/gravity duality to access information about field theories that would otherwise remain beyond computational reach.

1.6 From fundamental forces to disorder in strongly coupled matter

This is the final station of the trip we promised the reader at the beginning of this chapter. String theory, a theory originally devised to explain just the strong interaction, has evolved into the most promising candidate to a fundamental theory accounting for all interactions present in nature. Furthermore, symmetry considerations within string theory suggest an unexpected aspect through the description of charged extended objects present in it called D-branes. The low energy limit of the theory is conjectured to be physically equivalent to some strongly coupled gauge theories. Such theories might have properties in common with the quantum field theories that govern the strongly coupled regime of matter and might therefore be useful in their exploration.

One of the aspects of strongly coupled theories of matter still awaiting a complete theoretical understanding is disorder. Impurities of all kinds percolate real materials and are a mandatory factor to take into account for condensed matter physicists. Disorder is a very common feature of real world condensed matter systems, which might present different realisations but always implies the breaking of translational symmetry. This effectively gives charge carriers the chance to dissipate energy and allows to access more realistic physics than is reflected by perfectly symmetric systems. Despite its importance, little conceptual command is available about the role of disorder in strongly coupled materials due to the difficulty of modelling it using traditional field theories [22].

Given that the AdS/CFT correspondence connects the strongly coupled regime of some quantum field theories to the tractable weakly coupled regime of gravity, there is legitimate hope that it may lead us to a better understanding of the strongly coupled regime of matter. The scope of this thesis is the employment of the duality so as to gain insights into the physics of strongly coupled matter and in particular into the role played by disorder.
We design theories of gravity such that their interpretation in terms of the corresponding field theories mimics disorder so as to study its effects on the properties of the system.

Chapter 2

Roadmap of this thesis

2.1 The need for numerics

Gauge/gravity duality has been since its formulation object of many studies both from a formal and from an applied point of view. Consequently, most of the problems that can be addressed analytically have already been solved. One of the current trends, specially as far as the applications of the duality are concerned, consists in moving on to more involved models, which require the solution of more complicated equations. This thesis contains some examples of such models. We work with gravity theories whose field theory duals mimic the physics of strongly coupled disorder. The technical difficulty lies in the apparition of complicated systems of coupled partial differential equations triggered by the dependence of fields on at least one spatial coordinate besides the common dependence on the AdS radial coordinate. Very hard as they are to attack analytically, partial differential equations pose the need to resort to numerical methods to explore the solutions to problems involving spatial dependence, such as the ones related to interfaces or impurities we face here.

The use of numerics lets the theorist play being an experimentalist. The procedure to arrive at conclusions might deviate a bit from the common practice in theoretical physics in that it does not only consist in formulating a model and derive results from it by means of analytic calculations. Instead, once the model has been formulated theoretically - mostly so as to emulate the desired physical situation on the field theory side of the duality - numerical calculations follow and results are read out in a rather empirical way. The corresponding theoretical interpretation takes place a posteriori in a manner that resembles the traditional scientific method applied in experimental laboratories.
In this sense, the numerical approach to AdS/CFT is a step towards a test of its predictive power and hence of its validity as a physical theory. All of this is done while taking good notice of the caveat that the direct way from theory to predictability is far too complicated. The technical difficulty of the

theory from which the duality is derived, IIB Supergravity, renders its direct analytical exploration a very involved task. This job is being done by research groups working on string theory phenomenology, see [23] for a good review. The approach followed in the field of applied AdS/CFT is one consisting in assuming the validity of the duality and working in limits that simplify it and make it tractable. While this removes part of its generality, it provides a method to pioneer the exploration of new-land in physical terms, which should by all means be eventually conquered by the incontestable strength of formal mathematical means.

2.2 Motivation

The main motivation of this thesis was the perspective of reaching a better understanding of the role played by disorder and by the associated breaking of translational symmetry in strongly coupled matter by means of the AdS/CFT correspondence. In spite of its undeniable relevance for the understanding of realistic materials, no complete theoretical explanations of disorder are available at the quantum level. The holographic approach may lead to new insights in these regards.
In the first stage, our work was inspired by the conjectures presented in [24], which was at its time a follow-up to the ideas developed in [25, 26]. The basic thought is the use of probe D7-branes with a space-dependent embedding profile that translates into a spatially dependent mass in the dual field theoretical perspective. In particular this spatially varying mass profile interpolates between a constant value M and a localised zero at a given value of the spatial coordinate along which the profile changes, $M(x_0) = 0$. In field theories in the presence of a chemical potential, μ, it is the relationship between μ and M what dictates whether the system has a finite electrical conductivity or not. With this kind of spatially varying embedding it is therefore possible to transit from a conducting system to an isolating one over space. If the spatial profile is sharp enough, the transition is effectively localised in space and the system mimics a conducting interface between two isolating materials.
Topological considerations lead to an interpretation according to which one of said materials is a topological insulator. In our approach, we decided to circumvent the complications linked to the presence of topological terms by using a D5 probe brane instead of a D7-brane to introduce flavour degrees of freedom. While the system has very similar dynamics to the D7-brane case, this has the advantage of not having to take the topological Chern-Simons term of the action into account, since it has a zero contribution. This renders the system much more tractable in computational terms. Under these conditions we are able to compute conductivities for the first time in such systems and compare the results to the expectations based on the theoretical background and to provide a solid framework which could serve as a basis for future similar projects.

A substantial amount of the time invested in this thesis was devoted to the development of the codes aiming at providing numerical solutions to the system of partial differential equations in which the equations of motion of the described systems result. Getting such complicated codes to work properly when starting from scratch is a highly non-trivial task that demands a great deal of dedication and effort. Fortunately our work was rewarded with results. We managed to produce a stable code that solves the equations of motion involved with reasonable speed and provides results in a systematic way. A secondary scope of this thesis is to serve as a handbook to our numerical codes so as to make them accessible to future researchers wishing to further pursue our line of research.

Once the necessary machinery was in good working condition, we set off to exploit the generality of our codes and methods to use them in the resolution of similar systems that reproduce different kind of inhomogeneities. In this case, inspired by previous works analysing the role of disorder in holographic matter [27, 28], we launched a new project in which the inhomogeneities at the brane intersections were no longer localised at a given point but extended along a differentiated direction in a random space-dependent way. We choose a chemical potential with this spatial structure. Since the chemical potential defines the local energy of the charge carriers at different positions, this choice of disorder replicates local disorder in their on-site energy [28]. This is reminiscent of the presence of impurities or noise in real-world condensed matter systems. Similar approaches have been applied in the context of holography by other authors [29, 30, 31].
The disorder introduced in the chemical potential extends to the entire system and in particular to the charge density and the conductivities of the system. The behaviour of the conductivity in such disordered systems was studied holographically in [32], also with the presence of fundamental degrees of freedom introduced by a probe D-brane. The conclusion was drawn there, that random disorder in the charge density increases the conductivity at high temperatures and suppresses it as the temperature goes down.
Additionally, there have been attempts within condensed matter physics to better understand the transport properties of graphene in the presence of charged impurities. Graphene is a natural material to refer to when dealing with the transport properties of strongly coupled materials. At low energies, it is described by a relativistic theory in 2+1 dimensions with a chemical potential and its dynamics can be reproduced holographically [33]. The current models for graphene in condensed matter theory are not universally accepted, nor do they provide an explanation to all experimental observations. The improvement of the existing models for graphene is therefore a relevant goal in condensed matter physics given its theoretical and technological interest.
One of the most studied properties of graphene is its electrical conductivity as

a function of the applied gate voltage, which is directly related to the carrier density [34]. In [35, 36], different models were presented to account for the effect of spatially correlated impurity disorder in two-dimensional graphene layers upon the dependence between the charge density and the conductivity. In our second project we solve gravitational systems that reproduce random disorder in the chemical potential of the system and study its effects on the charge density and the conductivities. We compare our results to the predictions made in the cited works.

Other recent results related to the exploration of holographic systems with translational symmetry breaking and the consequent momentum dissipation by the charge carriers include [37, 38, 39] as well as models of massive gravity [40, 41].

2.3 Results

As main results of this thesis we underline the explicit numerical computation for the first time of charge densities and the related conductivities in systems with a D5 probe brane and a spatially dependent quantities. In a first realisation, the spatial dependence is induced by the spatially varying embedding profile resulting in an interface with differentiated electrical properties in comparison with the rest of the spatial interval. In particular the following results are worth emphasising:

- We compute the charge density of the system and observe that our construction leads to its localisation around the defect interface.

- We compute the AC and DC conductivities both in the direction parallel and transverse to the interface and establish that the presence of the interface affects the low-frequency behaviour of both conductivities in its vicinity, increasing the former and suppressing the latter.

- We obtain an expression for the DC conductivity in the direction transverse to the interface analogous to the ones in [42, 32] that allows for its computation based on background horizon data, thereby rendering the resolution of the equation of motion of the fluctuations unnecessary for this purpose.

- We realise that the low-frequency value of the conductivity at the interface in the direction transverse to it is dominated by the values of M and μ away from the interface, while the conductivity at the interface in the direction parallel to it is determined by the parameter configuration at the interface.

- Furthermore we study the effects of the spatial size of the system upon its electrical properties and the effects sourced by the translational symmetry breaking induced by the interface.

In our second main project we extend our studies to the case in which the inhomogeneity is not given by a localised interface but by a spatial random dependence of the chemical potential along a spatial direction, which mimics the effect of disorder in the on-site energy of real-world materials. We study probe brane systems with such kind of noise for the first time and analysed their electrical properties focusing our attention on the effects of the disorder upon the charge density and the electrical conductivities. We have produced the following results:

- We analyse the effects of the disorder upon the charge density of the system and observe an increase in the mean value of the latter with respect to the homogeneous case. Thus we can assert that the presence of the noise enhances the global charge density of the system.

- We study the dependence of the DC conductivity in the direction along which the disorder extends on the chemical potential, which in our system is related to the temperature, and find good qualitative agreement with the predictions formulated in [32] that random disorder in the charge density increases the conductivity at high temperature and suppresses it as the temperature goes down. We furthermore find that said suppression increases quadratically with the strength of disorder.

- We find a linear relationship between the DC conductivity in the direction along which the disorder extends and the mean charge density of the system. Disorder seems to lead to a sublinear behaviour at high charge densities in this behaviour. These results show qualitative agreement with predictions formulated within condensed matter theory models for the transport properties of graphene reproducing experimental data [35, 36].

2.4 Outline of the thesis

This thesis is structured in two parts. Part I includes a review of gauge/gravity duality in chapter 3. Chapter 4 is devoted to the numerical techniques employed to obtain of our results. Both chapters make special emphasis on those aspects of the respective topics which are most relevant to this thesis but do not go beyond the extent of a review. They contain no original work of the author.
Part II contains the original work of this thesis. It is based on the application of gauge/gravity duality and the numerical techniques covered in part I to address the problem of solving systems of partial differential equations arising

in non-homogeneous systems so as to extract holographic information from them, like charge densities and conductivities. Chapter 5 presents our model of charge localisation at brane intersections. In chapter 6 a different kind of disorder in the form of a random noise is studied. These chapters respectively reflect the content of the author's original work, produced under the supervision of Prof. Dr. Johanna Erdmenger at the Max-Planck-Institute for Physics in Munich, Germany, between October 2012 and September 2015. Both projects were carried out in collaboration with Dr. Daniel Areán and Javier M. Lizana. The work presented in chapter 5 has been published in

- M. Araujo, D. Arean, J. Erdmenger and J. M. Lizana, *Holographic charge localization at brane intersections*, *JHEP* **08** (2015) 146 [1505.05883]

The work presented in chapter 6 is part of an ongoing project which is about to be submitted for publication

- M. Araujo, D. Arean and J. M. Lizana, *Noisy brane intersections*, To appear

In chapter 7 we briefly review the results of our work within the current state of the art and suggest some possible directions of future research.
We have included four appendices. Appendix A is a review of representation theory in the context of Lie algebras. We develop in it the necessary concepts to follow our presentation of supergravity in chapter 3. Appendices B and C present mathematical expressions we did not wish to include in the main body of the text due to its length. Finally in appendix D we present simplified and commented versions of the codes we use in the elaboration of this thesis, which support and enforce our introduction to numerics in chapter 4.

Conventions

Unless otherwise explicitly mentioned, along this thesis we work in units in which the reduced Planck's constant, Boltzmann's constant and the speed of light are all unity, $\hbar = 1$, $k_B = 1$, $c = 1$. We use the Minkowski metric with mainly plus convention.

Part I

Conceptual grounds and numerical tools

Chapter 3

Gauge/gravity duality

It is sometimes possible to establish mathematical relations between seemingly different physical phenomena. When this happens, we recognise in this relation an equivalence of descriptions and hence identify the involved physical phenomena with one another. We then talk about a duality. The most eminent case of a duality might be Maxwell's electrodynamics, based on the realisation that the electric and the magnetic field are actually two different descriptions of one same thing, just depending on the observer's reference frame.

Gauge/gravity duality is an equivalence in this sense between certain quantum field theories in a d-dimensional flat space-time and theories of gravity in a $d+1$-dimensional space-time.
Sometimes dualities may involve equivalent descriptions which prove useful at different physical regimes. Gauge/gravity is such a case. The two equivalent descriptions, a quantum theory of fields and a theory of gravity with one extra dimension, happen to be tractable in different physical situations. In spite of being equivalent descriptions of one and the same thing, one or the other side of the duality may be the most convenient one in a given configuration of the physical system. In particular, in the regime at which the quantum field theory description can be assumed to be strongly coupled, the dual gravity theory description corresponds to a weakly curved space-time, accessible through the common methods of general relativity. This renders gauge/gravity duality a magnificent tool for studying strongly coupled quantum field theories, which are otherwise utterly difficult to tackle. At the same time though, this fact makes a formal proof of the duality extremely difficult to achieve. Such a proof would require computations on both sides of the duality, including the strongly coupled quantum field theory description, in which it is not known how to perform reliable calculations.
Still, since its original formulation in 1997 by Juan Martín Maldacena [18], the duality has seen lots of evidences being collected in its favour. Even though the set of theories accessible through the duality is still quite limited and far from describing any observable physical system, the assumption of its validity

opens the door to capturing some of the features that the accessible theories have in common with the ones describing real world physical systems. This may not only provide further evidence of the correctness of the duality but also expand our knowledge and intuition about important issues at the frontier of the current human understanding of nature.

In this chapter we present the most eminent case of gauge/gravity duality, that is the AdS/CFT correspondence, of which this work is an application. Many good and self-complete reviews of the topic are available [45, 46, 47] so we will focus on showing the basic ideas of the correspondence and on those aspects of it which are most relevant to our work. We begin by reviewing the required ingredients to understand the derivation of the conjectured duality, namely supersymmetric $\mathcal{N} = 4$ super Yang-Mills gauge theory and 10-dimensional supergravity theory. We then go on to present the two equivalent descriptions of the same object, a stack of D3-branes, that motivate the following formulation of the duality. Finally, we present some practical aspects of the duality on which its usefulness is based.

3.1 Pre-requisites

3.1.1 Supersymmetric gauge theories

Supersymmetry is a particular kind of space-time symmetry that relates fermions to bosons, that is matter particles to force carriers. It was mathematically postulated after noticing that the mathematical group-theoretic description of the Poincaré symmetry might be consistently extended to include objects having fermionic properties, namely obeying anticommutation rules. Physically, this implies the mixing of bosons and fermions by a symmetry, so that each matter particle is predicted to have a force carrier partner particle, a so-called "superpartner", and *vice versa*, always in fermion-boson pairs.
Supersymmetry is a very elegant symmetry in mathematical terms which has furthermore the potential to solve some of the most significant problems of the standard model, like the naturalness issue [48]. Additionally, it provides the best candidates for dark matter particles and simplifies the study of strongly coupled quantum field theories [48]. Yet supersymmetry is facing a major obstacle in its way to broad acceptance by the scientific community: lack of experimental evidence. No supersymmetric particles have yet been discovered. Nevertheless this does not prevent theoreticians from assuming its validity and exploiting its many analytical advantages. In an optimistic scenario, this just represents a leap of faith ahead of experimental evidence to come. In the worst of cases though, it might just be a convenient detour to access features of real world physical systems that would otherwise remain beyond our technical reach.

Supersymmetry assumes the existence of fermionic generators that extend the Poincaré algebra to a graded algebra including both commutation and anti-commutation relations. This has been proved to be the only consistent way of embedding the Poincaré algebra in a bigger symmetry algebra. So apart from the common bosonic generators of translations P^μ and Lorentz transformations $M^{\mu\nu}$, the supersymmetry algebra entails generators transforming in the spinor representations of the Lorentz group $SO(1,3)$ also called supercharges. In order to visualise better the role played by the different spinor representations, it is useful to recall that the Lorentz algebra is double-covered by the complexified algebra $SL(2,\mathbb{C})$, the group of 2×2 matrices with unit determinant

$$SO(1,3) = SU(2)\times SU(2)^* = SL(2,\mathbb{C})/\mathbb{Z}_2, \tag{3.1.1}$$

which means that the representations of the Lorentz group may be labelled by two $SU(2)$ spins. This is the notation conventionally used in supersymmetry. Thereafter, spinors are denoted as 2-vectors transforming under one of the two non-equivalent fundamental spinor representations. The supercharges being spinors, they are represented by

$$Q^a_\alpha, \quad \bar{Q}^{\dot\alpha}_a \qquad \text{with } \alpha = 1,2 \quad \text{and} \quad a = 1,\dots,\mathcal{N}. \tag{3.1.2}$$

The indices α and $\dot\alpha$ signal the spinor components in the left and right spinor representations and $\mathcal{N}$ is the number of independent supersymmetries of the algebra. When talking about Weyl spinors in this context, it is understood that

$$(\psi_\alpha)^* = \bar\psi_{\dot\alpha}. \tag{3.1.3}$$

The requirement that CPT symmetry be preserved together with renormalisability restricts the possible number of supercharges to $\mathcal{N}\leq 4$[1] and the possible spectra of particles to those symmetric under a sign change in helicity. Thus the largest supersymmetric realisation of renormalisable field theories is $\mathcal{N}=4$, which is our case of interest.

$\mathcal{N}=4$ super Yang-Mills

Since we will further down be interested in the low-energy limit of the theory, we restrict ourselves to the massless supersymmetric multiplet. In this case, a number of relevant facts follow from the relations

$$\{Q^a_\alpha, \bar{Q}^{\dot\beta}_b\} = 2\sigma^\mu_{\alpha\dot\beta}P_\mu\delta^a_b \qquad \{Q_\alpha, Q_\beta = 0\} \qquad \{\bar{Q}_{\dot\alpha}, \bar{Q}_{\dot\beta}\} = 0. \tag{3.1.4}$$

Considering $P^\mu = (E,0,0,E)$

$$\{Q^a_\alpha, \bar{Q}^{\dot\beta}_b\} = 2\delta^a_b \begin{pmatrix} 4E & 0 \\ 0 & 0 \end{pmatrix}, \tag{3.1.5}$$

[1]Recall that gravity is not renormalisable so that this is not in conflict with the existence of the $\mathcal{N}=8$ multiplet.

hence the vanishing of the central charges implies that the second component of the supercharges must be zero

$$Q_2 = 0. \tag{3.1.6}$$

Furthermore, Q_1^a and $\bar{Q}_a^{\dot{1}}$ respectively lower and increase helicity by 1/2.

$$Q_1^a|E,\lambda\rangle = |E,\lambda - 1/2\rangle, \qquad \bar{Q}_a^{\dot{1}}|E,\lambda\rangle = |E,\lambda + 1/2\rangle, \tag{3.1.7}$$

where E stands for the energy and λ for the helicity that characterise a state. Note that by virtue of the spin-statistics theorem, this fact means that the supersymmetry generators relate bosons to fermions and *vice-versa*.
So the field content of the $\mathcal{N} = 4$ supermultiplet will be the generated by the different choices among the 4 supercharges when generating superpartner states from the lowest or highest helicity state and then adding the corresponding CPT conjugates, that is the states with the flipped helicities. In the case $\mathcal{N} = 4$, it is then clear that departing from a lowest helicity state with $\lambda = -1$, we have $\binom{4}{1}$ possibilities to get to a state with $\lambda = -1/2$ and $\binom{4}{2}$ to obtain a scalar. This means that the theory contains 1 vector field, 4 fermions and 6 scalars and the corresponding CPT-conjugates, for a total of 16 different states. This is referred to as the gauge multiplet

$$\mathcal{N} = 4 \text{ gauge multiplet:} \quad (A_\mu, \psi_\alpha^a, X^i) \quad a = 1,\dots,4 \quad i = 1,\dots,6. \tag{3.1.8}$$

Taking into account the different choice possibilities of the supercharges to generate the states, it is possible to realise that these transform under an $SU(4)_R = SO(6)_R$ symmetry that rotates the supercharges globally into one another, the so-called R-symmetry, hence the R label. Under this symmetry, A_μ is a singlet, the fermions ψ transform in the fundamental 4-dimensional representation ans the scalars X transform in the adjoint 6-dimensional representation.
With respect to the gauge theory group, all fields are obliged by supersymmetry to transform in the same representation, namely in the adjoint.

Apart from having the maximal possible amount of supersymmetry in four space-time dimensions, $\mathcal{N} = 4$ Super Yang-Mills also has the very relevant characteristic of being a conformal theory, that is a theory with no physical scale. This conformal symmetry does not only hold at the classical level but also at the quantum level, as can be seen from the vanishing β-function (see for example [49]). The presence of the conformal symmetry is manifest in the form of the Lagrangian of the theory, which might be obtained by dimensional reduction from the 10-dimensional $\mathcal{N} = 1$ gauge theory [50] and has been known for a long time now [51]

$$\begin{aligned}\mathcal{L} = \mathrm{Tr}\ \Big(&\frac{1}{4}F^2 + \frac{1}{2}D_\mu X_i D^\mu X^i - \frac{g_{YM}^2}{4}[X_i, X_j][X^i, X^j] + \bar{\psi}_a \sigma^\mu D_\mu \psi_a \\ &- \frac{ig_{YM}}{2}\sigma_i^{ab}\psi_a[X^i,\psi_b] - \frac{ig_{YM}}{2}\sigma_{ab}^i\bar{\psi}^a[X_i,\bar{\psi}^b]\Big),\end{aligned} \tag{3.1.9}$$

where σ^μ and σ^i are respectively the chiral projections of the gamma matrices in four and six dimensions.All terms in this Lagrangian have dimension 4, from which scale invariance follows. The scale invariance extends Poincaré invariance to conformal symmetry in four dimensions, with symmetry group $SO(2,4) \simeq SU(2,2)$. This symmetry group must be added to the already mentioned R-symmetry group $SU(4) \simeq SO(6)$, so that the bosonic symmetry group of $\mathcal{N} = 4$ Super Yang-Mills is

$$\text{Bosonic symmetry of } \mathcal{N} = 4 \text{ SYM} \qquad SO(2,4) \times SO(6).$$

Together with the supersymmetry generators, the entire symmetry group of the theory is extended to the graded Lie group $SU(2,2|4)$, known as the $\mathcal{N} = 4$ superconformal group in four dimensions [50].

Summing up, $\mathcal{N} = 4$ super Yang-Mills is the gauge theory with the maximal possible amount of supersymmetry in four space-time dimensions. It furthermore displays superconformal symmetry with symmetry group $SU(2,2|4)$, whose bosonic subgroup is $SO(2,4) \times SO(6)$. The field content consists of a gauge field A_μ, four chiral fermions ψ_α, six real scalars X^i and the corresponding CPT conjugates.

3.1.2 Supergravity and string theory

We now want to turn to supergravity, the low-energy limit to the most eminent candidate to a complete theory that includes gravity and supersymmetry, namely superstring theory. Supergravity arises from string theory when we consider the limit in which strings are massless, i.e. point-like, and interact only at tree-level. Purely symmetric considerations suffice to derive a lot of information about the theory.
Firstly, although no formal proof has been provided, there is strong believe in physics that no particles with spin higher than 2 can exist in more than four space-time dimensions. Their existence would break causality, imply the existence of more than one gravity particle or graviton and present the impossibility of coupling to any known conserved currents [47, 48]. This restricts in general the content of supermultiplets in any physical theory, excluding particles with spin > 2.
In higher dimensions the massless supersymmetry algebras are given by

$$\{Q^a_\alpha, \bar{Q}^{\dot{\beta}}_b\} = 2\delta^a_b \begin{pmatrix} 4E & 0 \\ 0 & 0 \end{pmatrix} \qquad \{Q_\alpha, Q_\beta = 0\} \qquad \{\bar{Q}_{\dot{\alpha}}, \bar{Q}_{\dot{\beta}}\} = 0, \qquad (3.1.10)$$

which as in the four-dimensional case implies the effective vanishing of half of the supercharges. The supercharges transform in space-time under the spinor representation, which in d-dimensional space-times has dimensions $2^{d/2}$ for even d and $2^{(d-1)/2}$ for odd d. The requirement that no particle with spin > 2

is present in the theory then implies that the number of raising/lowering operators is restricted to be at most 8. Thus in the massless case, when only one fourth of the supercharges are left to act as raising/lowering operators, these considerations result in a restriction in the number of space-time dimensions, $d \leq 11$.

Taking all of the above into account, the field content of supergravity in $d = 11$ is uniquely specified. Fields are classified according to their representation under the little group, namely according to their propagating degrees of freedom. In a d-dimensional space-time, the little group for massless particles is $SO(d-2)$. Hence the maximal supergravity multiplet in $d = 11$ is obtained by considering different irreducible representations of the little group $SO(9)$. Considering the necessity of presence of the graviton, $g_{\mu\nu}$, to account for gravity, which always transforms in the second symmetric traceless representation of the space-time symmetry group, and the imposition by supersymmetry that there be a superpartner gravitino, $\psi_{\mu\alpha}$, and that the number of bosonic degrees of freedom be equal to the number of fermionic degrees of freedom, which requires the presence of a bosonic 3-form, $C^{(3)}_{\mu_1\mu_2\mu_3}$, the only possible multiplet consists of the three mentioned fields, with 44, 128 and 84 propagating degrees of freedom each

11D SUGRA		
$g_{\mu\nu}$ (44)	$C^{(3)}_{\mu_1\mu_2\mu_3}$ (84)	$\psi_{\mu\alpha}$ (128)
graviton	3-form	gravitino

They constitute the so-called massless gravity supermultiplet in 11-dimensional space-time. The language of group theory based on the use of Dynkin labels is quite useful for these considerations. A review of the necessary ideas is presented in appendix A. In these terms, the field content of 11-dimensional supergravity can be obtained from the basic irreducible representations of $SO(9)$,

$SO(9)$ has 4 basic irreps	
irrep	dofs
$[1,0,0,0]_9$	9
$[0,1,0,0]_9$	36
$[0,0,1,0]_9$	84
$[0,0,0,1]_9$	16 ,

by combining them properly as tensor products as follows:

11d SUGRA	irreps	obtained from
$g_{\mu\nu}$	$[2,0,0,0]_9$	$Sym^2([1,0,0,0]_9)$
$C^{(3)}_{\mu_1\mu_2\mu_3}$	$[0,0,1,0]_9$	$\Lambda^3([1,0,0,0]_9)$
$\psi_{\mu\alpha}$	$[1,0,0,1]_9$	$([1,0,0,0]_9 \otimes [0,0,0,1]_9)$.

With this in mind, it is possible to obtain the dimensional reduction of 11-dimensional supergravity to 10 space-time dimensions by assuming that the dependence of the fields on the 11th coordinate may be ignored. The dimensional reduction of the representations of $SO(9)$ to those of $SO(8)$ is easy to track by means of the Dynkin labels, which help keeping an overview of the representations and the degrees of freedom involved. The bosonic sector reduces as follows. The metric is dimensionally reduced to a lower-dimensional metric, a vector field or 1-form and a scalar:

$$\begin{array}{ccccccccc} [2,0,0,0]_9 & \longrightarrow & [2,0,0,0]_8 & \oplus & [1,0,0,0]_8 & \oplus & [0,0,0,0]_8 \\ g_{\mu\nu} & \longrightarrow & g_{ij} & + & g_{i10} & + & g_{1010} \\ 44 & \longrightarrow & 35 & + & 8 & + & 1\,. \end{array}$$

The 3-form reduces to another 3-form and a 2-form,

$$\begin{array}{ccccccc} [0,0,1,0]_9 & \longrightarrow & [0,0,1,1]_8 & \oplus & [0,1,0,0]_8 \\ C^{(3)}_{\mu_1\mu_2\mu_3} & \longrightarrow & C^{(3)}_{ijk} & + & B^{(2)}_{ij10} \\ 84 & \longrightarrow & 56 & + & 28\,. \end{array}$$

The dimensional reduction of the gravitino is slightly more complicated. Its derivation via tensor products can be seen in appendix A. It is given by

$$\begin{array}{ccccccccccc} [0,0,1,1]_9 & \longrightarrow & [1,0,1,0]_8 & \oplus & [0,0,0,1]_8 & \oplus & [1,0,0,1]_8 & \oplus & [0,0,1,0]_8 \\ \psi_{\mu\alpha} & \longrightarrow & \psi_{\mu\alpha} & + & \psi_{\dot\alpha} & + & \psi_{\mu\dot\alpha} & + & \psi_\alpha \\ 128 & \longrightarrow & 56 & + & 8 & + & 56 & + & 8\,. \end{array}$$

The dimensional reduction of 11d supergravity to 10 dimensions results in the so-called Type IIA supergravity with field content

Type IIA SUGRA				
BOSONIC SECTOR				
$[2,0,0,0]_8$	$[0,1,0,0]_8$	$[0,0,0,0]_8$	$[0,0,1,1]_8$	$[1,0,0,0]_8$
$g_{\mu\nu}$ (35)	$B^{(2)}_{\mu\nu}$ (28)	ϕ (1)	$C^{(3)}_{\mu\nu\sigma}$ (56)	$A^{(1)}_\mu$ (8)
graviton	2-form	dilaton	3-form	1-form
FERMIONIC SECTOR				
$[0,0,1,0]_8$	$[0,0,0,1]_8$	$[1,0,1,0]_8$	$[1,0,0,1]_8$	
ψ_α (8)	$\psi_{\dot\alpha}$ (8)	$\psi_{\mu\alpha}$ (56)	$\psi_{\mu\dot\alpha}$ (56)	
L gravifermion	R gravifermion	L gravitino	R gravitino	

It is iseful to note that the Type IIA supergravity multiplet admits a factorized form (see appendix A for some useful tensor factorisations)

$$\text{Type IIA 10d SUGRA:} \quad ([1,0,0,0]_8 \oplus [0,0,1,0]_8) \otimes ([1,0,0,0]_8 \oplus [0,0,0,1]_8) \tag{3.1.11}$$

This suggests that a new supermultiplet may be constructed by performing a change in the fermionic sector, taking both fermions to be of the same chirality. The resulting supermultiplet is

$$\text{Type IIB 10d SUGRA:} \quad ([1,0,0,0]_8 \oplus [0,0,0,1]_8)^2 = [2,0,0,0]_8 \oplus [0,1,0,0]_8 \oplus [0,0,0,0]_8 \oplus 2[1,0,0,1]_8 \oplus 2[0,0,1,0]_8 \oplus [0,0,0,2]_8 \oplus [0,1,0,0]_8 \oplus [0,0,0,0]_8 \tag{3.1.12}$$

which is known as Type IIB supergravity. It shares the bosonic sector with Type IIA supergravity but presents only fermions with the same chirality. The detailed field content is

Type IIB SUGRA			
BOSONIC SECTOR			
$[2,0,0,0]_8$	$2 \times [0,1,0,0]_8$	$2 \times [0,0,0,0]_8$	$[0,0,0,2]_8$
$g_{\mu\nu}$ (35)	$A^{(2)}_{\mu\nu}, B^{(2)}_{\mu\nu}$ (2×28)	ϕ, C (2×1)	$C^{(4)+}_{\mu}$ (35)
graviton	2-forms	dilaton, axion	4-form (self-dual)
FERMIONIC SECTOR			
	$2 \times [0,0,1,0]_8$	$2 \times [1,0,0,1]_8$	
	$2 \times \psi_{\alpha}$ (2×8)	$2 \times \psi_{\mu\dot{\alpha}}$ (2×56)	
	2 gravifermions	2 gravitini	

The two gravifermions have the same chirality, which is opposite to that of the two gravitini. A remarkable fact about Type IIB theory is that the 4-form has a self-dual field strength. This has made it this far impossible to write an action for Type IIB supergravity. The self-duality must be imposed as a separated field equation. More will be said about this further down. So we have derived the maximal supergravity in 11 space-time dimensions mostly from symmetry arguments and then arrived at the field content of Type IIA and Type IIB supergravity theory, at whose bosonic field content we are going to give now a closer look.

3.1.3 p-branes

All the supergravity theories presented above contain antisymmetric form fields, which allow for the definition of their corresponding field-strengths. Such field strengths can then be included in an action from which the equations of motion may be obtained. Given an n-form $C^{(n)}$, we may define a field-strength $n+1$-form, $G^{(n+1)}$, by means of the exterior derivative

$$G = d\,C. \tag{3.1.13}$$

Using G, Maxwell-like equations may be written in any number of dimensions d with the corresponding sources

$$d * G = \delta^{(d-n)} Q_E, \qquad d\,G = \delta^{(n+2)} Q_M, \tag{3.1.14}$$

which are characterised by charges Q_E and Q_M by analogy with the magnetic and electric charges of the classical four-dimensional Maxwell case. The sources are then localised in $d-n$ and $n+2$ dimensions respectively, i.e. extended in n and $d-n-2$ dimensions and are named p-branes, with $p=n-1$ and $p=d-n-3$ respectively. This is somewhat a generalisation of the common procedure in Maxwell electromagnetism.
The charges associated to the forms present in the theories described above resulting in the tensor factorisations (3.1.11) and (3.1.12) from a fermion-fermion product are furthermore named Dp-branes and will be object of special attention for us. What kind of p-branes are present in the theory depends on the differential forms contained in it. In the case of the 11-dimensional maximal supergravity, there is only one 3-form present in the theory, which gives rise to

$$\begin{aligned} d * G^{(4)} &= \delta^{(8)} Q_E \rightarrow \text{M2-brane}, \\ d\, G^{(4)} &= \delta^{(5)} Q_M \rightarrow \text{M5-brane}. \end{aligned} \tag{3.1.15}$$

We say that an M2-brane is electrically charged under the $C^{(3)}$ whereas an M5-brane is magnetically charged. We also say that an M5-brane is the magnetic dual of an M2-brane. Following the same procedure it is possible to find the brane solutions present in Type IIA supergravity and Type IIB supergravity:

Type IIA:	F1	NS5	D0	D2	D4	D6	D8
Type IIB:	F1	NS5	D(-1)	D1	D3	D5	D7

The fundamental string, F1, and its magnetic dual, the NS5, which are common to both theories, receive special names because they arise from the so-called NSNS-sector, namely the boson-boson product in the tensor factorisations (3.1.11) and (3.1.12).
A p-brane is hence a $(p+1)$-dimensional object, located at a point in a $(9-p)$-dimensional space. That means that its existence spontaneously breaks Poincaré invariance in $9-p$ dimensions, giving rise to $9-p$ massless Goldstone boson scalars living on the brane. The $9-p$ scalar fields describe the fluctuations of the brane in the transverse directions. Furthermore, a Dp-brane is defined to be an object on which a fundamental string may end, restricting the motion of the string in the $9-p$ dimensions transverse to it. Hence the name Dp-brane, the D standing for Dirichlet. An observer living on the Dp-brane does not see the string, just sees its end as a charged point particle propagating in $p+1$ dimensions. This allows the world-volume observer to make use of Gauss's law and associate an abelian gauge field to the end of the string on the brane. This abelian gauge field might as well be understood as Goldstone modes associated to large gauge transformations spontaneously broken by the brane [52, 53, 54]. It is the lowest excitation of an open string with both ends on the brane. The presence of the brane furthermore breaks supersymmetry spontaneously preserving just 16 of the 32 supersymmetries. The corresponding massless Goldstone modes are fermionic and complete the

supermultiplet of Goldstone modes generated by the presence of the brane in space-time. Hence the spectrum of degrees of freedom on the brane consists of an abelian gauge field, A_μ, $\mu = 0, \ldots, 9-p$, $9-p$ scalar fields ϕ_i, $i = 1, \ldots, 9-p$ and the corresponding fermionic superpartners.

A very interesting property of D-branes is their capacity of giving raise to non-abelian gauge theories when several branes come close to each other [55]. Consider for example the case in which 2 D-branes stay close to one another. In addition to the degrees of freedom corresponding to each of the branes, strings may now also stretch between different branes. As shown in figure 3.1 there are now four different types of strings, depending on where the starting and ending points lie. The strings starting and ending on the same brane are just two massless vector fields like the one we had in the single-brane case. Additionally there are now two massive vector fields for the two possibilities of a string starting on one brane and ending on the other one. Thus the configuration has furthermore a scale given by the distance between the branes, which determines the minimal mass of the strings stretching between them. When the branes overlap, this scale is lost. In this limit all strings must be massless and hence it corresponds to a low energy limit. The two massive vector fields mentioned loose now their masses and there are four massless vector propagating degrees of freedom, which corresponds to a gauge field transforming under the adjoint representation of a $U(2)$ gauge group. Since supersymmetry commutes with gauge rotations, the entire supermultiplet must transform under the same representation of the group, so that the $9-p$ scalars and the fermionic superpartners (gauginos) will also be in the adjoint representation of the $U(2)$. In a sense, if we start with the two branes lying on top of each other, the process of separation may be seen as a kind of Higgs mechanism whereby the $U(2)$ is spontaneously broken to a $U(1)^2$ with 2 massive gauge bosons.

It is now interesting to consider the case of a number, say N, of neighbouring D-branes. By analogy with the 2-brane case, there are now have N massless gauge bosons and $N(N-1)$ massive gauge bosons besides the corresponding scalar and fermionic fields. The situation is illustrated in figure 3.2. When the N branes lie on top of each other there are N^2 massless gauge bosons, which corresponds to a gauge group $U(N)$. An $U(N)$ group contains a $U(1)$ factor

$$U(N) = SU(N) \times U(1), \tag{3.1.16}$$

which is interpreted as a global excitation of the centre of mass of the branes and might therefore be factored out. Thereby the gauge group relevant for the dynamics of the branes with respect to one another is $SU(N)$.
All in all, this means that a system of N Dp-branes might be used to study the physics of $SU(N)$ supersymmetric gauge theories in $p+1$ dimensions with 16 supercharges.

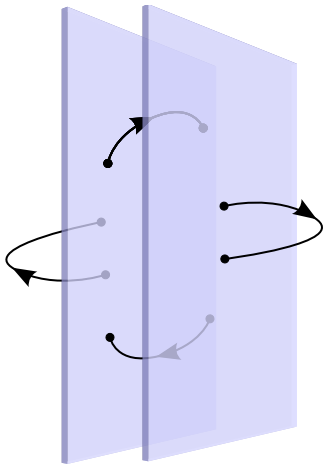

Figure 3.1: Different stretching possibilities of the strings between two neighbouring D-branes. The different orientations of the strings are counted as independent degrees of freedom since they stand for charges with different sign.

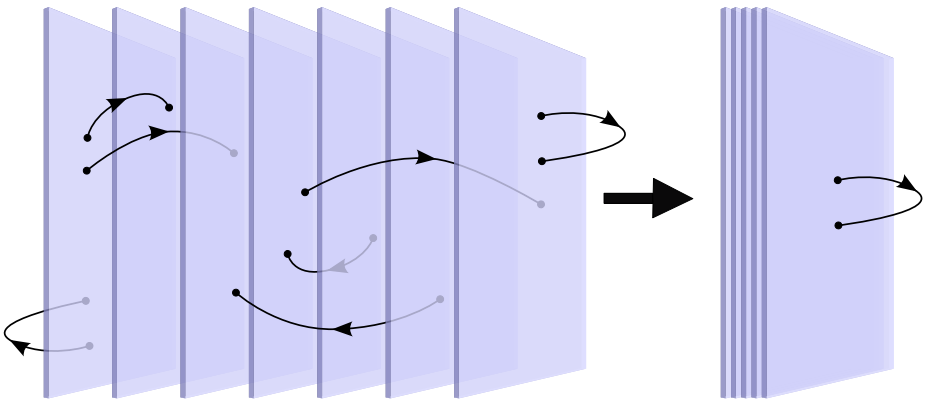

Figure 3.2: Different stretching possibilities of the strings between N neighbouring D-branes are shown on the left. The different orientations of the strings are counted as independent degrees of freedom since they stand for charges with different sign. The right picitures illustrates the situation in which the branes are coincident.

3.2 A stack of D3-branes: different perspectives

Af all the possible D-branes presented in the previous section, the case of D3-branes present in Type IIB supergravity is of special interest for a number of reasons. Firstly, their world-volume is a 4-dimensional Poincaré invariant space-time, which is much appreciated when trying to get closer to real-world physics. Furthermore it happens to be self-dual, for a D3-brane sources a 4-form, which is self-dual in a 10-dimensional space-time

$$d\,G^{(5)} = \delta^{(6)}Q = d * G^{(5)}. \tag{3.2.1}$$

That is, a D3-brane carries both electric and magnetic charge. This self-duality condition is imposed separately when writing the equations of motion in the form

$$*G^{(5)} = G^{(5)}, \tag{3.2.2}$$

for no action is known which is otherwise complete.

3.2.1 Gauge theory from the branes: open string perspective

In the light of the above considerations, a stack of D3-branes lying on top of each other will support a supermultiplet living on their world-volume consisting of a gauge field, six scalar fields and four Weyl fermions, all of them transforming in the adjoint representation of an $SU(N)$ gauge group. This is exactly the field content of $\mathcal{N}$=4 super Yang-Mills theory (3.1.8) with an $SU(N)$ gauge group. Indeed at the two-derivative level[2], the low-energy effective action for the massless supermultiplet living on the world-volume of the D3-branes is precisely the action of $\mathcal{N}$=4 super Yang-Mills in (3+1) space-time dimensions with a gauge group $SU(N)$ [56]. The Yang-Mills coupling constant is then given by

$$g^2_{YM} = 4\pi g_s, \tag{3.2.3}$$

g_s being the string coupling.
Hence in the low energy limit, N coincident D3-branes reproduce the dynamics of $\mathcal{N}$=4 super Yang-Mills theory in 4 dimensions with an $SU(N)$ gauge group.

3.2.2 Gravity theory from the branes: closed string perspective

Branes are not only sources to the differential forms but also sources of curvature to space-time as dictated by Einstein's general relativity, given that

[2]The Lagrangian receives higher-derivative corrections suppressed by $\alpha' E^2$ with α being the inverse string tension and E the energy. Such corrections can therefore be neglected in the low-energy limit.

they gravitate as any other material object. Their presence deforms the space-time around them according to their energy and matter content. From this perspective, branes are not the solitonic objects on which open strings may end, but rather the massive objects that determine the geometry of the background space-time in which closed strings propagate. The space-time metric sourced by a stack of N coincident D3-branes can be calculated by solving the corresponding equations of motion of supergravity [57, 58]

$$ds^2 = \left(1 + \frac{L^4}{r^4}\right)^{-\frac{1}{2}} \eta_{ij} dx^i dx^j + \left(1 + \frac{L^4}{r^4}\right)^{\frac{1}{2}} \left(dy^2 + y^2 d\Omega_5^2\right) \tag{3.2.4}$$

with η_{ij} being the common flat Minkowski metric in the directions parallel to the D3-branes and the metric in the second parentheses being the flat metric in the directions transverse to the branes in spherical coordinates. L is the radius of the D3-branes, which is given by

$$L^4 = 4\pi g_s N (\alpha')^2. \tag{3.2.5}$$

Note that the metric (3.2.4) only depends on r. For $r \gg L$ the metric reduces to that of flat space. Thus L may be seen as the length scale characteristic of the range of the gravitational effects of the D3-branes. In the opposite limit, for $r \ll L$ the metric (3.2.4) reduces to the so-called *throat region* in its near-horizon limit

$$ds^2 = \frac{r^2}{L^2} \eta_{ij} dx^i dx^j + \frac{L^2}{r^2} dr^2 + L^2 d\Omega_5^2. \tag{3.2.6}$$

By means of the coordinate redefinition

$$u \equiv L^2/r, \tag{3.2.7}$$

it becomes manifest that the metric (3.2.6) is

$$ds^2 = ds^2_{AdS_5} + L^2 d\Omega_5^2, \tag{3.2.8}$$

with

$$ds^2_{AdS_5} = \frac{L^2}{u^2} \left(\eta_{ij} dx^i dx^j + du^2\right), \tag{3.2.9}$$

where the label AdS_5 stems from the identification of this metric with the known one for five-dimensional Anti de Sitter space-time. Hence from a closed string perspective there are two different sets of degrees of freedom, those propagating in the flat Minkowski region and those propagating in the near-horizon region, which are described by fluctuations about the $AdS_5 \times S^5$ solution of Type IIB supergravity. The interaction terms between both sets of modes are proportional to GE^8 [59], so they decouple from each other in the limit of low energy. Furthermore, if this limit is approached in a particular way, namely in the so called Maldacena limit

$$\alpha' \to 0 \qquad u = \frac{r}{\alpha'} \text{ fixed}, \tag{3.2.10}$$

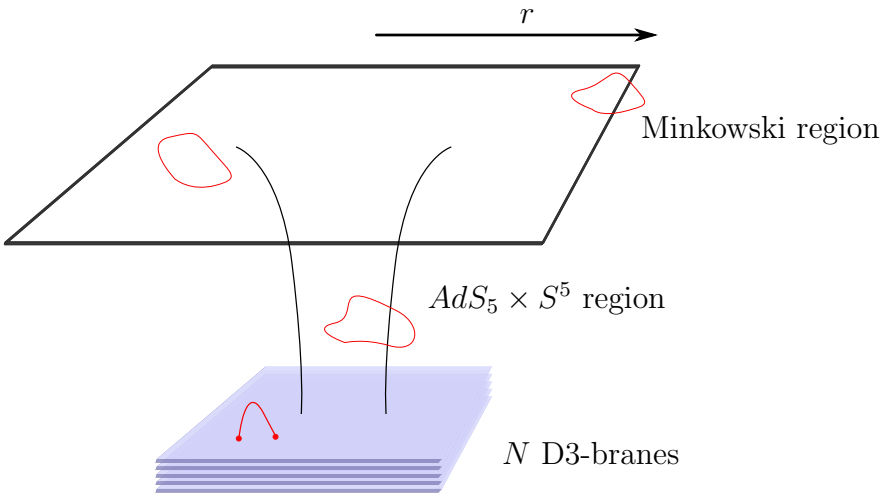

Figure 3.3: Illustration of the geometric limits. For $r \gg L$ the metric felt by the closed strings is that of flat space whereas near the branes, $r \ll L$, it tends to $AdS_5 \times S^5$. In the open string picture, the branes support an $\mathcal{N}$=4 super Yang-Mills theory with gauge group $SU(N)$. Since both theories are two different parameter regimes of the same object, Maldacena proposed the equivalence of the descriptions and launched the AdS/CFT correspondence.

the near-horizon region effectively becomes dominant [45], so that we can conclude that in the closed string description, the low energy sector reduces to closed strings propagating in $AdS_5 \times S^5$. An illustration of the geometry of the branes is shown in figure 3.3.

3.2.3 The AdS/CFT correspondence

We have seen that when describing a stack of N D3-branes in the low energy limit, closed and open strings offer alternative descriptions. The near-horizon geometry sourced by the branes reduces in this limit to string theory in an $AdS_5 \times S^5$ geometry. The gauge theory on the world-volume of the branes is equivalent to $\mathcal{N}$=4 super Yang-Mills theory with a gauge group $SU(N)$. It is furthermore important to notice that since the N coincident D3-branes represent N units of charge under the 5-form, their flux must be consistent with this and hence equal to the number of colours of the dual gauge theory. In a Gauss-law-like formulation

$$\int_{S^5} G^{(5)} = N. \tag{3.2.11}$$

Thus the rank of the $SU(N)$ gauge group coincides with the 5-form flux of the branes through a surrounding 5-sphere.

Summarizing, in the low energy limit there are two possible descriptions for a stack of N coincident D3-branes:

- Type IIB superstring theory on $AdS_5 \times S^5$with AdS and S^5 having the same radius L, the string coupling being g_s and the self-dual 5-form $G^{(5)}$ having integer flux N;

- $\mathcal{N}$=4 super Yang-Mills theory in 4-dimensions with gauge group $SU(N)$ and Yang-Mills coupling g_{YM};

with

$$g_{YM}^2 = 4\pi g_s, \qquad L^4 = 4\pi g_s N(\alpha')^2. \tag{3.2.12}$$

The fact that descriptions are equivalent in the low energy limit led Juan Martin Maldacena to conjecture that they are actually equivalent things even beyond this limit, giving birth to the AdS/CFT correspondence in its strongest formulation. Equivalence is understood here as a map between fields of the string theory and operators of the gauge theory, which transform under the same representations of the corresponding symmetries and as the equivalence of the respective dynamics. Yet the statement of the equality of both descriptions in its broadest sense remains a conjecture inasmuch as no proof of it has been provided. Given that it involves the full quantum type IIB supersting theory it is difficult to access and to test. Nevertheless, there are more restrictive versions of the duality which, while being less general are easier to handle with.

The t'Hooft limit

The t'Hooft limit [60] consists in taking the number of coulours N to be very large while keeping the so called t'Hooft coupling $\lambda \equiv g_{YM}^2 N = g_s N$ fixed,

$$N \to \infty, \text{ with } \quad \lambda \equiv g_{YM}^2 N = g_s N \text{ fixed.} \tag{3.2.13}$$

In this limit, all non-planar Feynman diagrams in the perturbative expansion of the gauge theory are suppressed [46], whereas in the string theory, since $g_s = \frac{\lambda}{N}$, the theory becomes weakly coupled string perturbation theory. Hence in this limit the AdS/CFT duality reduces to a correspondence between the classical tree-level string theory and the large N limit of the gauge theory, in which non-planar diagrams are suppressed.

The Maldacena limit

Additionally, the limit

$$\lambda \gg 1 \tag{3.2.14}$$

can be taken together with $N \to \infty$. The combination of both limits is known as the Maldacena limit. λ can be interpreted as the dimensionless effective coupling of the super Yang-Mills gauge theory, hence in this limit the gauge theory evolves to a strongly coupled one. In the gravity side of the duality,

one sees through the relation resulting from combining equations (3.2.5) and (3.2.13) that

$$L^4 = \lambda(\alpha')^2 \tag{3.2.15}$$

which means the the limit of big λ is tantamount to taking $\alpha' \to 0$ and hence recovering the supergravity regime of massless modes from which we got the inspiration of the duality. Thus in this limit the AdS/CFT duality is reflected as a correspondence between classical supergravity and the large N and strong coupling limit of the gauge theory.

Summing up, depending on the parameter regime, one or the other of the two possible perspectives of the stack of D3-branes becomes tractable. In particular when $g_sN \ll 1$ the closed string description is not useful, whereas when $g_sN \gg 1$ it simplifies to classical supergravity, which is basically Einstein gravity coupled to various matter fields. The open string description is tractable when $g_sN \ll 1$ and expansions in series of Feynman diagrams are possible whereas it becomes effectively strongly coupled and hence difficult to handle at $g_sN \gg 1$. Nevertheless both descriptions exist in both limiting regimes and also in between, the crucial question is when they become technically tractable. This thesis is based on the most restrictive version of the duality, that is in the Maldacena limit, $N \to \infty$, λ. We have seen that, as stated in [59], the strong coupling limit in the gauge theory suppresses the stringy nature of the dual string theory taking it to the supergravity regime, whereas the large N limit suppresses the quantum nature of the string theory, restricting it to the tree-level. When both limits are taken together, the full string theory reduces to a tractable classical theory of supergravity. In that regime we are able to perform computations that are dual to, and hence offer an interpretation within, a planar strongly coupled $\mathcal{N}$=4 super Yang-Mills theory with gauge group $SU(N \to \infty)$.
Since both theories are seen as different descriptions of the same physics, it is conjectured that they are dynamically equivalent in the sense that all the physics present in one of the descriptions, including fields and their interactions, must be mapped onto the physics in the other description.

3.2.4 Holography

The tractable version of string theory that enters the correspondence is compactified on an $AdS_5 \times S^5$space-time. Since the S^5 part of the metric is compact, any 10-dimensional field may be expressed as a tower of states by expanding it in terms of harmonics on the S^5. So if for example, x and ω denote the coordinates in AdS_5 and S^5 respectively, a scalar field $X(x, \omega)$ in $AdS_5 \times S^5$may be written as

$$X(x, \omega) = \sum_k X_k(x) Y_k(\omega), \tag{3.2.16}$$

where $Y_k(\omega)$ are the spherical harmonics on the S^5. This allows to practically see the duality as a correspondence between the four-dimensional $\mathcal{N}$=4 super Yang-Mills theory and a gravity theory on AdS_5, thereby providing a realisation of the holographic principle [61, 18], which states that a theory of quantum gravity in a given space ought to be described by a theory without gravity living on the boundary of that space. In fact the gauge theory might be seen as living on the boundary of AdS space and the extra radial direction is interpreted as an RG flow, namely as an energy scale above which fields have been integrated out in the wilsonian sense [19]. Indeed if a scale transformation $x^\mu \to Cx^\mu$ is carried out in the gauge theory and the energy E is rescaled by $E \to E/C$ the transformation is a symmetry of the system. In the metric (3.2.9) such a scale transformation is accompanied by $u \to u/C$, which leads to the identification

$$E \sim 1/u \sim r. \tag{3.2.17}$$

So the radial coordinate of AdS is identified with the energy scale in the dual field theory. Now as pointed out in [62], if the gauge theory with no degrees of freedom integrated out is seen as the most fundamental, it is natural for it to be situated at $r = \infty$ ($u = 0$), namely at the boundary of AdS. This is the basis of the holographic nature of the AdS/CFT correspondence. The dual gauge field theory sits at the boundary of the AdS part of the space-time geometry. It also makes sense to notice that since all energies scales are present in a conformal field theory, it is no surprise that the geometry extend all the way from $r = 0$ to $r \to \infty$.
This is also the reason why in the AdS/CFT jargon, the near boundary region is referred to as UV, whereas close to the lowest value of the radial coordinate (highest in terms of u) people talk about the infra-red.

3.2.5 Matching of symmetries

If the two alternative approaches to the stack of N D3-branes presented above are really to be equivalent, the physics in both sides must be the same, which necessarily requires the global symmetries in both sides of the duality to be the same.
In section 3.1.1 we saw that the global symmetries of $\mathcal{N}$=4 super Yang-Mills is given by the group $SU(2,2|4)$, whose maximal bosonic subgroup is $SO(2,4)\times SO(6)$, that is the product of the conformal group in four dimensions and the $SU(4) = SO(6)$ group of R-symmetries that rotate the supersymmetries into one another. This bosonic subgroup can immediately be identified on the string theory side of the duality as the group of isometries of $AdS_5 \times S^5$. Furthermore, since the presence of the branes breaks half of the number of supersymmetries, reducing them from the initial 32 to 16 and these are supplemented in the AdS limit by another 16 conformal supersymmetries, the total global symmetry is also seen to be $SU(2,2|4)$ on the string theory side and hence perfectly matches on both sides of the duality.

Given that gauge symmetries express a redundancy in the mathematical description of the physics, there is no need for them to be the same on both sides of the duality as is the case for global symmetries. Still they play an important role in AdS/CFT as they do in general in gauge/gravity duality. There is a correspondence between global symmetries in the gauge theory and gauge symmetries in the dual string theory. We will see more about this later.

Once we have seen that the global symmetries in both sides of the duality are the same, it is natural to expect that the objects transforming under the same representations of the symmetry group are physically related by means of the correspondence. This is indeed the case. It can be shown that the spectrum of operators on the gauge theory side of the duality can be mapped to fields in the massless Type IIB supergravity multiplet compactified on $AdS_5 \times S^5$ [47].

3.3 The dictionary: practicalities

Beyond the collection of intuitive evidences in favour of the duality we have so far gone over, a systematic and consistent approach to the duality was presented in [19] in which the foundations of the utilisation of the duality were laid. There it was shown that there is indeed a one-to-one correspondence between operators of the boundary gauge theory and gravity fields that transform in the same representation of the symmetry groups as the former. A precise prescription was given relating the boundary values of the bulk fields to the field operators of the dual gauge theory. The bulk path integral for the fields ϕ with boundary values ϕ_0

$$\mathcal{Z}_{string}(\phi) = \int_{\phi_0} D\phi\, e^{-S_{\text{string}}}, \tag{3.3.1}$$

is identified with the generating functional for correlation functions of an operator $\mathcal{O}$ in the dual field theory

$$\left\langle e^{\int dx^4\, \phi_0\, \mathcal{O}} \right\rangle_{\text{CFT}}, \tag{3.3.2}$$

by seeing the boundary value of the gravity theory field as a source for the gauge theory operator, which comes into the action via a term of the form

$$\int d^4x\, \phi_0(x)\, \mathcal{O}(x), \tag{3.3.3}$$

with

$$\phi_0(x) = \phi(u, x)|_{u=0}. \tag{3.3.4}$$

where the coordinate u is the same as in (3.2.9). Hence the prescription to make use of the duality given in [19] may be summarized as

$$\mathcal{Z}_{string}\left[\phi(x,u)|_{u=0} = \phi_0(x)\right] = \left\langle e^{\int dx^4\, \phi_0\, \mathcal{O}} \right\rangle_{\text{CFT}}. \tag{3.3.5}$$

Note though that no general explicit form of $\mathcal{Z}_{string}$ is known. Still, in the weak version of the correspondence presented above, in which both the quantumness and the stringiness of the strings are suppressed by the limits $N \to \infty$ and $\lambda \gg 1$, a saddle point approximation to the supergravity action is appropriate and the partition function may be approximated by

$$\mathcal{Z}_{string} \approx e^{-S_{\text{sugra}}}\big|_{on-shell}\,, \tag{3.3.6}$$

in which case, the on-shell bulk action of supergravity acts as the generating functional for the correlation functions of the operators in the gauge theory. Via this prescription, arbitrary n-point functions of the gauge theory may be computed, which in a conformal theory provide all physical information. This identification of the partition function of both dual theories is a beautiful realisation of the physical principle that the information contained in both theories be equivalent.

Even though no complete systematic recipe is known to find the field dual to a given operator, some of the entries of the dictionary are straightforward from (3.3.3) and the fact that both the field and the operator must have the same quantum numbers with respect to the global symmetries. In particular it is not difficult to find the dual fields to operators in the gauge theory which are conserved currents associated to global symmetries. So for example a gauge field in the gravity theory $A_\mu(u,x)$ with a boundary value $A_\mu(x)$

$$A_\mu(x) = A_\mu(u,x)|_{\partial AdS} = \lim_{u\to 0} A_\mu(u,x) \tag{3.3.7}$$

is naturally coupled to a conserved current $J^\mu(x)$ as

$$\int d^4x\, A_\mu(x) J^\mu(x). \tag{3.3.8}$$

This identification realises the fact mentioned above that continuous global symmetries in the boundary field theory correspond to gauge transformations in the gravity theory.
Analogously, the conserved charge associated to translational invariance, the energy momentum tensor $T^{\mu\nu}(x)$ is associated to a source $g_{\mu\nu}(x)$, which is the asymptotic boundary form of the bulk metric $g_{\mu\nu}(u,x)$ at the boundary of AdS

$$\int dx^4\, g_{\mu\nu}(x) T^{\mu\nu}(x). \tag{3.3.9}$$

This makes manifest that any dual of a translationally-invariant gauge theory must involve dynamical gravity.

The previous discussion about the connection between fields of the gravity theory and operators of the dual gauge theory was based on symmetry arguments. It can be made more explicit by looking at the boundary asymptotics

of the gravity fields in a bit more detail. Let us assume that our fields are in the lowest excitation state with respect to the S^5 harmonics, so that they can *de facto* be treated as (4+1)-dimensional fields in AdS_5. In the geometry (3.2.9) a gauge field A_μ can be shown to obey the following asymptotic behaviour close the boundary, $u \to 0$

$$A_\mu(u \to 0, x) = s_\mu + u^2 v_\mu + \dots, \tag{3.3.10}$$

and the relevant part of the typical action of the gravity theory will have the form

$$S \sim \int du \int d^4x \sqrt{\det g}\, F_{\mu\nu} F^{\mu\nu}. \tag{3.3.11}$$

It is then possible to make explicit use of the AdS/CFT prescription (3.3.5), (3.3.6),

$$\left\langle e^{\int dx^4\, \phi_0\, \mathcal{O}} \right\rangle_{\text{CFT}} = e^{-S_{sugra}}\big|_{u=0,\, on-shell}\,, \tag{3.3.12}$$

to compute the vacuum expectation value (vev henceforth) of the current J^μ via

$$\langle J_\mu \rangle = \left. \frac{\delta S_{sugra}}{\delta A_\mu} \right|_{u=0\, on-shell}. \tag{3.3.13}$$

By assuming the relevant supergravity action to be of the form (3.3.11) and taking into account the metric (3.2.9), this can be evaluated to

$$\langle J_\mu \rangle = -\int_{\partial AdS} \left. \frac{\partial \mathcal{L}}{\partial(\partial_u A_t)} \right|_{u=0} \sim L\, v_t, \tag{3.3.14}$$

giving raise to a very concrete interpretation of the terms in the asymptotic expansion (3.3.10): the leading term in the boundary expansion s_μ is the field theory source and the sub-leading term v_μ is the vacuum expectation value of the field theory operator sourced by s_μ.

The derivation we just showed has been done for the case of a gauge field A_μ in AdS_5 but it can be generalised to other kinds of fields in a dimension-independent way [19]. The conclusions drawn from the particular example shown apply in general in gauge/gravity.

3.4 Generalisations of AdS/CFT

3.4.1 Finite temperature and chemical potential

In previous sections we have considered the ground state of the D3-branes, which corresponds to zero temperature. There is a natural generalisation to the non-zero temperature case by replacing the pure AdS metric (3.2.9) by that of the so-called black D3-branes in AdS_5 [63]

$$ds^2 = \frac{r^2}{L^2}\left(-f(r)dt^2 + d\vec{x}^2\right) + \frac{L^2}{r^2 f(r)} dr^2, \tag{3.4.1}$$

or in our u coordinate (3.2.7)

$$ds^2 = \frac{L^2}{u^2}\left(-f(u)dt^2 + d\vec{x}^2\right) + \frac{L^2}{u^2 f(u)}du^2, \tag{3.4.2}$$

where $d\vec{x} = (dx_1, dx_2, dx_3)$ and the blackening factor $f(r)$ or $f(u)$ is

$$f(r) = 1 - \frac{r_h^4}{r^4}, \qquad f(u) = 1 - \frac{u^4}{u_h^4}. \tag{3.4.3}$$

This metric has an event horizon at $r = r_h, u = u_h$. This horizon may be related to the Hawking temperature of the black brane by the conventional method [64], namely by imposing that the Wick rotated space-time $\tau = it$ be regular at the horizon. By regular it is meant that a conical singularity be avoided, which requires that the Euclidean time τ be periodic. As usually, the period is identified with the inverse temperature $\beta = 1/T$ setting the Boltzmann constant to 1, $k_b = 1$. If the near-horizon limit is taken in (3.4.2) by making use of the coordinate

$$\rho^2 = u - u_h, \tag{3.4.4}$$

the metric becomes

$$ds^2 = \frac{L^2}{u^2}\frac{4}{f'(u_h)}\left[\rho^2\left(\frac{f'(u_h)}{2}\right)^2 d\tau^2 + d\rho^2 + \frac{f'(u_h)}{4}\delta_{ij}dx^i dx^j\right]. \tag{3.4.5}$$

Now defining

$$\Phi = \frac{f'(u_h)}{2}, \tag{3.4.6}$$

the metric in the (τ, ρ) plane turns into

$$ds^2 = d\rho^2 + \rho^2 d\Phi^2, \tag{3.4.7}$$

which for regularity requires the periodicity of Φ, $\Phi = \Phi + 2\pi$, otherwise the geometry of space-time would not be regular everywhere. Given the definition (3.4.6), this is tantamount to having $\tau = \tau + \pi u_h$. The period of the euclidian time is the quantity that is identified in thermal field theory with the temperature. By analogy, if we assume a temperature of the boundary gauge theory T, by virtue of the above the duality suggests the identification

$$\beta = \frac{1}{T} = \pi u_h. \tag{3.4.8}$$

The thermodynamic duals in gauge/gravity allow for the definition of further interesting quantities, such as the entropy, which is identified with the Bekenstein-Hawking entropy of the associated black brane, or the free energy. Still, since these quantities are not relevant to our work we do not review them here and refer the reader to [45] for more details about them.

In addition to temperature, another thermodynamic quantity of interest which can be introduced within gauge/gravity duality is a finite density and the associated chemical potential. Let us follow [45] in considering a quantum field theory containing fermionic matter and a $U(1)$ gauge field under which the fermion is charged

$$\mathcal{L} = -\frac{1}{4}F_{\mu\nu}F^{\mu\nu} + i\bar{\psi}\gamma^{\mu}D_{\mu}\psi, \tag{3.4.9}$$

with covariant derivative $D_\mu = \partial_\mu + iA_\mu$ and γ_μ being the Dirac matrices. If the gauge field has a non-vanishing time component $A_t = \mu$, this generates a potential term in the Lagrangian of the form

$$V = -\mu\psi^{\dagger}\psi, \tag{3.4.10}$$

with $\bar{\psi} = \psi^{\dagger}\gamma^0$. This term presents the common form of a density operator with chemical potential μ. Hence in the light of the considerations at the end of section 3.3, it is straightforward to propose that the inclusion of finite density and of a chemical potential be translated into the bulk gravity theory by including a gauge field with a non-vanishing time component A_t whose boundary asymptotic behaviour shall be of the form

$$A_t(u \to 0) \approx \mu - u^2\,\rho + \ldots, \tag{3.4.11}$$

with μ being the chemical potential and ρ being proportional to the density associated to μ. So just as the way of introducing temperature in AdS/CFT is by moving from the pure AdS geometry (3.2.9) to a black brane AdS geometry (3.4.2), finite density and chemical potentials are introduced in the context of gauge/gravity duality by turning on a gauge field in the bulk gravity theory with a non-vanishing temporal component and the proper boundary asymptotic behaviour (3.4.11).

Whenever both possibilities are exploited at a time to have chemical potential and temperature, further regularity conditions imposed by the presence of a black hole horizon must be observed. We will be more explicit about this in section 3.5.

Moreover, the presence of a gauge field that introduces a chemical potential into the game would in principle imply the presence of a radial electric field in the gravity theory, which in the case of non-zero temperature would also imply that the black branes are charged. The degree of complication involved is actually rarely faced, for the familiar physical quantities presented, like the chemical potential, are most often referred to fundamental matter, that is to fields transforming under the fundamental representations of the gauge group not in the adjoint representation as is the case of all the fields in the supergravity multiplet of the D3-branes. The question arises then of how to include fundamental matter in AdS/CFT and we devote the following section to it.

3.4.2 Fundamental matter

As mentioned before, all matter degrees of freedom supported by the stack of D3-branes on which we base our derivation of AdS/CFT transform in the adjoint representation of the gauge group as required by supersymmetry. However, if any connections to the phenomenology of real-world physics are to be made, we are to take contact to fundamental matter, that is to degrees of freedom transforming under the fundamental representations of the gauge group. In the high energy physics jargon one talks about introducing flavour degrees of freedom in analogy to the case of real particles.
There is a rather simple way to do this in AdS/CFT by introducing so-called probe branes in the background geometry sourced by the D3-branes. The open strings stretching between the D3-branes and the probe brane have only one end on the D3-branes and are hence seen as a point-like excitation by an observer living in the world-volume of the D3-branes. This is why such excitations transform in the fundamental representation of the $SU(N)$ gauge group and generate matter in the fundamental representation. To signal how branes are embedded in space-time, tables are used which display along which of the space-time coordinates $x_0, \ldots, x_9$ each brane is extended. For instance, it is usually assumed that the four first directions are the ones along which the D3-branes extend. This is signalled by

	x_0	x_1	x_2	x_3	x_4	x_5	x_6	x_7	x_8	x_9
D3	×	×	×	×	-	-	-	-	-	-

(3.4.12)

If the probe brane can be separated from the stack of D3-branes in some directions transverse to all branes, then the strings stretching between both type of branes must have a minimum length and hence a non-zero energy, which means that the corresponding matter particles are massive. Instead if the probe brane intersects the D3-branes at some point, the minimum length of the strings stretching between it and the D3-branes is zero so that the corresponding matter particles are massless.
Strings with both ends on the flavour brane transform in the adjoint representation of the flavour symmetry group and the dual particles are therefore interpreted as mesons. Strings with only one end on the probe-brane are interpreted as fundamental particles and hence seen as quarks.
In principle the presence of the probe brane should modify the space-time sourced by the D3-branes. Still, as long as we assume that the number of probe branes N_f is much smaller than the number of D3-branes N_c, the back-reaction of the probe branes on the geometry generated by the D3-branes may be neglected. This is called the probe approximation.
A depiction of the position of the probe brane with respect to the stack of D3-branes is shown in figure 3.4.

The low-energy dynamics of a probe Dp-brane in a background created by closed string modes is given by the Dirac-Born-Infeld action, which is usually

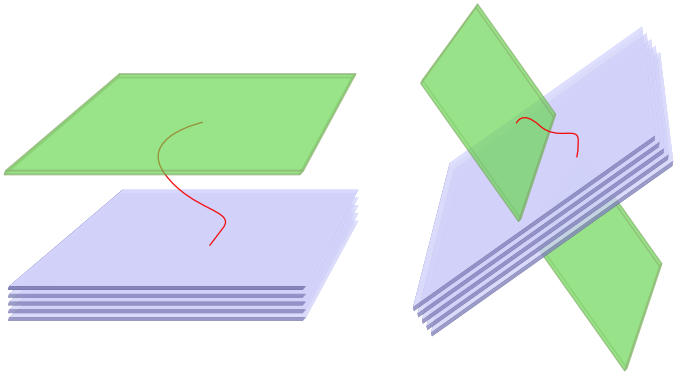

Figure 3.4: Schematic representation of the flavour branes with respect to the stack of D3-branes and the strings stretching between them. Two different configurations are shown. On the left, strings stretching between both kind of branes must have a minimum length and hence a minimum mass, giving rise to a spectrum with massive modes only. On the right, massless strings transforming under the fundamental representation of the flavour group are allowed, since the probe brane intersects the stack of D3-branes and strings of zero length may be present.

referred to as the DBI action. This action is found to lead to the correct equations of motion (see for example [65]). It is a direct analogy of the well-known Nambu-Goto action for the fundamental string based on the world-sheet swept by the string is minimised but now for a higher-dimensional object. Its bosonic part is

$$S = -T_p \int d^{P+1}\xi e^{-\Phi} \sqrt{-\det(P[g] + 2\pi\,\alpha'\,F + P[B])}\,, \tag{3.4.13}$$

where $P[g]$ is the pull-back of the background metric $g_{\mu\nu}$ on the world-volume of the probe Dp-brane

$$P[g] = \gamma_{ab} = \frac{\partial X^\mu}{\partial \xi^a}\frac{\partial X^\nu}{\partial \xi^b} g_{\mu\nu}, \quad \mu,\nu = 0,\ldots,9 \quad a,b = 0,\ldots,p\,, \tag{3.4.14}$$

the X being the space-time coordinates, ξ the embedding coordinates accounting for the transverse fluctuations of the brane, F the field strength of the world-volume $U(1)$ gauge field A_μ

$$F_{\mu\nu} = \partial_\mu A_\nu - \partial_\nu A_\mu, \tag{3.4.15}$$

and $P[B]$ stands for the pull-back of the NS-NS bulk 2-form $B_{\mu\nu}$. The prefactor T_p is known as the brane tension, which must have dimension $p+1$. Dimensional arguments may be drawn to show that

$$T_p = (2\pi)^{-p}\alpha'^{-(p+1)/2}. \tag{3.4.16}$$

See [66] for a detailed derivation. The dilaton field is given by

$$e^{\Phi} = g_s H_p^{\frac{3-p}{4}}, \tag{3.4.17}$$

with

$$H_p(r) = 1 + \left(\frac{r_0}{r}\right)^{7-p}, \tag{3.4.18}$$

stemming from the metric sourced by a black Dp-brane with horizon located at $r = r_p$. For the case of interest $p = 3$, the dilaton takes a constant value, $\Phi = \Phi_0$. If we now consider the action for the fundamental string in the absence of a dilaton potential

$$S \propto \int_\Sigma \Phi\, R\, d^2\sigma = \Phi_0 \int_\Sigma R\, d^2\sigma = \Phi_0(2 - 2G) \tag{3.4.19}$$

where Σ stands for the world-sheet swept by the fundamental string, parametrised by the coordinates σ, R is the curvature of the world-sheet and in the third equality we have made use of the Gauss-Bonet theorem relating the geometry of surfaces to their topology. G is the genus of the corresponding Riemann surface. In the light of this, it is clear by considering Feynmann path integrals

$$e^{-S} \sim e^{-\Phi_0(2-2G)}, \tag{3.4.20}$$

that the dilaton is related to the perturbative expansion of the string, since for a 2-dimensional world-sheet, G gives the order of string perturbation theory

$$e^{\Phi_0} = g_s. \tag{3.4.21}$$

So if for simplicity we consider action (3.4.13) in flat space with $B = 0$[3] and a constant dilaton and expand it using

$$\det(1 + M) = 1 - \frac{1}{2}\mathrm{Tr}\ (M^2) + \ldots, \tag{3.4.22}$$

we obtain to leading order in α'

$$S = -(2\pi\alpha')^2 \frac{T_p}{4g_s} \int d^{p+1}\xi\, \mathrm{Tr}\ F^2, \tag{3.4.23}$$

which is reminiscent of an abelian Yang-Mills action with coupling

$$g_{YM} = \frac{g_s}{T_p(2\pi\alpha')^2} = (2\pi)^{p-2} g_s \alpha'^{\frac{p-3}{2}}. \tag{3.4.24}$$

To analyse the dynamics of a D3/Dp-brane system, we must pay attention to the 't Hooft couplings of the D3-branes

$$\lambda_3 \equiv g^2_{YM(3)} N = 2\pi g_s N, \tag{3.4.25}$$

[3]We always assume $B = 0$ in this thesis if not otherwise specified.

and to that of the probe flavour branes, which in light of (3.4.24) is given by

$$\lambda_p \equiv g^2_{YM(p)} N_f = (2\pi)^{p-2} g_s \alpha'^{\frac{p-3}{2}} N_f. \tag{3.4.26}$$

Hence the quotient signalling the relative importance of the dynamics of the strings with both ends on the flavour brane is

$$\frac{\lambda_p}{\lambda_3} = \frac{N_f}{N} (2\pi)^{p-2} \alpha'^{\frac{p-3}{2}}. \tag{3.4.27}$$

This means that in order for the string starting and ending on the p-brane, the so-called pp-strings, to decouple in the Maldacena limit $\alpha' \to 0$ we must consider $p > 3$. Moreover, the requirement that the probe branes can separate from the stack of D3-branes excludes the case of the D9-brane. This leaves us with D5-branes and D7-branes as proper candidates for a probe brane.
There are some further requirements to be satisfied by the flavour probe branes [45]:

1. The brane intersection must be free from tachyonic modes and supersymmetric.

2. The flavour branes and the colour branes always share the time direction, x^0.

3. The flavour branes extend at least in one of the directions perpendicular to the D3-branes, $x^4, \ldots, x^9$, since they should extend in the radial direction for flavour degrees of freedom to be present at all energy scales.

The D7-brane was for a long time somewhat the canonical choice for a probe brane and has been studied in depth [67, 68, 69, 70]. Our work here though, will mainly deal with the probe D5-brane with finite temperature and chemical potential.

Probe D5-brane at finite temperature

From the above considerations, if the fundamental matter is to be present in some spatial directions, only one of the possible configurations of the D5-brane is to be taken into consideration, namely

	x_0	x_1	x_2	x_3	x_4	x_5	x_6	x_7	x_8	x_9
D3	×	×	×	×	-	-	-	-	-	-
D5	×	×	×	-	×	×	×	-	-	-

(3.4.28)

which is indeed the configuration we shall be working with. According to it, there is one direction in which the D3-branes extend but the D5-branes not, which implies that the fundamental matter fields are constrained to live in 2+1 dimensions out of the 3+1 dimensions of the dual gauge theory fields to which they couple. This is why such a field theory is called a defect field theory. The

degrees of freedom in the fundamental representation only exist along a defect, that is a plane in the x_0, x_1, x_2 directions.

In addition to the DBI-action (3.4.13), the presence of the $C^{(4)}$ of Type IIB supergravity makes it in general necessary to include a Chern-Simons term in the action accounting for its coupling to the $U(1)$ gauge field on the probe brane. In the case of the D5-brane, this extends the action to

$$S = S_{DBI} + S_{CS} = S_{DBI} + \frac{T_p}{g_s}\frac{(2\pi\alpha')^2}{2}\int_{\partial W} P[C^{(4)}] \wedge F. \tag{3.4.29}$$

A form of $C^{(4)}$ which is known to provide a solution to the equations of motion of supergravity is

$$C^{(4)} = \left(\frac{1}{H_3(r)} - 1\right) d\xi^0 \wedge \cdots \wedge d\xi^3 + \ldots \tag{3.4.30}$$

with $H_3(r)$ given by (3.4.18). The dots in the previous equation stand for the extra term that ensures that the self-duality condition (3.2.2) is fulfilled. In our configuration, the pull-back of the four-form vanishes.[4] This allows us to neglect the Chern-Simons term of the action, thus the bosonic low-energy dynamics of a probe D5-brane as in (3.4.28) is hence described by the action

$$S = -N_f T_{D5} \int d^6\xi \, \sqrt{-\det(P[g] + 2\pi\,\alpha'\,F)}\,, \tag{3.4.31}$$

from which its dynamics can be derived.

For considering a probe D5-brane at finite temperature, we must embed it as described above in the background generated by the stack of black D3-branes (3.4.2). A more convenient description can be used by introducing the coordinates [68]

$$z^2 = \frac{2\,L^4}{u^2 + \sqrt{u^4 - u_0^4}}, \tag{3.4.32}$$

after which the metric takes the form

$$ds^2 = \frac{L^2}{z^2}\left(-\frac{f(z)^2}{h(z)}\,dt^2 + h(z)\,d\vec{x}^2 + dz^2\right) + L^2\,d\Omega_5^2\,, \tag{3.4.33}$$

where $\vec{x} = (x_1, x_2, x_3)$, $d\Omega_5^2$ is the metric of a unit radius S^5, and

$$f(z) = 1 - \frac{z^4}{z_0^4}\,, \qquad h(z) = 1 + \frac{z^4}{z_0^4}\,. \tag{3.4.34}$$

[4] The topological term might be activated by assuming a different form of $C^{(4)}$ as in [26].

This geometry becomes asymptotic to $AdS_5 \times S^5$ in the small z limit, with the boundary of AdS_5 being at $z = 0$, while it presents a horizon at $z = z_0$. Accordingly, the Hawking temperature of the black hole reads

$$T = \sqrt{\frac{2}{\pi}}\, z_0 \,. \tag{3.4.35}$$

It is useful to define the dimensionless coordinates

$$(\tilde{z}, \tilde{x}_\mu) = \frac{1}{z_0}(z, x_\mu) \,, \tag{3.4.36}$$

in terms of which the metric takes the form (3.4.33) with $z_0 = 1$. From now on we always use these dimensionless coordinates and drop the tilde for presentational purposes.

Furthermore the embedding is better described by writing the metric of the S^5 in terms of two S^2 as follows

$$d\Omega_5^2 = d\theta^2 + \sin^2\theta\, d\Omega_2^2 + \cos^2\theta\, d\tilde{\Omega}_2^2 \,. \tag{3.4.37}$$

Thus (3.4.28) turns into

	t	x_1	x_2	x_3	z	Ω_2	$\tilde{\Omega}_2$	θ
D3	$\times$	$\times$	$\times$	$\times$				
D5	$\times$	$\times$	$\times$		$\times$	$\times$		

(3.4.38)

where the D5-brane shares two Minkowski directions with the D3-branes generating the background, is extended along the radial direction z, and wraps an S^2 (Ω_2) inside the S^5, while it is located at a fixed point of the remaining S^2 ($\tilde{\Omega}_2$). The embedding is then described by the coordinate θ, which determines the radius of the S^2 wrapped by the D5-brane. In order to simplify the analysis we define

$$\cos\theta = \chi \,, \tag{3.4.39}$$

in terms of which we describe the embedding. Thus the form of χ as a function of space-time coordinates determines the separation between the probe flavour brane and the stack of D3-branes. This separation is naturally related to the mass of the fundamental matter particles or quarks. If the probe brane is separated from the D3-branes in some of the transverse directions to both branes, the minimum length of a string stretching between the branes has a non-zero energy and the dual quarks are massive. This is confirmed by the equations of motion derived from (3.4.31). From them, it is possible to show that the field containing the information about the embedding, χ, asymptotically behaves close to the AdS boundary ($z \to 0$) as

$$\chi = mz + \psi z^2 + \mathcal{O}(z^3) \tag{3.4.40}$$

$$m = \frac{2\sqrt{2}}{\pi\sqrt{\lambda}} \frac{M_q}{T} \,. \tag{3.4.41}$$

with $\sqrt{\lambda} = L^2/(\sqrt{2}\alpha')$. The dimensionless constant m is proportional to the quantity that is dual to the quark mass [71, 72]. The precise relation is derived in detail in [72, 73]
Since this work considers models at finite chemical potential, we now want to add the necessary ingredients to account for it.

Adding finite chemical potential

As elucidated above, in order to introduce a chemical potential holographically, we must turn on the temporal component of a gauge field as in (3.4.11). If we want our chemical potential and the associated charge density to be referred to the fundamental matter particles, this gauge field cannot be anything but the $U(1)$ gauge field living on the world-volume of the probe brane. We assume it to be

$$A = A_t \, dt. \tag{3.4.42}$$

Since it is mostly preferable to work with dimensionless quantities, we define

$$\phi = 2\pi\alpha' \frac{z_0}{L^2} A_t \,, \tag{3.4.43}$$

from whose asymptotic boundary expansion

$$\phi = \mu - \frac{\pi}{\sqrt{2}} T \, \rho \, z + \mathcal{O}(z^2) \tag{3.4.44}$$

it is possible to obtain the dual chemical potential μ and the associated charge density ρ.
Note that we are working in a black brane geometry (3.4.33) with an horizon at $z = z_0$. The physics of black holes dictates some extra conditions that affect the fields present in the geometry. As pointed out in [67], the event horizon at $z = z_0$ is a Killing horizon, which means that it is a surface where the Killing vector field ∂_t becomes null. For the gauge field A to be well defined as a one-form it is then necessary that its time component be zero there. This can also be seen by considering the necessity that $g^{\mu\nu} A_\mu A_\nu = g^{tt} (A_t)^2$ not be infinite, which can only be true if

$$A_t(z = z_0) = \phi_t(z = z_0) = 0. \tag{3.4.45}$$

Additionally, as can be seen from the asymptotic horizon expansion of the equations of motion derived from (3.4.31), the embedding field χ must fulfil in this geometry

$$\partial_z \chi(z = z_0) = 0. \tag{3.4.46}$$

The last two restrictions reduce the number of free parameters of the fields A and χ in (3.4.40) and (3.4.44) from four down to two. This means that the

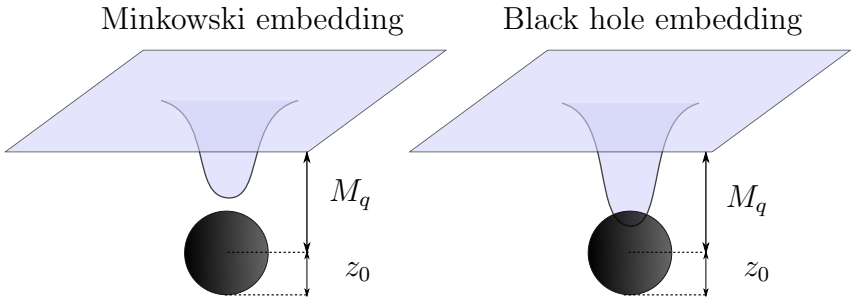

Figure 3.5: Illustration of the two possible types of embedding in the black brane geometry. On the left, a Minkowski embedding, in which the brane terminates in the radial direction before reaching the horizon. In that situation the fundamental matter particles have a minimum mass. On the right, a black hole embedding, in which the brane does reach the black hole horizon thereby allowing for massless fundamental modes. The parameter M_q, interpreted in the dual field theory as the quark mass, is given by the distance between the probe brane and the stack of D3-branes, which is located at $z = 0$. The event horizon of the black-brane geometry is at $z = z_0$.

solutions to the equations of motion are characterised by the choice of two parameters, which we may take to be m and μ.

The phenomenology of Dp/Dq brane intersections at finite temperature and chemical potential has been thoroughly studied over the last years, see for instance [74, 75, 76] and references therein. Analyses of finite temperature set-ups with probe D7-branes [77, 71] and probe D5-branes [78] have established two qualitatively different embeddings: those in which the brane ends before reaching the black hole horizon, denoted Minkowski embeddings, and those in which the brane reaches the horizon, called black hole embeddings. Both kinds of embedding are illustrated in figure 3.5. In our case, the precise choice of m and μ determines what kind of embedding we have. Minkowski embeddings exist above a certain value of the mass, while black hole embeddings are possible for any mass [68]. At non-zero charge density only BH embeddings are possible. As explained in [67], the fundamental strings realizing the charge density would have nowhere to end in a Minkowski embedding. The resulting phase diagram is shown in figure 3.6. For a large enough M_q/T, BH embeddings exist only above a non-zero chemical potential μ. In particular, the shaded region in the plot is only accessible by Minkowski embeddings, which have zero charge density.
Since our work focuses on embeddings with both temperature and charge density, we will exclusively deal with embeddings of the black hole type. This restricts our choice of the parameter pair m, μ to those corresponding to points in the non-shaded area of figure 3.6.

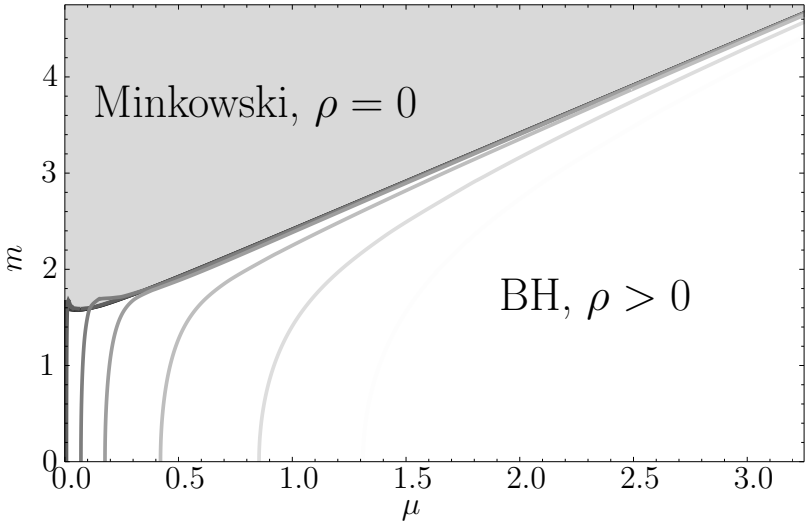

Figure 3.6: Quark mass $m = M_q/T$ versus chemical potential μ for black hole embeddings corresponding to various values of the charge density ρ, decreasing from right to left: $\rho = 2$, 1.25, 0.6, 0.25, 0.1, 0.01, 10^{-4}, 10^{-6}. The shaded area is not accessible by black hole embeddings, and is asymptotically delimited (at large μ) by $m > 1.00\mu + 1.41$. In the inlay we zoom in on the region of low μ.

3.5 Applications of AdS/CFT to condensed matter physics

As anticipated, one of the big advantages of AdS/CFT is its paving the way to a better understanding of many phenomena in strongly coupled matter theories which are otherwise not accessible to calculation. This is made possible by the weak/strong character of the duality, which we presented above. In the long run, the hope is to relate it to theories such as QCD and condensed matter systems. There are indeed many interesting physical systems in condensed matter physics still lacking a complete theoretical description due to its strong coupling. Most of these theories are far from being the ones we can relate to gauge/gravity, since they are not gauge theories with a large number of colours, nor are they infinitely strongly coupled. They are moreover mostly non-relativistic theories, as opposed to the ones considered in our presentation of the duality. Nevertheless, the main idea is to exploit universality to link AdS/CFT to real world physics. This idea relies on the assumption that even though real world theories and the theories involved in AdS/CFT may be far apart, they might share some common features which are universal to a wide range of theories and whose exploration via gauge/gravity could enhance our understanding of the former. A canonical example is the computation of the relation shear viscosity over entropy density

$$\frac{\eta}{s} = \frac{1}{4\pi}\frac{\hbar}{k_b}, \tag{3.5.1}$$

with η being the shear viscosity coefficient and s the entropy density. This result was computed within gauge/gravity [21] and is common to all strongly coupled theories with a gravity dual involving the Einstein-Hilbert action coupled to matter fields. Experimental measurements of this ratio in a strongly coupled fluid resulting from heavy ion collisions known as the quark gluon plasma at the Relativistic Heavy Ion Collider (RHIC), at Brookhaven National Laboratory near New York and at the LHC in Geneva display good agreement with this predicted value. This behaviour is remarkably different to the one predicted for weakly coupled fluids and for common fluids such as water or liquid helium. This celebrated result is considered to be one of the greatest successes of gauge/gravity duality up to date, given that it is the first example of a theoretical prediction by gauge/gravity which has been confirmed experimentally. It gives us hope that gauge/gravity may indeed be seen as a tool that may provide us a better understanding of strongly coupled matter.

Along this lines it is interesting to exploit the duality to test models wich can be linked to strongly coupled condensed matter systems. In order to do so though, we must know how to compute observables which have a concrete interpretation within the dual gauge theory. One of the most common quantities computed in applications of AdS/CFT to condensed matter physics is the optical conductivity, measuring the response of the charge current to an applied electric field. Since conductivity computations constitute the core of our work, we want to pay close attention to them.

3.5.1 Holographic optical conductivity

The optical conductivity, also denoted AC conductivity (σ) is understood here as within the linear response formalism in the context of the well-known Ohm's law, which relates the spatial electric current in a medium $\vec{J}$ to the electric field $\vec{E}$

$$\vec{J} = \sigma \vec{E}. \tag{3.5.2}$$

As we saw in section 3.3, the introduction of a spatial current along one of the directions of the gauge theory, say J_x, requires the presence of a dual bulk theory gauge field that acts as a source, A_x. We introduce an electric field of frequency ω by considering

$$E_x = F_{tx}|_{z=0} = i\omega \mathfrak{e}_x e^{i\omega t}, \tag{3.5.3}$$

where $\mathfrak{e}_x$ is the modulus of the electric field. Assuming that the fields only depend on the radial coordinate z we find

$$E_x = F_{tx}|_{z=0} = (\partial_t A_x - \partial_x A_t)|_{z=0} = \partial_t A_x|_{z=0} = i\omega \mathfrak{e}_x e^{i\omega t}, \tag{3.5.4}$$

Now if the boundary asymptotic behaviour of A_x is

$$A_x(z \to 0) = A_x^{(0)} + z A_x^{(1)} + \ldots, \tag{3.5.5}$$

we know

$$A_x^{(0)} = \mathfrak{e}_x e^{i\omega t}. \tag{3.5.6}$$

and know from our previous discussion (3.3.14) that the sub-leading term $A_x^{(1)}$ corresponds to the vacuum expectation value of the current sourced by the leading term $A_x^{(0)}$. So assuming that we are in a gauge where $A_z = 0$, we can apply Ohm's law

$$\sigma(\omega) = \frac{\langle J_x \rangle}{E_x} = \lim_{z\to 0} \frac{F_{xz}}{F_{tx}} = -\frac{\partial_z A_x}{\partial_t A_x} = -\frac{A_x^{(1)}}{i\omega \mathfrak{e}_x e^{i\omega t}} = \frac{j_x}{i\omega \mathfrak{e}_x}. \tag{3.5.7}$$

In the last equality we have redefined $A_x^{(1)} = -j_x e^{i\omega t}$. Note that the third expression in the equation involves only the field-strength tensor and therefore defines the conductivity in a gauge invariant way. This is indeed the definition we shall be using later on

$$\sigma(\omega) = \lim_{z\to 0} \frac{F_{xz}}{F_{tx}}. \tag{3.5.8}$$

The last two equations show how to compute a holographic conductivity once the solution for the gauge field A_x is known. To obtain this solution the corresponding equations of motion must be solved paying attention to the proper boundary conditions. Again, in the presence of a black hole such boundary conditions must guarantee the preservation of causality, which requires that no information escapes the event horizon. This is formally implemented by means of the so-called in-falling wave boundary condition at the horizon. Consider the metric (3.4.33)

$$ds^2 = \frac{L^2}{z^2}\left(-\frac{f(z)^2}{h(z)}\,dt^2 + h(z)\,d\vec{x}^2 + dz^2\right) + L^2\,d\Omega_5^2\,, \tag{3.5.9}$$

which has a coordinate singularity at $z = z_0 = 1$ (see (3.4.36)). In order to study causality issues we must analyse light-like geodesics and for this purpose it is convenient to switch to the tortoise coordinate

$$z^* = \pm \int_1^z \sqrt{\frac{h(z)}{f(z)^2}}dz, \tag{3.5.10}$$

which reminding ourselves of (3.4.34) is in the vicinity of the black hole horizon

$$z^* = \pm\frac{\log(1-z)}{2\sqrt{2}} \pm \frac{1-z}{2\sqrt{2}} + \mathcal{O}(1-z)^2. \tag{3.5.11}$$

In these coordinates, light-like plane waves moving towards and from the horizon in the radial direction correspond to a behaviour of the form $e^{i\omega(t\pm z^*)}$. Since causality requires that nothing escapes the black hole, we discard the

solutions with a negative sign. Going back to the original coordinates, we see that our causal in-falling waves take the form

$$e^{i\omega(t+z^*)} = e^{i\omega t}(1-z)^{i\alpha}\left(a^{(0)} + a^{(1)}(1-z) + \mathcal{O}(1-z)^2\right), \tag{3.5.12}$$

with

$$\alpha = \frac{\omega}{2\sqrt{2}}, \tag{3.5.13}$$

and

$$\frac{a^{(1)}}{a^{(0)}} = \frac{i\omega}{4\sqrt{2}}. \tag{3.5.14}$$

Thus the last three equations correspond to the ansatz we must take for the horizon boundary condition in order for causality to be preserved there. It has also been shown that this boundary condition corresponds to the selection in the dual field theory of the retarded Green's function, which is the one ensuring causal propagation there [79].

3.5.2 Top down vs bottom up and what things really are

In this chapter we have seen how AdS/CFT is motivated by Type IIB supergravity. The field spectrum of the theory is made up of a bosonic sector consisting of two scalars (axion and dilaton), two 2-forms (one is obtained by squaring the vectors and the other one by squaring the spinors), a self-dual 4-form and the metric.

Type IIB SUGRA			
BOSONIC SECTOR			
$[2,0,0,0]_8$	$2\times[0,1,0,0]_8$	$2\times[0,0,0,0]_8$	$[0,0,0,2]_8$
$g_{\mu\nu}$ (35)	$A^{(2)}_{\mu\nu}, B^{(2)}_{\mu\nu}$ (2×28)	ϕ, C (2×1)	$C^{(4)+}_{\mu}$ (35)
graviton	2-forms	dilaton, axion	4-form (self-dual)
FERMIONIC SECTOR			
	$2\times[0,0,1,0]_8$	$2\times[1,0,0,1]_8$	
	$2\times\psi_{\alpha}$ (2×8)	$2\times\psi_{\mu\dot{\alpha}}$ (2×56)	
	2 gravifermions	2 gravitini	

When using AdS/CFT to produce models for condensed matter systems there are two main roads one can follow. One approach consists in departing from the 10-dimensional Type IIB theory, in general setting some of the fields of the theory to zero, and then trying to find the dual field theory Lagrangian that enables a proper interpretation of physical quantities on both sides of the duality. This approach, which goes under the name of *top-down* has the advantage of being somewhat authentic, in the sense that the resulting theories stem from the original Type IIB supergravity theory on which the formulation

of the duality is based.
Another possible approach, called *bottom-up*, relies on the use of simpler gravity actions, mostly in four or five dimensions. We already saw that the transition to five dimensions can be done by dimensionally reducing the theory on S^5 to produce an effective five-dimensional theory with the corresponding effective Lagrangian by means of a Kaluza-Klein reduction. This is done by expanding the 10-dimensional fields in terms of a complete set of harmonics in the internal space (3.2.16). The reduced effective theory are equivalent to the higher dimensional one and will contain and infinite tower of massive states. In the simple compactifications, the massive modes can be decoupled by taking the compact dimension to be very small. Indeed, for small compact dimensions, all particles are heavy except for the massless zero modes. If we are probing distance scales much bigger than R, they can be ignored. On behalf of consistency though, such actions must be shown to be a consistent truncation of Type IIB supergravity. A consistent truncation is a non-linear reduction of the original theory such that the solutions of the lower dimensional equations of motion necessarily solve the original equations of motion.

The models considered in this thesis, using the set-up presented in section 3.4.2, are based on the geometry sourced by the stack of N D3-branes, that is the metric, $g_{\mu\nu}$ and the self-dual four-form $C^{(4)}$ under which the branes are charged. We furthermore consider the $U(1)$ gauge field supported on the world-volume of the D5 flavour brane and assume that the rest of the fields on that world-volume, namely the scalar fields accounting for the fluctuations of the brane and the fermionic supersymmetric partners are set to zero. We do not consider the backreaction of the D5-brane upon the background geometry, since we stay within the so-called probe approximation. All other fields in the theory, that is the two-forms, the scalars and the entire fermionic sector are assumed to be zero. The solutions found are hence solutions to the Type IIB supergravity action under the condition that all these fields are set to zero. The corresponding dual gauge theory Lagrangian is known, see section 10.4. of [45].

A further issue to take into consideration is that we want our physical systems to be stable. This requirement was ensured by the choice of the embedding (3.4.38). However the introduction of a temperature implies the existence of a scale in the theory which breaks conformal invariance and hence supersymmetry. The presence of supersymmetry generally guarantees the stability of a physical system so that in its absence we cannot be certain that the physical system at hand is stable. This ought to be verified separately.

All in all, we must keep in mind that our models, while consistently based on the original Type IIB supergravity theory in a top-down approach, are subject to a number of caveats. Apart from the stability issue, it is worth reminding ourselves that since we are using the weak form of the duality,

the dual gauge field theory has an infinite number of colours and is at very strong coupling. Nevertheless, as already mentioned, it is interesting to study such systems in the hope that universal properties common to more realistic strongly coupled systems be unveiled. In any case, the holographic models we deal with might pave the way to a better understanding of the phenomenology of strongly coupled systems.

Chapter 4

Numerical computations using spectral methods

Given that most of the results of this thesis have been obtained by means of numerical computations, we consider it appropriate to devote a chapter to the techniques used to this purpose, the so-called spectral methods. This thesis would not be complete without it. Yet presenting a complete review of the broad field of pseudospectral methods as a tool for solving partial differential equations is far beyond the scope of this thesis. The reader wanting to learn more about them is referred to some of the very good existing references in the literature [80, 81]. Instead, we would like to offer an introduction to the general idea of pseudospectral methods with special emphasis on those aspects which are most relevant for holographic computations in general and in particular for this work.
The results obtained in this thesis have all been produced using Mathematica[1] and explicit reference is given to the concrete Mathematica functions where appropriate so as to facilitate the reproduction and extension of our results. Examples are provided which are directly related to our final codes, schematic versions of which are shown in appendix D. The reader may feel free to use them, adapt them or reproduce them.

Before going to the matter though, let us point out that having to resort to complicated codes to solve equations is not something a physicist generally does for the fun of it but rather because of it being the only feasible way. In many AdS/CFT applications to condensed matter systems, specially in those aiming at reproducing realistic every day situations, one has to renounce to more and more symmetries, like for example, translational symmetry, which is very often not present in condensed matter systems. This is indeed the case in systems with disorder or impurities, to which this work is devoted. The involved fields do not only depend on the radial AdS coordinate as usually but

[1] Wolfram Research, Inc., Mathematica, Version 9.0, Champaign, IL (2012).

also on at least one spatial coordinate. This turns the equations of motion of the fields into partial differential equations (PDEs), whose analytical resolution is only possible in a very reduced number of highly symmetric cases. Beyond those cases, such PDEs cannot be solved analytically and numerics poses the only realistic way of attacking the problem.

4.1 Discretisation and differentiation matrices

Computers cannot cope with an infinite amount of data. This excludes the possibility of using them to perform numerical computations in a continuum. Whenever a computer comes into play, things have to be discretised. Space-time is no exception to this statement. The discretisation of space-time implies that only a finite amount of space-time points is used in the calculations, thereby reducing space-time to a grid of points at which functions of space-time take a numerical value. The more points one uses for such computations, the more trustworthy the discrete approximation of continuum space-time is. But only at the cost of computational resources, for more points also mean more required computing power and longer computation times. Hence the art consists in finding an equilibrium between affordable computation conditions and precision.
Once space-time has turned into a collection of discrete points at which the known functions are evaluated, the question arises of how this data can be used to estimate derivatives. The method most probably striking the mind of the reader is that of finite differences. Let us assume that a 1-dimensional space described by the spatial coordinate x is discretised in a uniform grid of 3 points $\{x_0, x_1, x_2\}$ with an interval $x_{i+1} - x_i = h$ for each i. A function of x, say $f(x)$ will correspondingly take numerical values at each of the grid points $\{f_0, f_1, f_2\}$. The question is how to estimate the value of $f'(x)$ at the gridpoints. The simplest possible method is the second-order difference approximation, which assumes

$$f'_i = \frac{f_{i+1} - f_{i-1}}{2h}. \tag{4.1.1}$$

Following this rule and assuming on behalf of simplicity periodic boundary conditions, in our simple case with only three grid points, the vector containing the values of the derivative of a function f with respect to x at each of the grid points is obtained from the vector containing the value of the function itself at those points via a matrix

$$\begin{pmatrix} f'_0 \\ f'_1 \\ f'_2 \end{pmatrix} = \frac{1}{h} \begin{pmatrix} 0 & \frac{1}{2} & -\frac{1}{2} \\ -\frac{1}{2} & 0 & \frac{1}{2} \\ \frac{1}{2} & -\frac{1}{2} & 0 \end{pmatrix} \begin{pmatrix} f_0 \\ f_1 \\ f_2 \end{pmatrix}. \tag{4.1.2}$$

Such a matrix is called a differentiation matrix. This has been a very basic example, in which the order of convergence would be just $\mathcal{O}(h^2)$, but the main idea is that of defining differentiation matrices to implement differentiation in

a discrete grid of points once a discrete differentiation method like (4.1.1) has been chosen.

It is in our interest to notice that (4.1.1) could have been found in a different way. Knowing $\{f_0, f_1, f_2\}$ one could have made use of polynomial interpolation to get a continuum estimate of the function f. To this end, the well known polynomial interpolation formula by Lagrange may be used

$$p(x) = \sum_{i=0}^{N} \left(\prod_{\substack{1 \le j \le N \\ j \neq i}} \frac{x - x_j}{x_i - x_j} \right) f_i, \tag{4.1.3}$$

to obtain for our simple case that for each i

$$f(x) \simeq \frac{(x - x_i)(x - x_{i+1})}{2h^2} f_{i-1} - \frac{(x - x_{i-1})(x - x_{i+1})}{h^2} f_i + \frac{(x - x_{i-1})(x - x_i)}{2h^2} f_i. \tag{4.1.4}$$

Differentiating and evaluating at $x = x_i$ then gives (4.1.1).
It being so, the natural way of increasing the order of the finite difference approximation to the derivative is made evident. It suffices to take a polynomial of higher order in (4.1.3). So for a more involved example, if we discretise space-time in a grid of $N + 1$ points $\{x_0, \dots x_N\}$, the differentiation matrix of the fourth-order analogue of (4.1.2) can be found to be

$$\begin{pmatrix} f_0' \\ \\ \\ \vdots \\ \\ \\ f_{N-1}' \end{pmatrix} = \frac{1}{h} \begin{pmatrix} & & \ddots & & & \frac{1}{12} & -\frac{2}{3} \\ & & \ddots & -\frac{1}{12} & & & \frac{1}{12} \\ & & \ddots & \frac{2}{3} & \ddots & & \\ & & \ddots & 0 & \ddots & & \\ & & \ddots & -\frac{2}{3} & \ddots & & \\ & & & \frac{1}{12} & \ddots & & \\ -\frac{1}{12} & & & & \ddots & & \\ \frac{2}{3} & -\frac{1}{12} & & & \ddots & & \end{pmatrix} \begin{pmatrix} f_0 \\ \\ \\ \vdots \\ \\ \\ f_{N-1} \end{pmatrix}, \tag{4.1.5}$$

where omitted entries are zeroes.
Note that both in the latter example case and in the previous one, we could have taken a higher order interpolation. In particular the highest possible order of interpolation is fixed by the number of points in the grid, $N + 1$.
Now the machinery is laid down for converting derivatives into matrices and having every element of our equations in a discrete form. The fundamental working principle is based on taking a given set of discrete data on a grid, choosing an interpolating method and then using the interpolant to evaluate derivatives on the grid. Recall that an interpolating approximation to a function f is nothing but a polynomial expression p whose $N+1$ degrees of freedom are determined by the requirement that it agree with f at a set of $N + 1$ interpolation points [80].

In our previous simple example, we introduced Lagrange's famous method of interpolating a function, which makes use of fundamental algebraic polynomials of the form $p(x) = a_0 + a_1 x + \cdots + a_N x_N$. We also used a grid of evenly spaced points, although this is no necessary restriction. It turns out that such a configuration generally works quite badly to approximate functions by interpolation. In spite of what intuition might suggest, convergence is not always guaranteed as the number of grid points $N+1$ is increased and it may indeed even get worse and worse. This phenomenon, which was shown by Runge and bears nowadays his name, is illustrated in figure 4.1, from which it is evident that the problematic points are the ones near the ends, not the ones in the middle of the interval. This already suggests the possibility of distributing the interpolation points so that their density is higher near the extrema of the interval than in the central region, namely in an unevenly spaced way. Still, since, as seen in fig 4.1, the unwanted oscillations of the interpolating polynomial increase with increasing N, it is somewhat reasonable to think that the squeezing of the points should increase with N. As to how exactly the uneven spaced points ought to be distributed, the answer is provided by the Chebyshev minimal amplitude theorem, by virtue of which the error in the interval of interpolation is minimised for an interpolation of degree N by letting the interpolation points be the roots of the Chebysehv polynomial of degree $N+1$, $T_{N+1}(x)$, which are given by

$$x_j = \cos\left[\frac{(2j+1)\pi}{2(N+1)}\right] \qquad j = 0, 1, \ldots, N. \tag{4.1.6}$$

This can be shown by exploiting the property $T_n(\cos\theta) = \cos(n\theta)$.
Closely related to Chebyshev roots and displaying equally good stability and accuracy properties are the so-called Chebyshev extreme points, or Chebyshev-Gauss-Lobatto points, which we, like many others, shall be calling just Chebyshev points. They are the extrema of the Chebyshev polynomials and are given by

$$x_j = \cos\left(\frac{j\pi}{N}\right) \qquad j = 0, 1, \ldots, N. \tag{4.1.7}$$

The effect of using a grid of Chebyshev points for polynomial interpolation can be dramatic, as is shown in figure 4.2, which is intended to be compared to figure 4.1. We see that the wild oscillations of the interpolant at the edges of the interval characteristic of the Runge phenomenon are not present for a grid of Chebyshev points and more and more accuracy is gained for bigger and bigger N. Indeed this key idea of strategically "collocating" the grid-points is the very essence of pseudospectral methods.

It being so, it is clear how to proceed from now on. We shall be working with grids of $N+1$ Chebyshev points (4.1.7) and use them to construct differentiation matrices by means of the interpolating polynomial of the highest possible order, namely N. Then the interpolant can be derived and evaluated

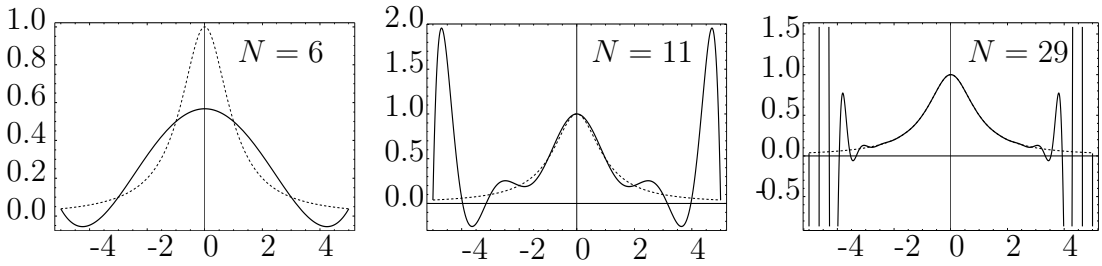

Figure 4.1: Example of the Runge phenomenon for polynomial interpolation on a grid of evenly spaced points. The function to be interpolated is $\frac{1}{1+x^2}$ (dashed line) and we shown from left to right the cases with 6, 11 and 29 interpolation points. As more and more points are used, the error gets worse and worse near the end points.

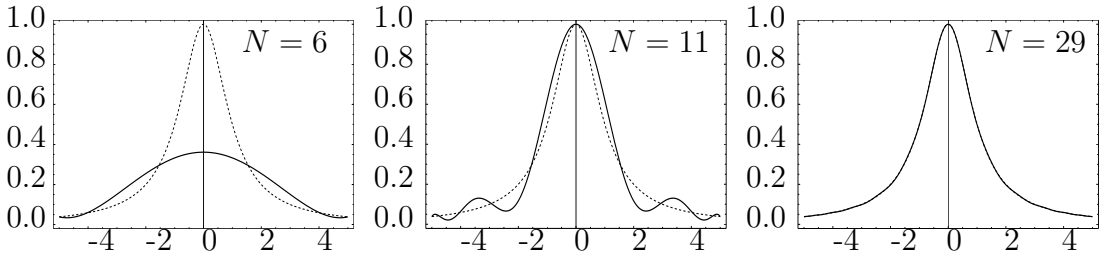

Figure 4.2: Same interpolation cases as in figure 4.1 but using a grid of Chebyshev points instead of evenly spaced ones. It can be seen, that the Runge phenomenon is not present, and indeed convergence improves for increasing number of points N.

at the grid points, which delivers the numerical values of the derivative. The formulas for the entries of the corresponding Chebyshev differentiation matrix are just a combination of (4.1.3) and (4.1.7) used in the way made explicit by the two examples above (4.1.2) and (4.1.5) and pose no mystery at all. They are actually known for any N. For each N, the rows and columns of the corresponding differentiation matrix are given by

$$
\begin{aligned}
(D_N)_{00} &= \frac{2N^2+1}{6}, \qquad (D_N)_{NN} = -\frac{2N^2+1}{6}, \\
(D_N)_{jj} &= \frac{-x_j}{2(1-x_j^2)}, \qquad j = 1, \ldots, N-1, \\
(D_N)_{ij} &= \frac{c_i}{c_j}\frac{(-1)^{i+j}}{(x_i - x)j)}, \qquad i \neq j, \qquad i, j = 0, 1, \ldots, N, \\
c_i &= \begin{cases} 2, & i = 0 \text{ or } N, \\ 1 & \text{otherwise.} \end{cases}
\end{aligned}
\tag{4.1.8}
$$

Which, brought into order and schematically put into matrix form results in

$$D_N = \left(\begin{array}{c|c|c} \frac{2N^2+1}{6} & 2\frac{(-1)^j}{1-x_j} & \frac{1}{2}(-1)^N \\ \hline -\frac{1}{2}\frac{(-1)^i}{1-x_i} & \frac{(-1)^{i+j}}{x_i-x_j} \quad \frac{-x_j}{2(1-x_j^2)} \quad \frac{(-1)^{i+j}}{x_i-x_j} & \frac{1}{2}\frac{(-1)^{N+i}}{1+x_i} \\ \hline \frac{1}{2}(-1)^N & -2\frac{(-1)^j}{1+x_j} & -\frac{2N^2+1}{6} \end{array}\right). \tag{4.1.9}$$

Of course the domain of interest will not always range between -1 and 1 as the Chebyshev points. We may want it, for instance, to represent an AdS radial coordinate ranging between 0 and 1. In that case, there is nothing wrong in rescaling the grid of Chebyshev points so that it starts at the desired point and has the length one wishes, as long as the corresponding differentiation matrices are rescaled accordingly. Hence if we take our grid of Chebyshev points (4.1.7) ranging from -1 to 1 and perform the rescaling

$$z_j = ax_j + b, \tag{4.1.10}$$

it is clear that the domain we work in will now range from $z_0 = b - a$ to $z_L = b + a$, where a is related to the desired length of the system $L = 2a$ and b locates the middle point of the interval. Now for this scaling to be consistent, and for the differentiation matrix D_N (4.1.9) to be still valid, it is clear that the latter must be rescaled by a factor of a

$$\bar{D} = D_N/a, \qquad \text{so that} \qquad D_N \cdot x = \bar{D}_N \cdot z\,. \tag{4.1.11}$$

Fortunately, such differentiation matrices are pre-built in most of the scientific programming software, so that one often needs not deal with the cumbersome definitions. In the case of Mathematica, once the grid of Chebyshev points (4.1.10) has been defined at will

```
ChebPoints[z0_,L_,n_Integer/;n>1]:=z0+L/2 (1-Cos[Pi Range[0,n-1]/(n-1)]);
grid = ChebPoints[z_0, L, Npoints]//N;
```

the corresponding derivative of a discretised function can be computed by means of the differentiation matrix $\bar{D}_N$, which may be invoked in Mathematica as

```
d[1] = NDSolve`FiniteDifferenceDerivative[{1},{grid},
"DifferenceOrder" -> {"Pseudospectral"}, PeriodicInterpolation -> {False}],
```

and so given a set of numeric data `phi` standing, say, for a field ϕ discretised on the defined grid of Chebyshev points `grid`, the numeric version of $\partial_x\phi$ may be called upon by means of

```
d[1][phi]
```

As it is, most physical cases of interest are not in just 1 dimension but rather in a least 2-dimensional spaces and the equations mostly involve more than just first derivatives. As to how to deal with higher derivatives, the matter is solved quickly by just thinking of the second derivative as a succession of two first derivatives. If the first derivative is obtained by means of the derivative matrix D, the second derivative is obtained by just letting D^2 act. The differentiation matrix for the second derivative can be defined in Mathematica for the grid of Chebyshev points `grid` as

```
d[2] = NDSolve`FiniteDifferenceDerivative[{2},{grid},
"DifferenceOrder" -> {"Pseudospectral"}, PeriodicInterpolation -> {False}].
```

While the accuracy of the numerical approximation is smaller for higher derivatives, most physical problems do not require the use of derivatives higher than the second or at most the third, which in practice turns out to be good enough. Still, it is good practice to redefine fields when possible so that quantities of interest are computed in terms of functions and not of its derivatives.[2]
The second issue is that of adapting our machinery to 2-dimensional spaces, which are relevant for this work. There is a natural way of extending the concept of derivation matrix to higher space-time dimensions, which consists in the use of the tensor or Kronecker product. The tensor product of two matrices A and B is usually denoted by $A \otimes B$ and it is defined by

$$A \otimes B = \begin{pmatrix} A_{11}B & \dots & A_{1n}B \\ \vdots & \ddots & \vdots \\ A_{m1}B & \dots & A_{mn}B \end{pmatrix}. \tag{4.1.12}$$

So if the matrices A and B are respectively $m \times n$ and $p \times q$, $A \otimes B$ is $mp \times nq$. If we want to work in a 2-dimensional grid of points resulting from having, say, m collocation points along the direction x, $\{x_0, \dots, x_{m-1}\}$ and n points along a direction y, $\{y_0, \dots, y_{n-1}\}$ the resulting 2d grid will have mn points, whereas the Kronecker product of any two differentiation matrices acting respectively on x and y will have dimension $mn \times mn$, so it seems natural to take the mn-dimensional vector $\{x_0 y_0, \dots, x_{m-1} y_{n-1}\}$ and let the differentiation matrices resulting from the Kronecker products act upon it. Let us take D and Δ to be the 1d differentiation matrices for x and y. If one thinks about how this works in terms of matrix products, one sees, for example, that

$$\begin{aligned} \partial_x^2 &\longrightarrow I_m \otimes D_n^2 \\ \partial_x^2 + \partial_y^2 &\longrightarrow I_m \otimes D_n^2 + \Delta_m^2 \otimes I_n \end{aligned}$$

are the right equivalences between symbolic operations and numerical ones.
Again, this whole machinery is built-in in most mathematical software at use

[2] Think for example of quantities of interest involving the coefficients of the asymptotic expansion of fields, such as conductivities in an AdS/CFT context. More shall be said about such a situation at due time.

and in particular in Mathematica. In a straightforward extension of the 1-dimensional case, the 2-dimensional grid of Chebyshev points may be defined as

```
ChebPoints[z0_,L_,n_Integer/;n>1]:=x0+L/2 (1-Cos[Pi Range[0,n-1]/(n-1)]);
gridz = ChebPoints[x_0, Lx, Npointsx]//N;
gridy = ChebPoints[y_0, Ly, Npointsy]//N;
```

and the corresponding derivative of a discretised function with respect to the coordinate discretised in `gridz` can be computed by means of the differentiation matrix defined as

```
 d[1,0] = NDSolve`FiniteDifferenceDerivative[{1,0},{gridz,gridy},
"DifferenceOrder" -> {"Pseudospectral","Pseudospectral"},
PeriodicInterpolation -> {False,False}]
```

And analogously for the rest of the cases. So for example the numerical version of the cross derivative of a discretised field `Phi`, $\partial_x \partial_y \Phi$ (note that `Phi` is now a 2-dimensional matrix) is given by

```
d[1,1] = NDSolve`FiniteDifferenceDerivative[{1,1},{gridz,gridy},
"DifferenceOrder" -> {"Pseudospectral","Pseudospectral"},
PeriodicInterpolation -> {False,False}]

d[1,1][Phi]
```

So by now it is clear how to translate analytical equations into a numerical problems via differentiation matrices. The next step is the resolution of the equations at hand, which are very often non-linear equations.

4.2 Non-linearity

Once we are equipped with the mathematical gear presented in the previous section, it is time to put it work to do what is meant to do, namely solve difficult PDEs for us. Using the differentiation matrices presented above, all derivatives in our equations will be dealt with as matrices. As a consequence of that, in the case of equations linear in the derivatives, once these have been replaced by the corresponding matrices, their numerical resolution is a matter of employing a good linear system solver. But in general the equations of interest, and notably the ones this thesis copes with, will be complicated and non-linear. Non-linearity is not much of a problem though. Indeed one of the advantages of spectral methods is the ease with which non-linear equations can be solved. Still, the resolution of a linear system will not suffice to find a solution to non-linear equations and iterative methods have to be employed. Probably the most established resolution method for non-linear systems of equations is the Newton-Raphson method, the multidimensional version of the well-known Newton method for finding roots of equations in 1d. This method provides very efficient means of convergence to the sought roots provided the selected seed, or initial guess, is sufficiently good. The issue of the selection of a proper seed is a crucial one and we shall say more about it later.

The basic working principle of the Newton method is a mere Taylor expansion. A typical problem involves N_e equations whose zeroes are to be found, depending on N_e variables:

$$F_i(x_1, \ldots, x_N) = 0, \qquad i = 1, \ldots, N_e. \tag{4.2.1}$$

If we denote by $\vec{F}$ the vector of equations F_i and by $\vec{x}$ the vector of variables x_i, in the vicinity of a given value of $\vec{x}$, the last equation may be Taylor expanded as

$$\vec{F}(\vec{x} + \vec{\delta}x) = \vec{F}(x) + J \cdot \delta\vec{x} + \mathcal{O}(\delta x^2), \tag{4.2.2}$$

where J is the Jacobian matrix of partial derivatives

$$J_{ij} \equiv \frac{\partial F_i}{\partial x_j}. \tag{4.2.3}$$

Now by neglecting terms of order $\delta\vec{x}^2$ and higher and requiring that $F(\vec{x}+\delta\vec{x})$ be zero, a set of linear equations is obtained which can be solved for the corrections $\vec{\delta}x$

$$J \cdot \delta\vec{x} = -\vec{F}. \tag{4.2.4}$$

That is, the set of $\delta\vec{x}$ obtained is such that the solution is closer to the simultaneous zeroes of the equations than before. Hence $\vec{x} + \delta\vec{x}$ may be taken to be the new $\vec{x}$ and the procedure can be carried out again and again until the process converges up to the desired precision.
The Jacobian matrix might be difficult to obtain analytically though. Indeed, this is often the case in holographic computations. Still, it can be computed by finite differences.

All this can be implemented in Mathematica and connected to all of the above quite straightforwardly. For example for the case of two equations for two fields and a grid of N points, using `EOMs` for F_i (F_1 and F_2 joint together on computational purposes), `Field1` and `Field2` for the two fields present in the equations of motion, `accur` and `accurwish` for the attained and the desired accuracy respectively, `Jacob` for the finite differences approximation to the Jacobian matrix, `trialsize` for a constant quantity to account for an arbitrary trial $\delta\vec{x}$ and `deltax` to stand for the computed improved value of $\vec{\delta}x$, a `While` loop as simple as

```
Field1=seed1;
Field2=seed2;
Fields = Join[Field1, Field2];
While[accur > accurwish,
 M1 = EOMs[Field1, Field2];
 Jacob = {};
 For[m = 1, m < 2 Nx, m++;
  Fields[[m]] = Fields[[m]] + trialsize;
  Field1 = Take[Field1, {1, N}];
  Field2 = Take[Field2, {N + 1, 2 N}];
  M2 = EOMs[Field1, Field2];
```

```
 Jacob = Join[Jacob, {(M2 - M1)/trialsize}];
 Fields[[m]] = Fields[[m]] - trialsize;];
deltax = LinearSolve[Transpose[Jacob], -Flatten[M1]];
Fields = Fields + deltax;
Field1 = Take[Field1, {1, Nx}];
Field2 = Take[Field2, {Nx + 1, 2 Nx}];
accur = Max[Abs[deltax]];
]
```

will do the job. This is actually the basic structure we shall be using in our more involved codes.

4.3 Boundary value problems

The next thing to worry about is the implementation of boundary conditions to our numerical solving of equations. Boundary conditions usually play an important part when it comes to solve PDEs in physics and AdS/CFT is indeed quite a good example. In holographic models, the physical parameters one wishes to control are almost always defined in the context of boundary asymptotic expansions, for they refer to field theory quantities. Furthermore, physical requirements like the ones derived by the presence of a black hole also impose conditions upon the boundary values of the physical fields at hand. So when implementing numerics to solve equations of motion one normally has to take those physically meaningful boundary conditions into account and look for solutions which are subject to them.

Even though it is not the only possible way of implementing boundary conditions in spectral collocation methods, we will restrict to the method based on the enforcement of the boundary conditions by requiring the fulfilment of additional equations. This is both because this method turns out to be more effective when it comes to implementing different kinds of boundary conditions and because it is the method we use in our codes.
As we have seen in the previous section, the use of numerical methods relies on the fact that each derivative be replaced by the corresponding differentiation matrix. An equation of motion will be a combination of coefficients, known functions and derivatives, which then result in a resulting numerical matrix that acts upon the object containing the numerical values of the grid points in the linear system to be solved. For example, if one of the equations to be solved is Poisson's equation

$$\partial_x^2 f(x,y) + \partial_y^2 f(x,y) = g(x,y), \tag{4.3.1}$$

and we are working with a 2-dimensional grid with $N_x \times N_y$ collocation points, this will be translated into our Mathematica numerical language as

```
EOM=D[f[x,y],{x,2}]+EOM=D[f[x,y],{y,2}]-g[x,y];
EOMnumeric =
 Compile[{{fnumeric, _Real, {Nx,Ny}}},
  EOM /. {D[f[x,y],{x,2}] -> d[2,0][fnumeric],
    D[f[x,y],{y,2}] -> d[0,2][fnumeric],g[x,y] -> gnumeric}];
```

with the derivatives and the grids defined as at the end of section 4.1.
Let us assume that our grid of collocation points is the one resulting from the Kronecker product of the one-dimensional grids of Chebyshev points for x, ranging from $-L_x$ to L_x and for y, ranging from $-L_y$ to L_y. Taking into account the rules of matrix algebra it is possible to identify which matrix elements affect which of the grid points. For instance, it is clear that in the previous example, the numerical matrix produced by `EOMnumeric[fnumeric]` is a $N_x \times N_y$, whose first row controls what happens in the x-slice where x takes the first value of the corresponding grid, $x = -L_x$, for the different values of the grid for y from $-L_y$ to L_y. Analogously, the last column of the matrix dictates what is being imposed along the y-slice where $y = L_y$ is fixed at the last value of its collocation points.
The boundary conditions we will most often have to deal with must be imposed at the edges of the intervals. In the case of algebraic conditions, like Neumann boundary conditions for example, we will impose the corresponding equations at the right position. In the case of Dirichlet boundary conditions it is easier to set the value of the numerical variable to the desired one at the beginning and keep it fixed during the resolution process. So if we want to solve again Poisson's equation but this time subject to the boundary conditions

$$\begin{aligned} &f(x = -L_x, y) = 2 \qquad && \partial_x f(x = L_x, y) = 3f(x = L_x, y) \\ &\partial_y f(x, y = -L_y) = 0 && \partial_y f(x, y = L_y) = 0 \end{aligned} \tag{4.3.2}$$

we do it by as described by means of

```
fnumeric=Join[Table[2.,{i,1,Ny}],seedrest]
EOMwithBCs =
 Compile[{{fnumeric, _Real, {Nx,Ny}}},
  Join[Transpose[
    Join[{Take[Transpose[d[0, 1][fnumeric]][[1]], {2, Nx - 1}]},
     Transpose[
      Take[EOMnumeric[fnumeric], {2, Nx - 1}, {2,Ny - 1}]],
      {Take[Transpose[d[0, 1][fnumeric]][[-1]], {2, Nx - 1}]}]],
       {d1[1, 0][fnumeric][[-1]] - 3 fnumeric[[-1]]},
   ]]
```

Where our previously defined function `EOMnumeric` is taken at the inner grid points whereas the boundary conditions 4.3.2 are incorporated at the outer rows and columns according to their position. Furthermore, note that no row is included to impose the Dirichlet boundary condition. Instead, the numerical value of the variable `fnumeric` is taken in the seed such that the condition is respected from the very beginning and the first row, corresponding to the position $x = -L_x$ should be omitted in the Newton-Raphson routine. The resulting disposition of the resulting numerical matrix operator is schematically

where the grid of points (x, y) is assumed to be arranged with x varying in the vertical direction and y varying horizontally.

As mentioned before, most times our boundary conditions will be physical ones. Good examples in holography are the preservation of causality at black

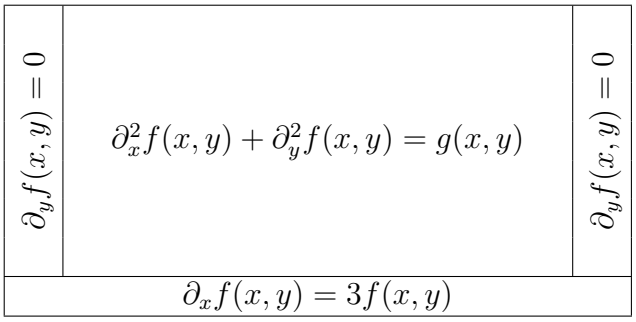

hole horizons, which requires that no information propagate in time from inside the black hole outwards or the imposing of constraint equations. The former must be fulfilled at the black hole horizon itself whereas the latter might usually be imposed either at the black hole horizon or at the AdS boundary. As to the spatial boundaries in holographic examples where a boundary direction is also considered - as it will here - different possibilities exist, being more or less convenient depending on the geometry of the problem. Explicit examples will be given in chapters 5 and 6.

4.4 Taking profit of symmetry

Sometimes it is useful to take profit of the particular symmetry of a physical problem to save up computation resources and time. When dealing for example with a periodic system, different mathematical techniques to the ones presented above can be employed, which are more efficient. Another possibility is that the symmetry present in the system makes it unnecessary to solve for the entire range, for a part of this might be deduced from the remaining, as is the case of parity. We shall now explore such cases and its peculiarities, as they are of interest to our work.

4.4.1 Parity

Parity is the simplest kind of symmetry a physical system may display. We talk about parity whenever the functions present in the model can be grouped in even and odd functions, according to whether they are symmetric or antisymmetric.
A function $f(x)$ is said to be *even* or *symmetric* if it verifies

$$f(x) = f(-x), \tag{4.4.1}$$

whereas it is called *odd* or *antisymmetric* if it satisfies

$$f(x) = -f(-x). \tag{4.4.2}$$

The direct practical consequence of having functions with a definite parity is that knowing them in one half of the considered interval suffices to know

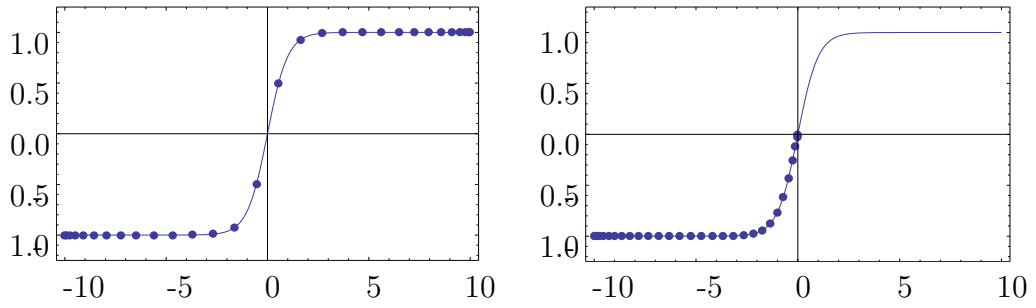

Figure 4.3: Comparison of the resolution obtained by a grid of $N = 30$ Chebyshev points for the function $\tanh x$ when the grid covers the interval {-10,10} (left) and when symmetry is exploited to concentrate the grid points in one half of the interval, namely to {-10,0} (right). Note how the density of points close to the symmetry point is bigger in the latter case. Gradients are bigger there than elsewhere, so this extra resolution is more than welcome.

their behaviour entirely. This allows furthermore either to work with half the number of collocation points or to achieve a better precision with a given number of them.
Of course splitting the domain of numerical resolution introduces the need for extra boundary conditions at the point at which the grid is split, in this case at $x = 0$ in this case. Nevertheless, differentiating a function with a definite parity an odd number of times reverses the parity whereas doing it an even number of times leaves it unchanged and this can be used to set the new boundary conditions for the functions and their derivatives. This means that an even function satisfies

$$\partial_x f(x)|_{x=0} = 0, \tag{4.4.3}$$

whereas an odd function verifies

$$f(x)|_{x=0} = 0. \tag{4.4.4}$$

Both conditions can be imposed at $x = 0$ when splitting the interval there as explained above.

A further positive effect of symmetry allowing to halve the interval along which the collocation points are placed is that more resolution is gained around the point with respect to which functions have a definite parity. This is so because of the spatial arrangement of Chebyshev points, which concentrate at the edges of the range. The situation is illustrated in figure 4.3. In general, physical situations displaying this kind of symmetry will be related to localised defects such as point-like impurities or interfaces. It is by all means good news to have more precision close to that exceptional locations, where mathematical functions will generally behave in a different way than far from them.

4.4.2 Periodicity

Another kind of symmetry which helps simplifying things substantially is periodicity. This is so on computational grounds due to the possibility of invoking the convenient properties of the Fourier transform if the functions involved are periodic. It is well known that any periodic function may be expanded as a Fourier series, which helps when it comes to interpolate. Furthermore, the implementation of the well-known Fast Fourier Transform, an algorithm to compute discrete Fourier transforms, provides a remarkable enhancement in computation speed[3].
The Fourier transform enters our game via its close connection to Chebyshev polynomials, based on a relationship between any grid of Chebyshev points and an equivalent periodic grid of evenly spaced points. Once such a grid is available, the great computational power of the FFT can be exploited.

To see the close connection mentioned above, it suffices to recall equation 4.1.7 and see that our set of Chebyshev points is defined from the set of evenly spaced points

$$\theta_j = \frac{j\pi}{N} \qquad j = 0, 1, \ldots, N, \tag{4.4.5}$$

and hence straightforwardly related to it. This suggest that when dealing with periodicity it might be more convenient not to work with the grid of Chebyshev points and the differentiation matrices shown above but rather to turn to the corresponding grid of evenly distributed points 4.4.5 and then use trigonometric functions as interpolants. For more mathematical detail on the equivalence of both procedures the reader is referred to [81].

The implementation in Mathematica that takes profit from periodicity is very easy to realize as a deviation from our previous codes. It just requires the definition of a grid of evenly distributed points instead of one of Chebyshev points.

```
gridz = Range[x_0, x_0 + Lx, Lx/(Npointsx - 1)] // N;
gridy = ChebPoints[y_0, Ly, Npointsy]//N;
```

and the specification of periodicity in the definition of the differentiation matrices, like for example

```
d[1,1] = NDSolve`FiniteDifferenceDerivative[{1,1},{gridz,gridy},
"DifferenceOrder" -> {"Pseudospectral","Pseudospectral"},
PeriodicInterpolation -> {True,False}]

d[1,1][Phi]
```

It is no problem at all combining such a grid in one dimension with one of Chebyshev points in another dimension. Indeed this combination is quite an interesting possibility in holography, given that no periodicity can be assumed

[3]For more information about the FFT, see for example [82]. Since we do not use it directly here but just use Mathematica built-in functions based on its use, we do not get into details about it.

in the AdS radial direction. Of course periodicity also eliminates the need to fix boundary conditions at the spatial edges. A further advantage is the possibility of ignoring the numerical values corresponding to the first or the last point of the periodic coordinate, since they are equal to the last or the first point values due to periodicity.

Once the required tools have been presented, we are now well prepared to present and analyse the more involved codes we use for our codes.

4.5 Numerical PDE solving in AdS/CFT

In the light of all of the above, we are now in a good position to start employing the skills we have collected this far for holographic purposes. Along well-known time-saving techniques common to all numerically-oriented codes there are some tricks specific to Mathematica which are worth taking notice of. An example of the former is the storing of numerical data which is used repeatedly to avoid its computation over and over. It is a very simple idea that may save lots of time. So for example if our radial coordinate, z, is discretised in the variable `gridz`, we might as well assign names to the quantities $z^2, z^3, \ldots$ and save them so that Mathematica does not have to multiply the vector `gridz` by itself each time it appears but rather substitutes the variable by its pre-stored numerical value.
As an instance of a practical detail specific to Mathematica, it is good pointing out the convenience of using the built-in *Compile* function wherever possible to perform numerical computations, for it speeds up the code drastically[4]. This is why we have been including this function in our listings this far. So for example, once it comes to turn the analytical form of the equations of motion, say `EOMa` and `EOMb` into numerical values, we shall turn to such an object

```
EOMa_num = Compile[{{{ChiNum, _Real, {Nx, Nyh}}}, {{A0Num, _Real, {Nx, Nyh}}}},
   EOMa /. numvalues];
```

where the substitution rule introduces the corresponding numerical values for the analytical variables

```
numvalues= {D[Chi[z, x], {x, 2}] -> d[0, 2][ChiNum],
D[Chi[z, x], {z, 2}] -> d[2, 0][ChiNum],
D[Chi[z, x], {z, 2}] -> d[2, 0][ChiNum],
D[Chi[z, x], {z, 1}] -> d[1, 0][ChiNum],
D[Chi[z, x], {x, 1}] -> d[0, 1][ChiNum],
D[Chi[z, x], {z, 1}, {x, 1}] -> d[1, 1][ChiNum], Chi[z, x] ->
 ChiNum, D[A0[z, x], {x, 2}] -> d[0, 2][A0Num],
D[A0[z, x], {z, 2}] -> d[2, 0][A0Num],
D[A0[z, x], {z, 2}] -> d[2, 0][A0Num],
D[A0[z, x], {z, 1}] -> d[1, 0][A0Num],
D[A0[z, x], {x, 1}] -> d[0, 1][A0Num],
D[A0[z, x], {z, 1}, {x, 1}] -> d[1, 1][A0Num], A0[z, x] -> A0Num,
h[z] -> hnum, h'[z] -> hnumdr, h''[z] -> hnumdr2, f[z] -> fnum,
f'[z] -> fnumdr, f''[z] -> fnumdr2, z^2 -> gridz2, z^3 -> gridz3,
```

[4] See https://reference.wolfram.com/language/Compile/tutorial/Introduction.html#8903121 for detailed information

```
z^4 -> gridz4, z^5 -> gridz5, z^6 -> gridz6, z^7 -> gridz7,
z^8 -> gridz8, z^9 -> gridz9, z^10 -> gridz10, z^11 -> gridz11,
z^12 -> gridz12, z^13 -> gridz13, z -> gridz, x -> gridy};
```

Where the fields χ and ϕ are analytically represented in Mathematica by `Chi[z,x]` and `A0[z,x]` respectively, whereas their numerical values are stored as `ChiNum` and `A0Num` respectively.
A further relevant issue is that of the choice of a proper seed or initial guess for our numerical resolution methods, like the Newton-Raphson iteration, to converge. We make use of two different approaches to this matter. One of them consists in first solving the easier homogeneous problem, in which nothing depends on the spatial coordinate x and taking the homogeneous solution as a starting point for the non-homogeneous one. This method is specially well-suited for configurations with deviations from an average value like noises, whence we shall employ it in chapter 6.
Our second approach is based on the use of smaller grids of collocation points at the beginning whose solution is then extrapolated to a bigger grid to continue with the proper calculation. Small grids of 15×15 collocation points usually provide with a good starting base. We will make use of this method in the computation in chapter 5.

It is furthermore very recommendable to perform as many numerical tests as possible to make sure that things are working properly. One clear example is the monitoring of the propagation of the constraint equation when it is set to zero at one of the boundaries of the numerical domain. If things are in good order, the numerical value of the constraint should not get bigger to numerical accuracy than the values of the equations of motion that are being explicitly imposed.
Further possible checks include the comparison of the numerical results in the non-homogeneous case to the ones obtained when solving the homogeneous problem. Note that using the homogeneous problem as an easier way to estimate values and behaviours is mostly a clever thing to do.

All in all, our codes will not be much than a combination of the techniques we have reviewed in this chapter. Detailed commented version of the real codes are offered in appendix D. It should be taken into account though, that our codes have been written by a physicist and are very far from being optimal. For sure there is great room for improvement and optimisation, though our lack of these compensates with simplicity and makes the codes more accessible to the dummy user.

4.6 Final remarks

The main motivation of our use of numerical methods is our necessity to attack problems in which translation invariance is broken. Thereby we reckon some

words on the current state of research along this line in an holographic context would not go amiss.
Recently, significant progress has been achieved in studying holographic systems with broken translation invariance by numerically solving the resulting equations of motion, which are in general partial differential equations. These include set-ups with different holographic realisations of lattices [83, 84, 85, 86, 87, 41, 88, 89] through periodically space-dependent sources, and also set-ups implementing disordered sources [27, 28, 30, 90]. Moreover, a lattice realisation where PDEs are avoided, which goes under the name of Q-lattices given its resemblance to the construction of Q-balls [91], was introduced in [92] and further explored in [93, 94]. Alternatively to introducing translational symmetry breaking by spatially modulating the sources of conserved currents, momentum relaxation may also be realised by explicitly breaking diffeomorphism invariance in the bulk [95, 96, 97, 98, 99, 100, 101], which in [102] led to progress on the study of the conductivity for systems with broken translational symmetry.

Part II

Holographic strongly coupled fundamental matter with inhomogeneities

Chapter 5

Holographic charge localisation at brane intersections

In chapter 3 we laid down the principles of AdS/CFT duality and the prescription to exploit its power. In chapter 4 we introduced the necessary machinery to perform numerical computations involving partial differential equations in an holographic context. It is now time to combine both pieces of knowledge to investigate interesting phenomena in strongly coupled matter.

In all of the above we only considered fields depending on the radial coordinate of AdS, which implies the assumption of translation invariance in all other directions. Nevertheless, a number of relevant phenomena in condensed matter physics do not display this translation invariance. For example, those which involve the presence of an interface between materials of different kind. Such interfaces represent a localised impurity which breaks translational symmetry in the system. Broken translational symmetry allows the charge carriers to dissipate their momentum. In the case of strong coupling, where the standard quasiparticle picture does not apply, many questions about the exact form of this mechanism are still open. Gauge/gravity duality reveals itself as a natural tool to further explore momentum dissipation at strong coupling, given that it provides a method for describing strongly coupled systems by mapping them to weakly coupled gravity theories as we showed above.

It is this step of introducing translational symmetry breaking which requires the fields to depend not just on the radial AdS coordinate but at least on an additional spatial coordinate, we shall call x. When doing so, the resulting equations of motion are in general partial differential equations, which we know now how to handle.

In this chapter, based on the author's publication [43], we consider the breaking of translation invariance by an interface. We consider a top-down model involving a D5 probe brane with a kink geometry. The basic idea is to in-

corporate the existence of massless fundamental matter modes localised on an interface by letting the embedding of the flavour probe brane vary over the distinguished boundary coordinate x, in addition to being a function of the radial coordinate. This way, the corresponding dual gauge theory physical quantities also display spatial dependence, whose effects we wish to study. This is implemented by an embedding function that asymptotes to a positive value m (with $m_q = 2\pi\alpha' m$ the quark mass, see (3.4.41)) for $x \to \infty$ and to $-m$ for $x \to -\infty$, while it vanishes at $x = 0$, therefore introducing a defect surface there. The original idea was introduced in [25] to design a holographic model for topological insulators using the D7/D3 intersection and further explored in [24].

5.1 Holographic set-up

We consider a D3/D5 intersection, that is a probe D5 flavour brane in the background geometry generated by the stack of D3 black branes (3.4.33)

$$ds^2 = \frac{L^2}{z^2}\left(-\frac{f(z)^2}{h(z)}\,dt^2 + h(z)\,d\vec{x}^2 + dz^2\right) + L^2\,d\Omega_5^2\,, \tag{5.1.1}$$

We do it in the presence of temperature and chemical potential for the fundamental matter dual to the open strings stretching between the flavour brane and the D3-branes. We work in the probe limit approximation presented in subsection 3.4.2, hence using a DBI action like (3.4.31):

$$S = -N_f T_{D5}\int d^6\xi\,\sqrt{-\det(P[g] + 2\pi\,\alpha'\,F)}\,, \tag{5.1.2}$$

and embedding the D5 probe brane according to (3.4.38)

	t	x_1	x_2	x_3	z	Ω_2	$\tilde{\Omega}_2$	θ
D3	×	×	×	×				
D5	×	×	×		×	×		

(5.1.3)

We use the χ defined in (3.4.39) to describe the embedding and introduce a non-zero temporal component of the $U(1)$ gauge field on the world-volume of the probe brane, A_t, (3.4.42), whose dimensionless version ϕ we defined in (3.4.43). However, since we now wish to introduce a spatial dependence, we let the fields χ and ϕ that specify the embedding depend not only on the radial coordinate of AdS but also on the distinguished spatial coordinate x

$$\chi = \chi(z, x) \qquad \phi = \phi(z, x). \tag{5.1.4}$$

With this set-up, reminding ourselves of the fact that we need not include a Chern-Simons term, the DBI action can be written as

$$S = -N_f\,T_{D5}\,L^6\int dt\,d^2x\,dz\,d\Omega_2\,f\,z^{-4}\,\sqrt{h\,(1-\chi^2)\,(S_\chi + S_\phi + S_{\rm int})}\,, \tag{5.1.5}$$

with

$$S_\chi = 1 - \chi^2 + z^2\chi'^2 + \frac{z^2\,\dot{\chi}^2}{h}\,, \tag{5.1.6}$$

$$S_\phi = -\frac{z^4(1-\chi^2)}{f^2}\left(h\,\phi'^2 + \dot{\phi}^2\right)\,, \tag{5.1.7}$$

$$S_{\rm int} = -\frac{z^6(\dot{\chi}\phi' - \chi'\dot{\phi})^2}{f^2}\,, \tag{5.1.8}$$

where a tilde denotes a derivative with respect to z and a dot a derivative with respect to x. The equations of motion for $\phi(z,x)$ and $\chi(z,x)$ can be readily obtained from the action (5.1.5). They are shown in appendix B.
Once they are known we can proceed to analyse their near-horizon ($z \to 1$) and near-boundary ($z \to 0$) asymptotic behaviours by expanding the corresponding limits of the equations of motion.

IR Asymptotics

As we saw in subsubsection 3.4.2, we are interested in solutions describing black hole embeddings for which the brane ends at the horizon. Hence regularity at the horizon requires ϕ to vanish there. The geometry furthermore requires that χ' also vanish there, restricting the infra-red solution to the following form

$$\phi(z,x) = a^{(2)}(x)\,(1-z)^2 + \mathcal{O}((1-z)^3)\,, \tag{5.1.9a}$$

$$\chi(z,x) = C^{(0)}(x) + C^{(2)}(x)\,(1-z)^2 + \mathcal{O}((1-z)^3)\,, \tag{5.1.9b}$$

with

$$C^{(2)}(x) = \frac{\left(2 - a^{(2)}(x)^2\right)\left[C^{(0)\prime\prime}(x)(C^{(0)}(x)^2 - 1) - C^{(0)}(x)\left(3C^{(0)\prime}(x)^2 + 4\right) + 4C^{(0)}(x)^3\right]}{8\left[C^{(0)\prime}(x)^2 - 2C^{(0)}(x)^2 + 2\right]}\,. \tag{5.1.10}$$

UV Asymptotics

At the boundary, the asymptotic form of the fields $\chi(z,x)$ and $A(z,x)$ is of the same form as in (3.4.40) and (3.4.44) but taking now the x-dependence of the fields into account

$$\phi(z,x) = \mu(x) - \rho(x)z + \mathcal{O}(z^2)\,, \tag{5.1.11a}$$

$$\chi(z,x) = m(x)\,z + \psi(x)z^2 + \mathcal{O}(z^3)\,. \tag{5.1.11b}$$

Let us recall that the holographic dictionary relates $\mu(x)$, and $\rho(x)$ respectively to the chemical potential and charge density of the $U(1)$ flavour symmetry supported by the D5-brane. As for the asymptotic form of χ, the leading piece $m(x)$ is proportional to the asymptotic distance $\bar{M}$ between the probe D5 and the D3-branes generating the background, and is therefore interpreted as the

quark mass.

As is clear from (5.1.11), the UV solutions depend on four parameters (functions of x): μ, ρ, m, and ψ, while as we see in (5.1.9),the IR behaviour is determined by two free functions, namely $C^{(0)}(x)$ and $a^{(2)}(x)$. Thus we expect a two-parameter family of solutions, which we choose to describe in terms of the chemical potential μ, which we assume to be independent of x, and the mass $m(x)$. Consequently, once μ and $m(x)$ are fixed, the embedding of the probe D5-brane is completely fixed.

5.1.1 Inhomogeneous embeddings and charge localisation

As we saw in subsection 3.4.2, at non-zero charge density only embeddings of the black hole type are possible in the Dp/Dq model. As explained in [67], the fundamental strings realizing the charge density would have nowhere to end in a Minkowski embedding. Moreover, as illustrated in figure 3.6, for a large enough M_q/T, black hole embeddings exist only above a non-zero chemical potential $\bar{\mu}/T$. In particular, the shaded region in the plot is only accessible by Minkowski embeddings, which have zero charge density.
Our purpose is to construct an embedding depending on one spatial direction x, that localises charge density along an interface situated at $x = 0$. This can be done following [25] by means of an embedding with constant chemical potential $\mu = \bar{\mu}/T$ and an x-dependent mass ($m = M_q/T$)

$$m(x) = M\left(\frac{2}{1+e^{-a\,x}} - 1\right), \tag{5.1.12}$$

that interpolates between two constant values; M at $x = -L$, and $-M$ at $x = L$, while vanishing at the origin, $m(0) = 0$.[1] a is a constant parameter that fixes the steepness of the kink. If we were to choose μ and M to lie within the shaded region of figure 3.6, asymptotically, at $x \to \pm L$, the embedding would be of the Minkowski type and the charge density would vanish there. At the interface ($x = 0$) though, the mass would vanish, the brane would intersect the black hole and, for a non-zero μ, some charge density would be induced. In such a construction the charge density would exactly vanish towards the spatial edges while it would peak at the interface. Notice that by increasing a in (5.1.12) the transition can be made as abrupt as desired, and therefore the charge may be localised around $x = 0$. However, such an embedding, with a varying topology along x, turns out to be too challenging in numerical

[1] As explained in [26], embeddings with positive and negative m correspond respectively to the D5-brane sitting at opposite poles of the $\tilde{\Omega}_2$ in (3.4.38). We take L to be the spatial boundary, which may also be $L = \infty$. More shall be said on this further down. As in [25] we account for the case $m < 0$ by letting χ become negative.

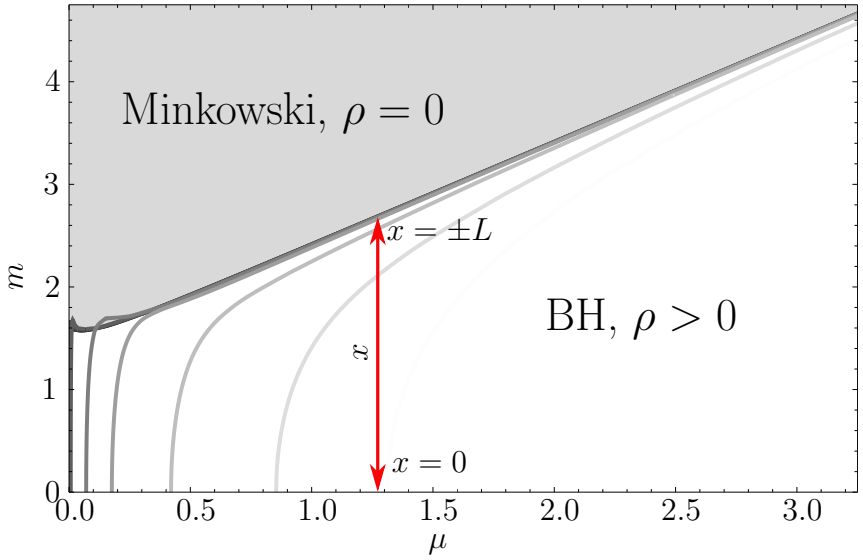

Figure 5.1: Illustration of the step-like construction of equation(5.1.12) upon the phase diagram of the D3/D5 probe system previously presented in figure 3.6. The embedding interpolates between a massless embedding at $x = 0$ and a massive one at $x = L$ very close to the transition to the Minkowski embeddings, for which the charge density is zero. While some charge will be induced at the spatial edges, given that for numerical reasons we stay within the black hole region of the phase diagram, the charge will be peaked at $x = 0$ and become small at the spatial edges whenever the value of M and μ there are such that the embedding is close to the Minkowski regime. As a result of this, we expect charge density to be localised around $x = 0$ in such a configuration.

terms. Instead, we do as in [24], and go for a more modest construction: we choose M and μ to be just outside, but at the edge of, the shaded region of figure 3.6. This way we deal with embeddings that are of the black hole kind everywhere. Notice that in principle one can pick M and μ such that the corresponding embedding has an arbitrarily small charge density induced at the edges. Then, the charge density is effectively localised around the interface, where the embedding becomes massless. The kind of construction we use is illustrated in figure 5.1.
We plot the same data in figure 5.2 but represent it as μ/M versus $1/m$ to make more explicit the presence of the forbidden region, which can be seen for values $1/m \lesssim 0.6$.

5.2 Numerical machinery

With the equations of motion for our system - (B.0.1) and (B.0.2) - at hand, the next natural step is the application of the numerical techniques presented in chapter 4 to solve them. The inhomogeneous mass profile boundary condition

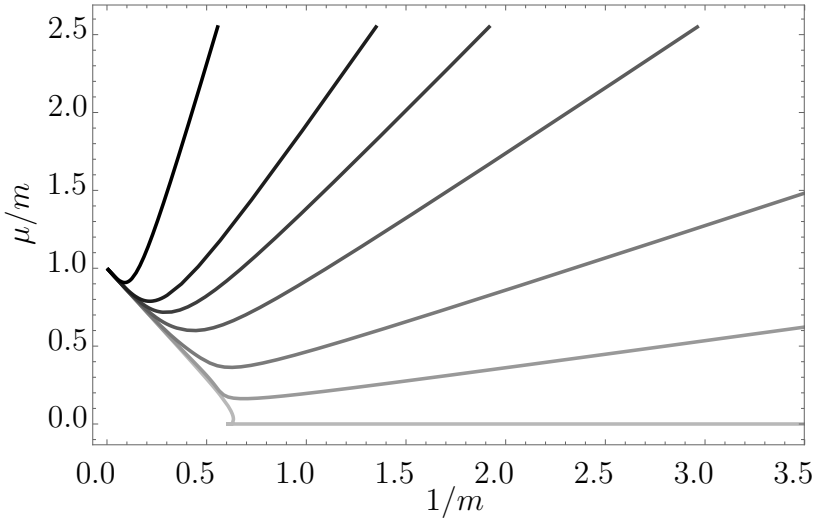

Figure 5.2: As in fig. 3.6 we plot lines of constant charge density for black hole embeddings. From bottom (light grey) to top (black) they correspond to $\rho = 10^{-6}, 0.25, 0.6, 1.25, 2, 3, 10$.

(5.1.12) implies that we have to deal with two coupled second order partial differential equations. The role played by the boundary conditions turns out to be crucial, since it is through them that we set the values of m and μ and hence the kind of embedding we have.
At the boundary, from (5.1.11) and (5.1.12), we must impose

$$\chi'(0,x) = M\left(\frac{2}{1+e^{-ax}} - 1\right), \qquad \phi(0,x) = \mu\,, \tag{5.2.1}$$

where μ determines the homogeneous chemical potential of the solution, while M fixes the mass of the embedding at the edges of the system. On the other hand, at the horizon, $z = 1$, the asymptotic solutions (5.1.9) and the requirement of regularity in the sense elucidated in (3.4.45) result in the following boundary conditions

$$\phi(1,x) = 0\,, \qquad \chi'(1,x) = 0\,. \tag{5.2.2}$$

As for the boundary conditions at the spatial edges, given that the symmetry of our set-up with a step-like configuration does not allow the use of periodic boundary conditions as is commonly done, we take our system to have a finite length ($x \in [-L, L]$), but require it to be large enough so that it resembles an homogeneous embedding towards the spatial edges. Consequently we impose the following Neumann boundary conditions

$$\dot{\chi}(z,\pm L) = 0\,, \qquad \dot{\phi}(z,\pm L) = 0\,, \tag{5.2.3}$$

which ensure that the effects of the inhomogeneity sourced by the mass profile (5.1.12) fade away towards the spatial edges.

We obtain our numerical solutions using the pseudospectral methods of resolution shown in chapter 4. We use Mathematica to discretise the plane (z, x) on a grid of Chebyshev points and then solve the resulting set of non-linear algebraic equations via Newton-Raphson iteration. Defining the variations of the fields $f = (\chi, \phi)$ in each iteration as δf, we consider the accuracy of our solution to be given by Max $|\delta f|$. We work to an accuracy defined this way of 10^{-12}.
In addition, we can benefit from the symmetry of our set-up by noting that $\chi(z, x)$ is an odd function of x, whereas $\phi(z, x)$ is even

$$\chi(z, x) = -\chi(z, -x)\,, \qquad \phi(z, x) = \phi(z, -x). \tag{5.2.4}$$

This follows from the form of the equations of motion together with our UV boundary conditions (5.2.1) and helps us making the numerics more efficient in two ways. First, it allows us to solve for half the range along x, imposing (5.2.3) at $x = L$, while in view of 5.2.4 at $x = 0$ we must have

$$\chi(z, 0) = 0\,, \qquad \dot{\phi}(z, 0) = 0. \tag{5.2.5}$$

Second, given that Chebyshev collocation points are more densely concentrated towards the boundaries of the interval, this reduction of the integration range results in a better accuracy of our solutions around the interface (at $x = 0$), where the gradients along x are bigger. This is exactly the situation we described in subsection 4.4.1 and illustrated in figure 4.3.

5.3 Background solution and charge density

We now present the results obtained using the numerical techniques of chapter 4 according to the previous section. We use a grid of 50×50 collocation points for the half-interval of integration ranging from $x = 0$ to $x = 10$. We will show plots for a solution with $\mu = 4$ and $M = 5.34$. This combination is chosen so that the charge density induced at the edges of the system is much lower than at the interface. The parameter a in (5.1.12) is chosen so that stable numerics is obtained while still having an embedding which is steep enough. $a = 3$ turns out to be good enough for this purpose[2]. The numerical solutions of the fields $\chi(z, x)$ and $\phi(z, x)$ are shown in figure 5.3. It is interesting to note how the spatial inhomogeneity introduced by the step-like boundary condition (5.1.12) affects differently the two fields defining our set-up. While for χ the inhomogeneity is amplified towards the horizon, for the gauge field ϕ it dies away towards the horizon.

[2]While the numerics allow for much bigger values of a for the computation of the background, these pose some difficulties when it comes to solving for the perturbation fields, which we will undertake later.

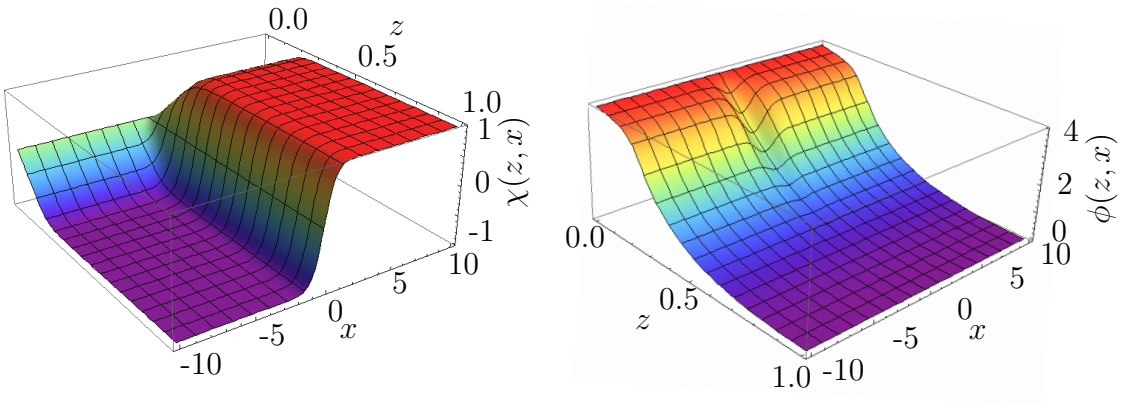

Figure 5.3: Computed solutions of $\chi(z,x)$ and $A(z,x)$ for $\mu = 4$ and $M = 5.34$.

Once we know the solution of the fields χ and ϕ, we can employ the asymptotic form of ϕ, (5.1.11) to read out the charge density ρ, which is then given by

$$\rho(x) = -\partial_z \phi|_{z=0} \tag{5.3.1}$$

In figure 5.5 we present the resulting charge density associated to the background in figure 5.3. As expected, we see that the charge density peaks at the interface, where its value is about five times the value at the edges. We also see that the base line is not zero, since we are still in a black hole embedding with induced charge density at the spatial edges. Still since, leaving numerical subtleties aside, it is possible to get arbitrarily close to the transition line to the Minkowski embeddings, this phenomenon of charge localisation can be as pronounced as one wishes. Getting the choice of parameters M and μ closer to that line would move the base line in figure 5.5 downwards, thereby increasing the ratio of the charge density peak at $x = 0$ over the baseline charge density at the spatial edges.

Moreover, it is interesting to study how the charge density depends on the chemical potential, both at the interface and far from it. This is plotted in figure 5.4. We observe that the scaling $\rho \propto \mu^2$ expected for a D3/D5 intersection [103] is approached everywhere in our system for large enough μ. This prediction is made on general grounds based on the use of the DBI action and the probe approximation for a Dq probe brane sharing $d-1$ space-like dimensions with the stack of Dp-branes generating the background geometry and it states that for large ρ the relation

$$\rho \propto \mu^{\frac{1}{4}(p-7)(p-d-2)+(p-3)(q-d)} \tag{5.3.2}$$

is fulfilled at leading order. In our case, $p = 3$, $q = 5$ and $d = 3$, so that indeed the result is

$$\rho \propto \mu^2 \tag{5.3.3}$$

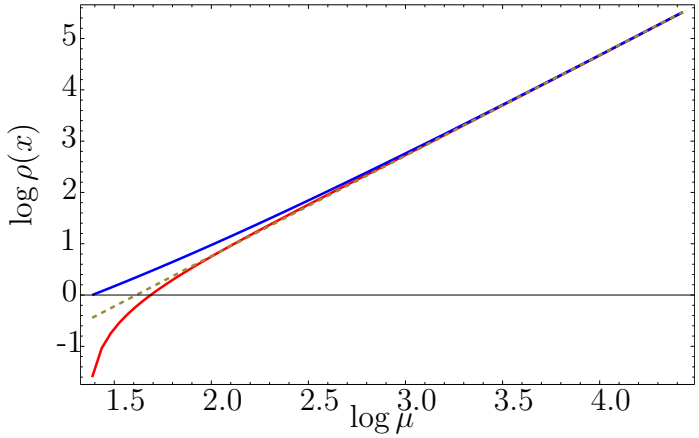

Figure 5.4: Charge density $\rho(x)$ versus chemical potential μ for an embedding with $M = 5.3$. The blue line corresponds to the interface, while the red one to one of the spatial edges. The charge density has been normalised to unity at $\mu = 1$, $m = 0$. The dashed line illustrates the fit $\rho = \mu^{1.96}$ performed for $\mu > 74$.

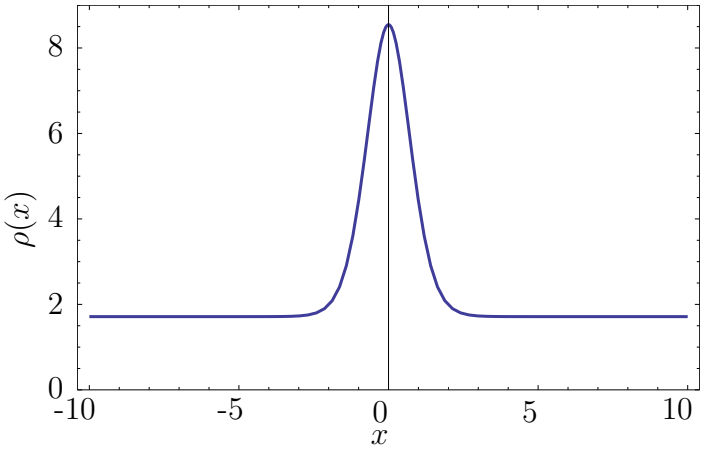

Figure 5.5: Charge density $\rho(x)$ for the background in figure 5.3. The base line is at $\rho = 1.71$, and the peak reaches $\rho = 8.54$.

as we numerically find. For the D7-brane case instead, the correct relationship would be $\rho \propto \mu^3$. The confirmation of this behaviour at the interface was seen in [24] as a piece of evidence in support of the presence of a Fermi surface there. However, since in the D5 case we observe this predicted behaviour at high μ both at the interface ($x = 0$) and away from it, we cannot agree with this line of reasoning. Still, as pointed out in that paper, looking for further signatures of the fermionic nature of the interface is an interesting research direction in this kind of systems.

5.4 Conductivities

After constructing a holographic set-up localizing charge along a (1+1)-dimensional defect, we go on to study its response to an applied electric field, namely its electrical conductivity. We do this according to what we developed in subsection 3.5.1 so as to study the conductivities of our system both in the direction parallel, y, and orthogonal to the defect, x. For reasons that will soon become apparent, we also differentiate between the so-called DC conductivity, which is the optical conductivity at zero frequency and the so-called AC conductivity, by which the conductivity at any frequency is meant.

In order to bring the required electric field into the game as in (3.5.3), we consider fluctuations around our background solution with vanishing spatial components of the gauge field ($A_x = A_y = 0$) and compute the linear response of our background when an electric field is switched on along the boundary. So as to analyse these transport properties at the interface generated by the mass profile (5.1.12) we study the fluctuations of the gauge field on the world-volume of the D5 probe brane along the spatial directions it shares with the stack of D3 branes, which we have labelled x and y. In general these fluctuations couple among them and to the fluctuations of the embedding field χ, thus we have to solve for the whole set of coupled fields.

We hence switch on fluctuations of the gauge field realizing an electric field of constant modulus and frequency ω along the boundary. That is at $z = 0$ we require the fluctuations to satisfy

$$f_{ti} = (i\omega\, \mathfrak{e}_i)\, e^{i\omega t}\,, \qquad (i = x, y)\,. \tag{5.4.1}$$

where f_{ti} stands for the field strength of the fluctuations of the gauge field, and we are considering both the case when the electric field is orthogonal and parallel to the interface. $\mathfrak{e}_x$ and $\mathfrak{e}_y$ are respectively the corresponding constant moduli. Once these fluctuations are defined, we may plug them into our expression for the conductivity (3.5.8) to obtain

$$\sigma_i(\omega, x) = \frac{j_i}{i\omega\, \mathfrak{e}_\mathfrak{i}} = \lim_{z\to 0} \frac{f_{iz}}{f_{ti}}\,, \qquad (i = x, y)\,. \tag{5.4.2}$$

Consequently, it will be necessary to analyse the following set of fluctuations[3]

$$A_\mu = A_\mu(z, x) + \epsilon\, a_\mu(z, x) e^{i\omega t}\,, \tag{5.4.3a}$$
$$\chi = \chi(z, x) + \epsilon\, c(z, x) e^{i\omega t}\,, \tag{5.4.3b}$$

where ϵ just keeps track of the fluctuation order, ϕ_μ and χ stand for the background fields, while a_μ and c refer to the fluctuations of the gauge field and the

[3]Since we are working with the dimensionless coordinates (3.4.36), ω is dimensionless, and in terms of the dimension-full frequency $\mathfrak{w}$, one has $\omega = \sqrt{2}\,\mathfrak{w}/(\pi T)$.

embedding scalar respectively. Note that the gauge field and its fluctuations are intended to be renormalised according to (3.4.43) so as to be dimensionless.
Our background, described by $A_t(z,x)$ and $\chi(z,x)$, is time invariant. This allows us to Fourier transform along the time direction, t and justifies the form of the fluctuations considered. Given that we are interested only in the conductivity, we wish not consider our fluctuations to have any net spatial momentum. In addition, we choose to work in the radial gauge and therefore set

$$a_z(z,x) = 0\,. \tag{5.4.4}$$

We are working in the linear response regime. The equations of motion for the fluctuations (5.4.3) follow from expanding the DBI lagrangian of the action (5.1.5) up to second order in those fluctuations

$$\mathcal{L} = \mathcal{L}_0 + \epsilon\,\mathcal{L}_1 + \epsilon^2\,\mathcal{L}^2 + \dots\,. \tag{5.4.5}$$

Upon imposing the equations of motion for the background fields $\mathcal{L}^1$ vanishes and the linearised equations for the fluctuations can be found from the quadratic part of the action, $\mathcal{L}^2$, which is shown explicitly in appendix C. Although straightforward to derive from it, the resulting equations of motion are lengthy and we do not reproduce them here.

However, it is worth mentioning that the component of the gauge field fluctuations parallel to the defect, a_y, decouples from the rest of the fluctuations. Hence to study the conductivity σ_y we only need to solve the corresponding linear partial differential equation (PDE) for a_y. Instead, a_x is coupled to both a_t, and c. Their dynamics is described by a system of three second order linear PDEs plus a first order constraint PDE resulting from the equation of motion for a_z.

Boundary conditions at the horizon

In order to compute the conductivity, we must proceed as in section 3.5.1 and solve the equations of motion of the fluctuations with in-falling boundary conditions at the horizon (3.5.12) - (3.5.14) so as to preserve causality. Thus we assume that in the IR ($z \to 1$) the fluctuation fields take the form

$$a_\mu = (1-z)^{i\alpha_\pm}\left(a_\mu^{(0)}(x) + a_\mu^{(1)}(x)\,(1-z) + \mathcal{O}((1-z)^2)\right)\,, \tag{5.4.6}$$
$$c = (1-z)^{i\alpha_\pm}\left(c^{(0)}(x) + c^{(1)}(x)\,(1-z) + \mathcal{O}((1-z)^2)\right)\,, \tag{5.4.7}$$

with

$$\alpha = \frac{\omega}{2\sqrt{2}}\,. \tag{5.4.8}$$

where we recall that we have taken the negative sign in (3.5.11), since the negative is associated to the outgoing wave. For the coefficients in the expansions

(5.4.6) and (5.4.7) we require in accordance with (3.5.14)

$$c^{(1)} = \frac{i\omega}{4\sqrt{2}}\, c^{(0)}\,, \qquad a_t^{(0)} = 0\,, \qquad a_i^{(1)} = \frac{i\omega}{4\sqrt{2}}\, a_i^{(0)}\,; \qquad (i = x, y)\,, \tag{5.4.9}$$

while higher order coefficients are determined in terms of these. The vanishing of the term $a_t^{(0)}$ is found in the IR expansion of the equation of motion for a_t. At this stage, on behalf of simplicity it is useful to redefine the fields such that the $(1-z)^{i\alpha}$ factor be conveniently disposed of our computations can be performed using the fields

$$\tilde{a}_\mu(z,x) = (1-z)^{-i\alpha_+}\, a_\mu(z,x)\,, \qquad \tilde{c}(z,x) = (1-z)^{-i\alpha_+}\, c(z,x)\,. \tag{5.4.10}$$

in terms of which we impose at the horizon the following mixed Dirichlet and Robin boundary conditions

$$\tilde{a}_t(1,x) = 0\,, \qquad \tilde{a}_i'(1,x) = \frac{i\omega}{4\sqrt{2}}\, \tilde{a}_i(1,x)\,, \qquad \tilde{c}'(1,x) = \frac{i\omega}{4\sqrt{2}}\, \tilde{c}(1,x)\,. \tag{5.4.11}$$

Of course when interpreting the results physically, like in the computation of the conductivity, the field redefinition (5.4.10) must be reversed to convert back to the original fields we use in our definition of the conductivity (3.5.8), which would otherwise be altered. Notice in particular, that the asymptotic UV expansions to follow are written in terms of the original fluctuation fields (without tilde).

Boundary conditions at the AdS boundary

At the AdS boundary, $z \to 0$, we want our fluctuations to source an homogeneous electric field (5.4.1). The fluctuation fields behave asymptotically like the background fields, as can be verified by expanding the corresponding equations of motion

$$a_\mu(z,x) = a_\mu^{(\mathrm{b})}(x) - j_\mu(x)\, z + \mathcal{O}(z^2)\,, \qquad (\mu = t, x, y)\,, \tag{5.4.12a}$$

$$c(z,x) = c^{(\mathrm{b})}(x)\, z + \mathcal{O}(z^2)\,. \tag{5.4.12b}$$

When computing the conductivity in the direction parallel to the defect, since we need only solve for a_y, which decouples from the rest of the fluctuations, it is convenient to just impose

$$a_y(0,x) = 1\,, \tag{5.4.13}$$

which is tantamount to taking a normalisation in which the modulus of the electric field E_y is taken to be unity, $\mathfrak{e}_y = 1$. Instead, to compute σ_x we must solve for a_x, a_t, and c. Again, we want our fluctuations to source solely an electric field in the x direction

$$E_x = f_{tx} = \partial_t a_x - \partial_x a_t = i\omega a_x - \partial_x a_t \tag{5.4.14}$$

and would also like to avoid fluctuations in the mass parameter. Hence we take

$$c'(0,x) = 0\,, \tag{5.4.15a}$$

$$a_x(0,x) - \frac{1}{i\omega}\partial_x a_t(0,x) = 1\,, \tag{5.4.15b}$$

where the second condition implies that an homogeneous electric field along x, normalised to $\mathfrak{e}_x = 1$, is turned on at the boundary. In addition, in the UV we impose the fulfilment of the constraint equation resulting from the equation of motion for a_z, which reduces to

$$i\omega\,\partial_z a_t(0,x) - \partial_x\partial_z a_x(0,x) = 0\,. \tag{5.4.16}$$

Notice that in terms of the asymptotic solutions (5.4.12a) this boundary condition is nothing else than the conservation of current

$$\partial_t\left(e^{i\omega\,t} j_t(x)\right) - e^{i\omega\,t}\,\partial_x j_x(x) = 0\,. \tag{5.4.17}$$

As expected, it is straightforward to check that the partial derivative along z of the constraint equation vanishes for solutions of the equations of motion. This ensures that the constraint is satisfied for all z by any solution of the equations of motion that obeys the constraint on a constant z slice, thus it is sufficient to impose it at the boundary for it to be satisfied everywhere. Therefore, the constraint may be numerically monitored as a correctness test when performing computations.

It is worth pointing out that although we have allowed for both a_t and a_x to be non-zero at the boundary, one can proceed as in [92, 89] and apply a gauge transformation $e^{i\omega t}\,\Lambda(z,x)$ that brings the boundary field configuration to

$$a_\mu(0,x)\,e^{i\omega\,t}\,dx^\mu \to (a_\mu + \partial_\mu\Lambda(0,x))\,e^{i\omega t}\,dx^\mu = e^{i\omega\,t}dx\,, \tag{5.4.18}$$

which makes clear that the only boundary source is that corresponding to an homogeneous electric field, and other non-zero sources are just gauge artefacts. Note that one can always choose $\Lambda(z,x)$ such that it vanishes at the horizon and also satisfies $\partial_z\Lambda(0,x) = 0$ and hence $a_z(0,x) = 0$.

Summing up, in order to compute the conductivity $\sigma_y(\omega)$ we must solve the equation of motion of a_y with boundary conditions (5.4.11) and (5.4.13), and then read the conductivity from (5.4.2). On the other hand, to calculate σ_x it is necessary to solve the equations of motion of a_x, a_t, and c, imposing (5.4.11) at the horizon, and (5.4.15 - 5.4.16) at the boundary; and again read $\sigma_x(\omega)$ from (5.4.2). We will discuss the boundary conditions at the spatial boundaries when describing our numerical methods. But before that, in the next section we analyse the DC limit of the conductivity, and show how $\sigma_x^{\rm DC}$ can be computed from the background horizon data, with no need to solve for the fluctuations.

5.4.1 DC conductivity

We can follow the procedure of [42] (as applied for instance in [32] to a DBI action) and compute the DC conductivity along the direction perpendicular to the interface $\sigma_x^{\rm DC}$ in terms of the background functions evaluated at the horizon. It proves useful to define the radial coordinate ζ through

$$d\zeta = \sqrt{\frac{h(z)}{f(z)^2}}\, dz\,, \tag{5.4.19}$$

and note that the horizon (at $z=1$) is located at $\zeta=\infty$ in the new coordinate. When expressed in this coordinate, the equations of motion for the fluctuation fields $a_x(z,x)$ and $a_z(z,x)$ in the DC limit, $\omega\to 0$, respectively take the form

$$\partial_\zeta\left(\mathcal{F}(\zeta,x)\,\partial_\zeta a_x\right)=0\,,\qquad \partial_x\left(\mathcal{F}(\zeta,x)\,\partial_\zeta a_x\right)=0\,, \tag{5.4.20}$$

where we have defined

$$\mathcal{F}(z,x)=f\left(1-\chi^2\right)^{3/2}\sqrt{\frac{h}{\Gamma}}\,, \tag{5.4.21}$$

with

$$\begin{aligned}\Gamma=&-z^4h\left\{\phi'^2\left[h(1-\chi^2)+z^2\,\dot\chi^2\right]-2z^2\phi'\,\dot\phi\,\chi'\,\dot\chi+\dot\phi^2(1-\chi^2+z^2\,\chi'^2)\right\}\\&-f^2\left[h\left(\chi^2-1-z^2\,\chi'^2\right)-z^2\,\dot\chi^2\right].\end{aligned} \tag{5.4.22}$$

The equations of motion (5.4.20) ensure that the combination $\mathcal{F}\,\partial_\zeta a_x$ is a constant. It is thanks to the existence of this conserved quantity that one can express $\sigma_x^{\rm DC}$ in terms of the background functions evaluated at the horizon. First, notice that at the boundary

$$\mathcal{F}(0,x)=1, \tag{5.4.23}$$

and let us define the function

$$X(\zeta,x)=-\frac{\partial_\zeta a_x(\zeta,x)}{a_x(\zeta,x)}, \tag{5.4.24}$$

which at the horizon satisfies

$$X(\infty,x)=i\omega\,, \tag{5.4.25}$$

due to the ingoing wave boundary condition imposed on a_x. In terms of $X(\zeta,x)$, the conductivity from (5.4.2) reads

$$\sigma_x(\omega,x)=\frac{X(0,x)}{i\omega}\,a_x(0,x)\,, \tag{5.4.26}$$

where we have normalised the modulus of the electric field to one. Next, in the DC limit we can expand X in a power series in ω as

$$X(\zeta, x) = i\omega\, a(\zeta, x) + \mathcal{O}(\omega^2)\,, \tag{5.4.27}$$

and a_x and a_t at the boundary as

$$a_t(0, x) = i\omega\, p(x) + \mathcal{O}(\omega^2)\,, \tag{5.4.28a}$$
$$a_x(0, x) = 1 + \partial_x p(x) + \mathcal{O}(\omega)\,, \tag{5.4.28b}$$

where $a(\zeta, x)$ and $p(x)$ are fixed by the equations of motion (5.4.20). Moreover, notice that (5.4.28) is such that the condition (5.4.1) of having a constant electric field (with $\mathfrak{e}_x = 1$) at the boundary is automatically satisfied. At the horizon, the ingoing wave condition (5.4.25) translates into

$$a(\infty, x) = 1\,. \tag{5.4.29}$$

Plugging the expansions (5.4.27, 5.4.28) into eq. (5.4.26) we obtain

$$\sigma_x^{\mathrm{DC}} = a(0, x)(1 + \partial_x p(x))\,. \tag{5.4.30}$$

Using the definition (5.4.24) together with the expansions (5.4.27, 5.4.28), the equations of motion (5.4.20) imply that

$$\mathcal{F}(\zeta, x)\, a(\zeta, x)\, (1 + \partial_x p(x)) \tag{5.4.31}$$

is a constant. We have taken into account that $a_x(\zeta, x) = a_x(0, x) + \mathcal{O}(\omega)$. Now, notice that (5.4.31) when evaluated at $\zeta = 0$ reduces precisely to the expression (5.4.30) for the conductivity. Hence we conclude that σ_x^{DC} is a constant. By evaluating (5.4.31) at the horizon we arrive at the following expression for the DC conductivity

$$\sigma_x^{\mathrm{DC}} = \mathcal{F}(z = 1, x)\, (1 + \partial_x p(x))\,, \tag{5.4.32}$$

which is indeed a constant as required by current conservation. Notice though, that this expression for σ_x^{DC} still depends on the fluctuations through the field $p(x)$ which should in principle be determined by solving the corresponding equations of motion. However, this dependence can be eliminated and σ_x^{DC} expressed solely in terms of the background horizon data. Integrating the expression (5.4.32) over the whole sample we can write

$$\sigma_x^{\mathrm{DC}}\, \frac{1}{2L} \int_{-L}^{L} \frac{dx}{\mathcal{F}(1, x)} = \frac{1}{2L} \int_{-L}^{L} dx\, (1 + \partial_x p(x))\,, \tag{5.4.33}$$

and assuming the condition

$$\frac{1}{2L} \int_{-L}^{L} dx\, (1 + \partial_x p(x)) = 1\,, \tag{5.4.34}$$

(to be justified below) we arrive at the following expression for the DC conductivity

$$\sigma_x^{\rm DC} = \frac{2L}{\int_{-L}^{L} \frac{dx}{\mathcal{F}(1,x)}}\,, \tag{5.4.35}$$

which allows us to calculate $\sigma_x^{\rm DC}$ purely in terms of background functions evaluated at the horizon. In terms of the IR asymptotic solutions for ϕ and χ, given in eq. (5.1.9), $\mathcal{F}(z=1,x)$ can be written as

$$\mathcal{F}(z=1,x) = \frac{2\left(C^{(0)}(x)^2-1\right)^{3/2}}{\sqrt{(a^{(2)}(x)^2-2)\left(2-2C^{(0)}(x)^2+C^{(0)\prime}(x)^2\right)}}. \tag{5.4.36}$$

Let us discuss at this point the condition (5.4.34) that must be satisfied by the fluctuations. First, notice that when rewritten in terms of $a_t(z,x)$ it boils down to

$$\int_{-L}^{L} dx\, \partial_x a_t(0,x) = 0\,. \tag{5.4.37}$$

This would be automatically satisfied for a periodic system, but also in a set-up like ours if we assume that the system is long enough for the effects of the interface to fade away towards the edges of the sample. As we discuss below, it can be checked that in that case the solution for the fluctuations asymptotes towards the edges to that of an homogeneous system, for which $a_t = 0$ and then (5.4.37) holds. A more general argument for requiring (5.4.37) to hold is as follows. Notice that even though we allow a_t to be non-zero at the boundary, as illustrated by (5.4.18) our configuration is gauge equivalent to one where a_x is the only source at the boundary [92, 89]. Then, $a_t(0,x)$ is pure gauge, *i.e.* $\Lambda(0,x)$, and gauge invariance of the action in presence of a conserved current implies that $\int_{-L}^{L} dx\, \partial_x \Lambda(0,x) = 0$, which justifies the assumption (5.4.37).

5.5 Numerics for the fluctuations

We now proceed to present our numerical resolution of the equations of motion for the fluctuation fields and the subsequent extraction of the conductivities. We start by briefly describing the numerical methods employed, and specifying the boundary conditions imposed at the spatial edges of the system.

We solve the equations of motion of the fluctuation fields (5.4.10) on the same Chebyshev grid used for the background fields χ and ϕ, that is on a grid of 50×50 collocation points for the half-interval of integration. To simplify the numerics, again we make use of the parity along x of the fields in our problem, namely

$$\begin{aligned} &a_t(z,x) = -a_t(z,-x)\,, \qquad a_x(z,x) = a_x(z,-x)\,, \\ &c(z,x) = c(z,-x)\,, \qquad a_y(z,x) = a_y(z,-x)\,, \end{aligned} \tag{5.5.1}$$

which follows straightforwardly from the linear equations of motion taking into account that the background fields satisfy (5.2.4). As in the case of the background, this allows us to actually solve for half the system, between $x = -L$ and $x = 0$, and given the distribution of points in a Chebyshev grid, greatly increases the resolution close to the interface, where the gradients in x are larger. The IR and UV boundary conditions are given by eqs. (5.4.9, and 5.4.13 -5.4.16) as discussed above.

Regarding the boundary conditions at the spatial edges, $x = \pm L$, again, periodic boundary conditions cannot be used due to the symmetry of the problem. Let us focus first on the the three coupled fields a_t, a_x, and c, which allow us to compute σ_x. By studying the asymptotic form of the coupled PDEs at the spatial boundaries, one can show that a solution is completely determined once the values of a_t and c, or those of their derivatives $\partial_x a_t$ and $\partial_x c$, are fixed at each spatial boundary. Solving the system asymptotically at one edge, once the values of a_t and c and their derivatives, $\partial_x a_t$ and $\partial_x c$, are fixed, and taking into consideration the UV and IR boundary conditions, the asymptotic solutions for a_x, a_t and c are completely fixed. Then, to fully determine a solution of the system one may set the values of a_t and c, and their derivatives, at one edge, or equivalently impose two conditions at one edge and two more at the other. We consider fixing a_t and c both at $x = L$ and $x = -L$, or, alternatively, fix $\partial_x a_t$ and $\partial_x c$ at $x = \pm L$. The case of a_y is simpler, for a single linear PDE has to be solved and as spatial boundary conditions we either fix the value of the function or of its derivative $\partial_x a_y$, at the spatial boundaries.
Both when computing σ_x and σ_y two different sets of boundary conditions may be considered, which we now describe.

5.5.1 Damping boundary conditions. Long systems

A reasonable boundary condition is derived from the assumption that the system is long enough for all the inhomogeneities sourced by the interface to die away towards the edges, that is from the requirement that the fluctuations become independent of x there, namely

$$\partial_x a_t(z, \pm L) = 0\,, \qquad \partial_x c(z, \pm L) = 0\,, \tag{5.5.2}$$

while a_x is left free as discussed above.
To compute the conductivity in the direction parallel to the interface (σ_y) we only need to solve for a_y. The damping boundary condition at the spatial boundaries is then

$$\partial_x a_y(z, \pm L) = 0\,. \tag{5.5.3}$$

5.5.2 Boundary conditions. Short systems

One can instead be interested in a situation in which the system is not long enough for the inhomogeneities of the fluctuations to vanish towards the spa-

tial edges. In this case these fields may reach the boundary with a non-zero derivative along x, then, those fields have a non-zero derivative at the boundary, and Dirichlet boundary conditions may be imposed there instead of Neumann ones. As discussed in the previous section, a_t, which is odd, must obey (5.4.37), hence an alternative boundary condition that allows for a non-zero $\partial_x a_t$ at the boundary is

$$a_t(z, \pm L) = 0\,. \tag{5.5.4}$$

Analogously we require c to also vanish at the boundaries

$$c(z, \pm L) = 0\,. \tag{5.5.5}$$

Notice that these boundary conditions are nothing else than the requirement that a_t and c reach the solution of the homogeneous problem exactly at the edge. We should bear in mind that when computing the conductivity σ_x of an homogeneous system, only a_x has to be turned on, hence c and a_t, which decouple from a_x, vanish identically. It is straightforward to check, both analytically and numerically, that these boundary conditions are satisfied whenever the previous more restricting damping boundary conditions are imposed. Yet the opposite is not true, and for short enough systems the solutions are such that $\partial_x a_t$ and $\partial_x c$ are non-vanishing at the spatial boundaries.
Finally, for a_y one could also consider a Dirichlet boundary condition which requires that a_y reach the homogeneous solution at the boundary, namely the solution for a_y in a homogeneous background characterised by the values of the chemical potential and the mass far away from the interface

$$a_y(z, \pm L) = a_y^{\text{hom}}(z)\,. \tag{5.5.6}$$

Except for when we specifically focus on long systems and so specify (fig. 5.14), in the rest of this work we consider our systems to be short, and consequently impose the boundary conditions above. In particular, we set $L = 10$ and fix $a = 3$ in (5.1.12), as discussed in section 5.3. Moreover, as for the background, we use grids of size 50×50, except for the results plotted in figures 5.11 and 5.12 which were obtained with a grid of size $N_z \times N_x = 50 \times 35$.

5.6 Solution of the fluctuations and conductivities

We now present our numerical results for the fluctuation fields and the conductivities extracted from them via the expressions (5.4.2) for the AC conductivity and (5.4.32) for the DC conductivity. The codes employed are shown in detail in appendix D. In figures 5.6 and 5.7 we show a case of the solutions found for the fluctuation fields in the middle frequency range. In figures 5.8 and 5.9 we show results in the smallest frequency we achieve numerically for comparison. Note in particular how the fields de-localise in the direction transverse to the

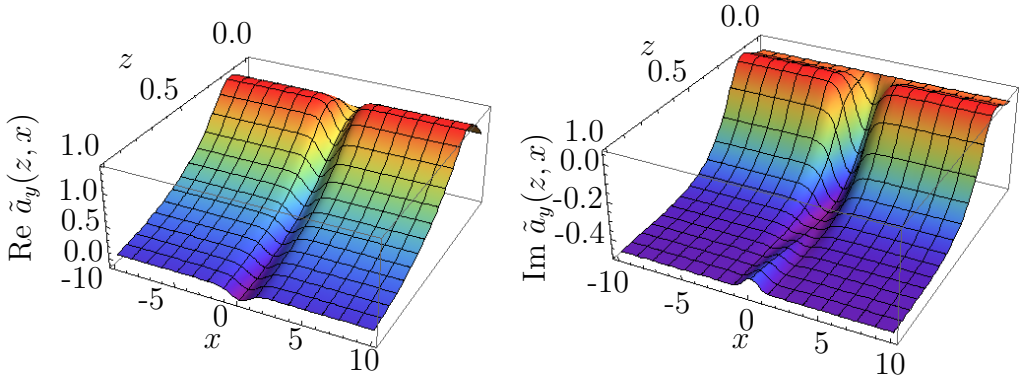

Figure 5.6: Numerical solutions obtained for the fluctuation fields a_y for $M = 5$, $\mu = 4$ at $\omega = 5$. The real part are shown in the left panel and the imaginary part in the right panel.

defect interface at low frequencies. Notice as well that we plot the tilded fields (5.4.10) everywhere, as the numerics are carried out in terms of them.

Once the fluctuations fields are known, one may proceed to compute the corresponding conductivities. After a glance at the optical conductivity for the entire range of the coordinate x, we focus on its behaviour at the interface and then go on to study the DC conductivity in more detail. In figure 5.10 we plot the real part of the optical conductivities σ_x and σ_y as functions of the frequency ω, and the position x for a background with $\mu = 4$ and b$M = 5.3$. At intermediate and large frequencies, and away from the interface, both conductivities are very similar, not only to each other, but also to the conductivity of the equivalent homogeneous system, *i.e.* the one given by an homogeneous embedding with the same values of mass and chemical potential that characterise our system away from the interface. In particular, we observe the presence of the resonances given by the quasi-normal modes corresponding to the 'melting' vector mesons. In fact, as found in [70], the effective meson masses, which correspond to peaks in the spectral function, are in one-to-one relation with the frequencies

$$\omega_{\text{res}} = m\sqrt{2(k+1)(k+2)}\,, \qquad k = 0, 1, 2, \dots\,, \tag{5.6.1}$$

which correspond to the masses of stable mesons [104]. The peaks we observe gradually approach these values as the configuration gets closer to the Minkowski region in figure 3.6.
The similarity of both conductivities at high values of the frequency is no surprise given the fact that short-range distances are probed in that range of frequencies and hence the effects of the localised inhomogeneity become less and less relevant. The similarity towards the spatial edges was also to be expected inasmuch as the effects of the inhomogeneity fade away there by means of the boundary conditions (5.5.2) and (5.5.2) or (5.5.4), (5.5.5) and (5.5.6). Instead, at low frequencies, when the system is probed in the long-range it

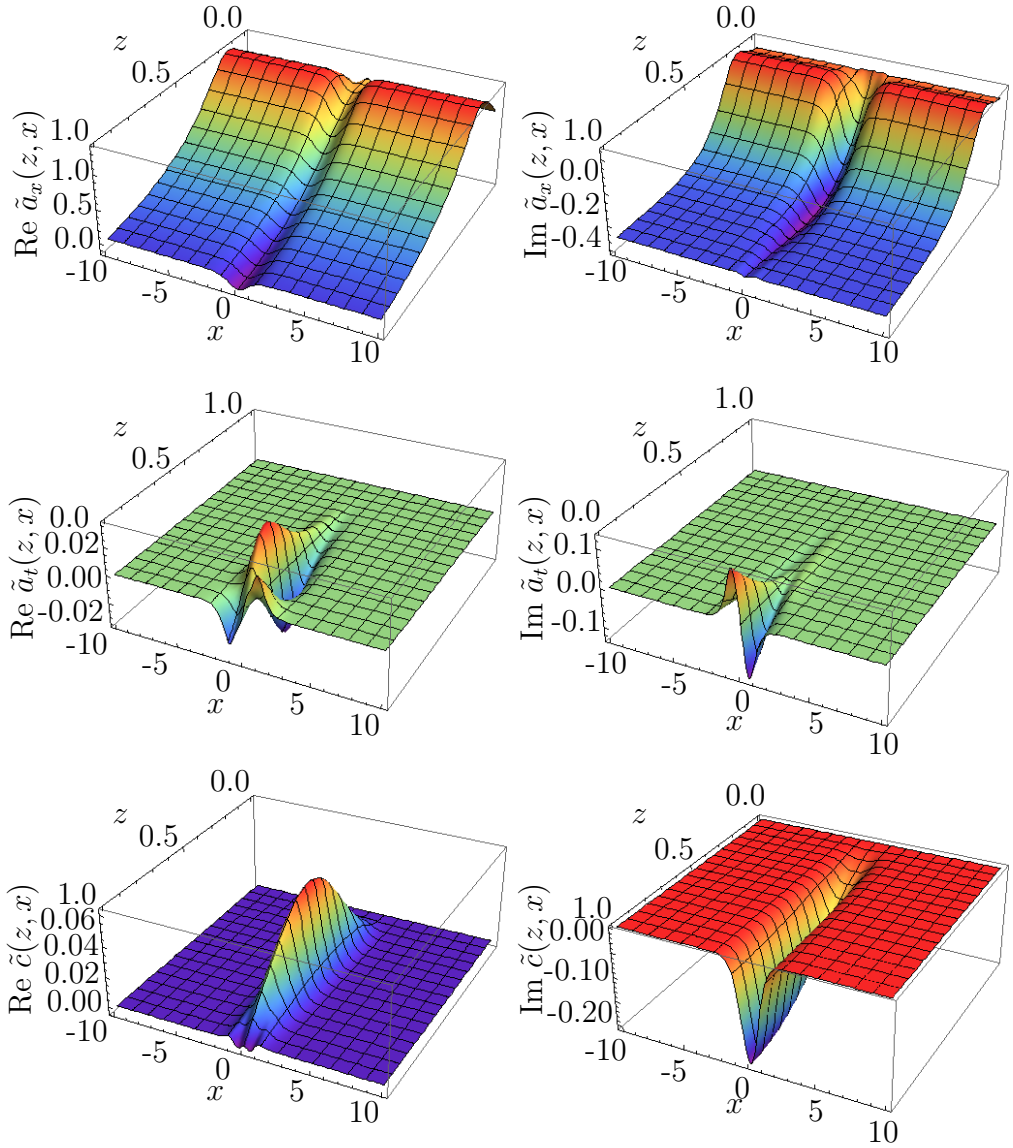

Figure 5.7: Numerical solutions obtained for the fluctuation fields a_x, a_t and c in a short system (with (5.5.4)) for $M = 5$, $\mu = 4$ at $\omega = 5$. Notice that the z axis is inverted in the plot for a_t. The real parts are shown in the left panel and the imaginary part in the right panel.

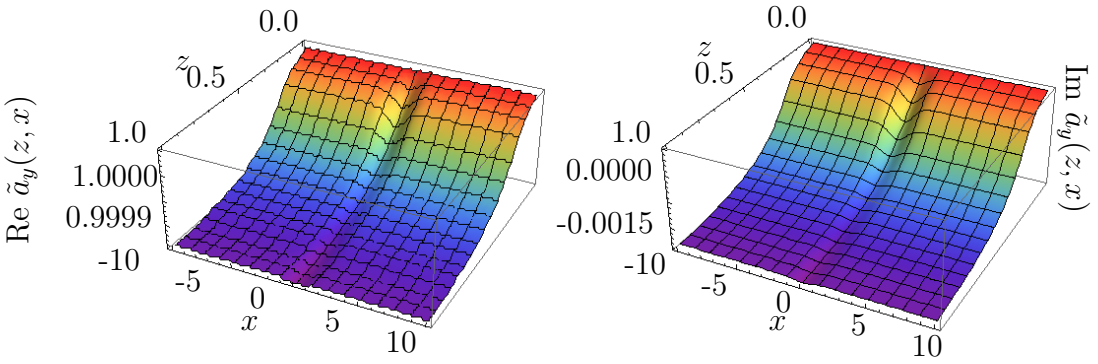

Figure 5.8: Numerical solutions obtained for the fluctuation fields a_y for $M = 5$, $\mu = 4$ at $\omega = 10^{-3}$. The real part are shown in the left panel and the imaginary part in the right panel.

becomes more and more sensitive to the effects of the localised inhomogeneity as the frequency decreases. Indeed we see that the conductivity in both directions differ in this regime.

As to the conductivity along the direction parallel to the defect, in a system like ours, homogeneous along the y direction, one could naively expect that at each point x, the conductivity in the y direction, $\sigma_y(\omega, x)$, be very similar to that of an homogeneous system having the same mass and chemical potential as our set-up at that point, which we denote by ft$\sigma_y^{\rm h}$. However, $\sigma_y(\omega, x)$ turns out to be sensitive to the spatial gradients of the inhomogeneous embedding, and therefore becomes different from $\sigma_y^{\rm h}$ where the spatial gradients are large. To illustrate this, in figure 5.11 we plot $\sigma_y(\omega)$ and $\sigma_y^{\rm h}(\omega)$ at the point where the difference between them is maximal, which is of course close to the interface. Interestingly, with respect to the equivalent homogeneous case we observe a transfer of spectral weight from intermediate to very low frequencies resulting in a larger DC conductivity in the presence of the interface. Moreover, we have checked that the relative enhancement increases with decreasing μ for a given M as one moves toward the phase transition in the phase diagram 3.6. The spatial gradients due to the interface affect the conductivity $\sigma_y(\omega, x)$ in two ways. The most important effect occurs at the level of the background fields χ and ϕ: the non-zero spatial gradients of these fields result in a value of the charge density $\rho(x)$, which near the interface is higher than that of a homogeneous system with the same values of mass $m(x)$ and chemical potential μ. This is shown in the left panel of figure 5.12 where we compare both charge densities, and see that indeed, around the interface, the charge density of the inhomogeneous case is always larger. Consequently, one expects $\sigma_y(x)$ and $\sigma_y^{\rm h}(x)$ to differ, and in particular, the DC value of $\sigma_y(x)$ to be higher than that of $\sigma_y^{\rm h}$. This is in agreement with what we see in fig. 5.11. Note that this effect, due to the the enhancement of the charge density around the interface, would be there even if the form of the equations of motion for the fluctuations

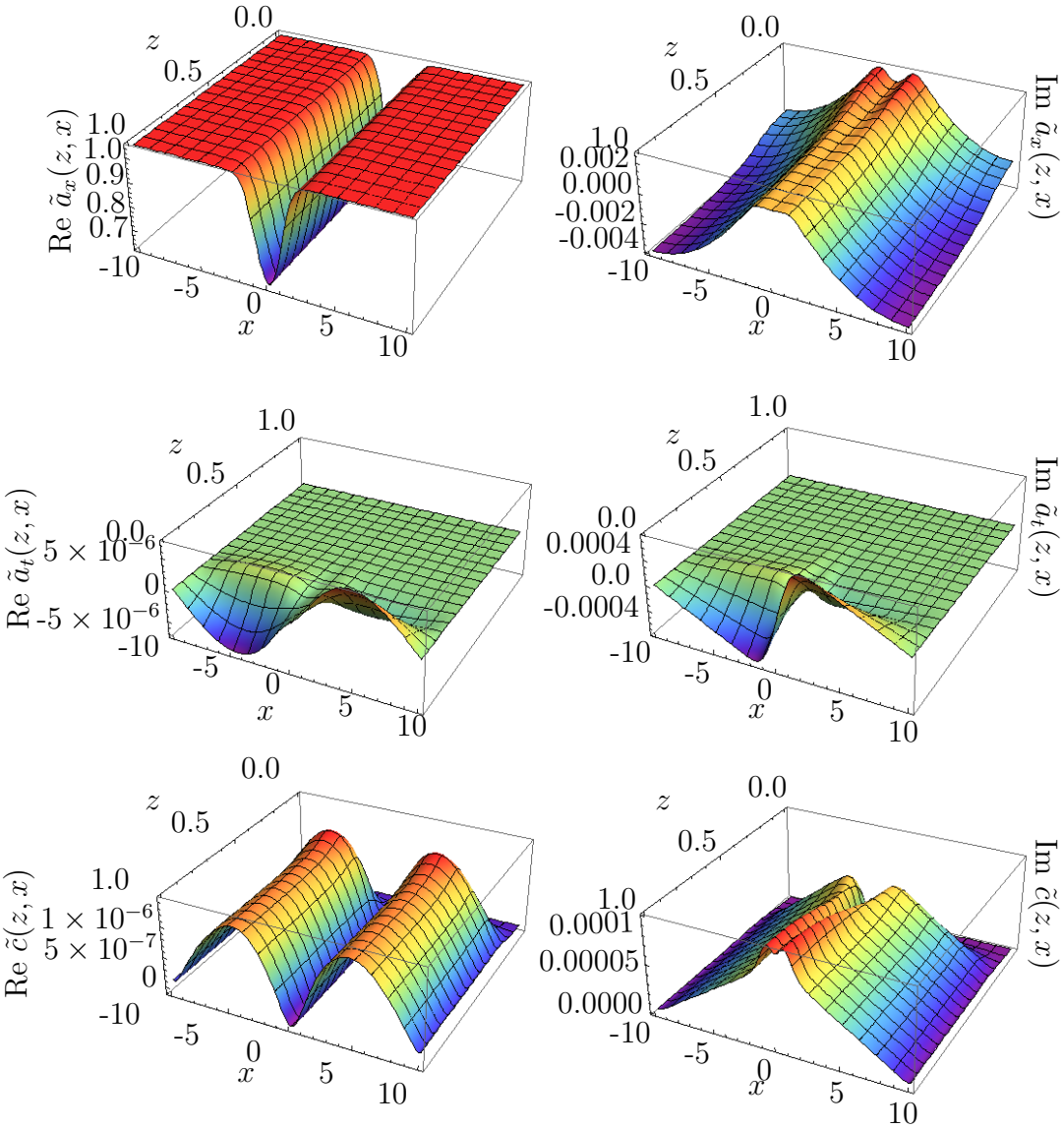

Figure 5.9: Numerical solutions obtained for the fluctuation fields a_x, a_t and c in a short system (with (5.5.4)) for $M = 5$, $\mu = 4$ at $\omega = 10^{-3}$. Notice that the z axis is inverted in the plot for a_t. The real parts are shown in the left panel and the imaginary part in the right panel.

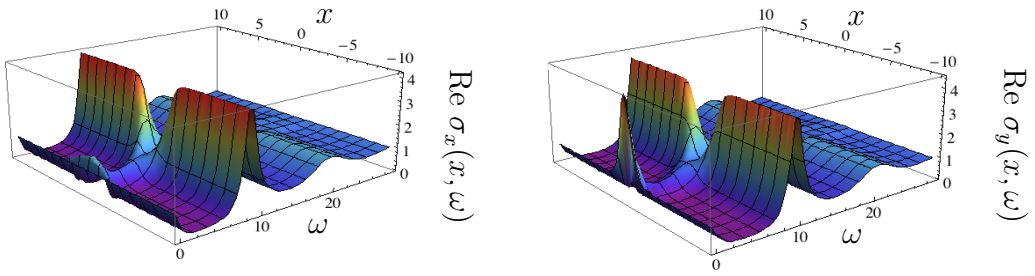

Figure 5.10: Real optical conductivities as a function of frequency and position, for a background with $\mu = 4$ and $m = 5.3$. Notice that the main differences between σ_x and σ_y occur at low frequencies, and close to the interface ($x = 0$).

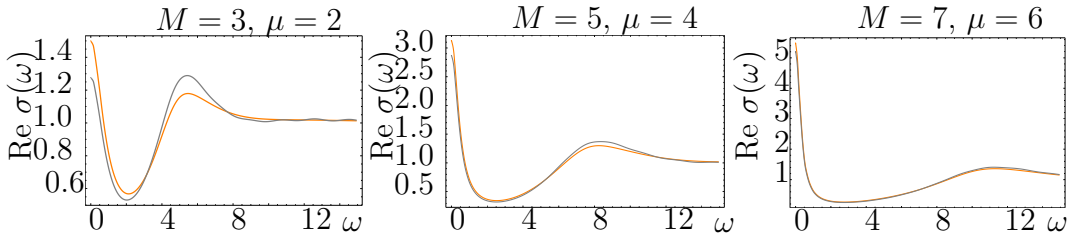

Figure 5.11: Plots of the real part of $\sigma_y(\omega)$ (orange lines) at a point $x = x_0 = 0.749$ in the vicinity of the interface for different pairs of values (M, μ). The grey line stands for the equivalent homogeneous conductivity $\sigma_y^{\rm h}(\omega)$, obtained for an homogeneous system with the same mass $m = m(x_0)$, and chemical potential as our set-up at that point (from left to right $m(x_0) = 2.4262$, 4.044, and 5.661 respectively).

were not changed with respect to the homogeneous case.
The second effect occurs at the level of the equations of motion of the fluctuations. Notice that while the fluctuation a_x is coupled to those of the embedding and the charge density, c and a_t, the field a_y decouples from any other fluctuation, as it happens in the homogeneous case. However, the DBI action does couple a_y to the spatial derivatives of the background functions, $\dot{\phi}$ and $\dot{\chi}$, as can be seen in (C.0.5). Hence, there are new terms in the equation of motion for a_y that are not present in the homogeneous case, so one expects these terms to affect the conductivity.

To try and assess the relevance of these two effects, on the right panel of figure 5.12 we compare the conductivity $\sigma_y(\omega)$, computed at a point x (orange line), with the one that results for a system with the same value of the chemical potential and the charge density as our system at that point x (purple line). Although the purple line does not exactly overlap with the orange one, it is much closer to it than the gray line, which as in figure 5.11 stands for $\sigma_y^{\rm h}$. This confirms that, as expected, the enhancement of the charge density due to the spatial inhomogeneities is the dominant effect of the interface on σ_y.

We now focus on the behaviour of the conductivities at the interface. In

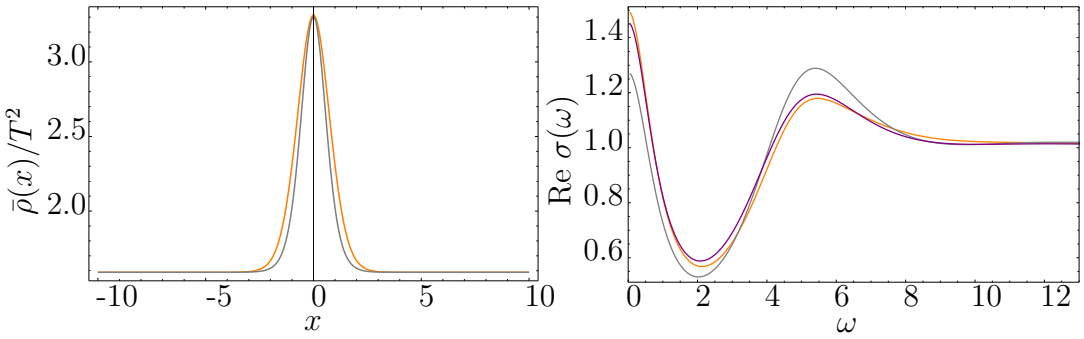

Figure 5.12: On the left panel we plot the charge density (orange line) for a set-up with $M = 3$ and $\mu = 2$. The gray line corresponds to the charge density of the equivalent homogeneous system at each point x, namely a homogeneous system with the same mass $m(x)$ as our set-up at that point. On the right we plot the same conductivities as in the leftmost plot of fig. 5.11 (orange and gray lines) together with the conductivity obtained for an homogeneous system with $\mu = 3$ and $m = 2.095$ (purple line). This last system has the same value of the charge density as the inhomogeneous set-up at the point of interest ($x = 0.749$).

figure 5.13 we plot both σ_x and σ_y at the interface for three different values of the background parameters M and μ. We have chosen the pairs of values (M, μ) so that they correspond to systems where the charge density at the edges is kept low, namely configurations at the edge of the area accessible to black hole embeddings in fig. 3.6. At the interface the embedding becomes massless, thus the configurations with higher values of μ correspond to lower temperatures and higher values of the charge density. By looking at the plots of the real part of the conductivities at the interface, presented on the right panels of figure 5.13, we observe one of the main features of our construction: the DC conductivity along the interface ($\sigma_y^{\rm DC}$) is considerably enhanced with respect to that in the direction perpendicular to it ($\sigma_x^{\rm DC}$). This is a direct consequence of the spatial distribution of the charge density in our system. See fig. 5.5 for an example of $\rho(x)$. As we have seen in fig. 5.11, the conductivity $\sigma_y(\omega)$ is basically determined by the value of the charge density at the point of interest, in this case $x = 0$. However, this is not the case for the conductivity in the x direction $\sigma_x(\omega)$. As we discuss below, when focusing on $\sigma_x^{\rm DC}$, the DC conductivity along the x direction, which must be independent of x due to current conservation, is basically determined by the charge density at the edges of the system, which is much lower than that at the interface. Therefore $\sigma_x^{\rm DC}$ is suppressed with respect to $\sigma_y(\omega)$. This suppression is maximal for embeddings such that the charge density at the edges is arbitrarily small. Nevertheless, $\sigma_x^{\rm DC}$ never vanishes completely, since there is always a contribution from the thermally produced pairs of charge carriers [105].

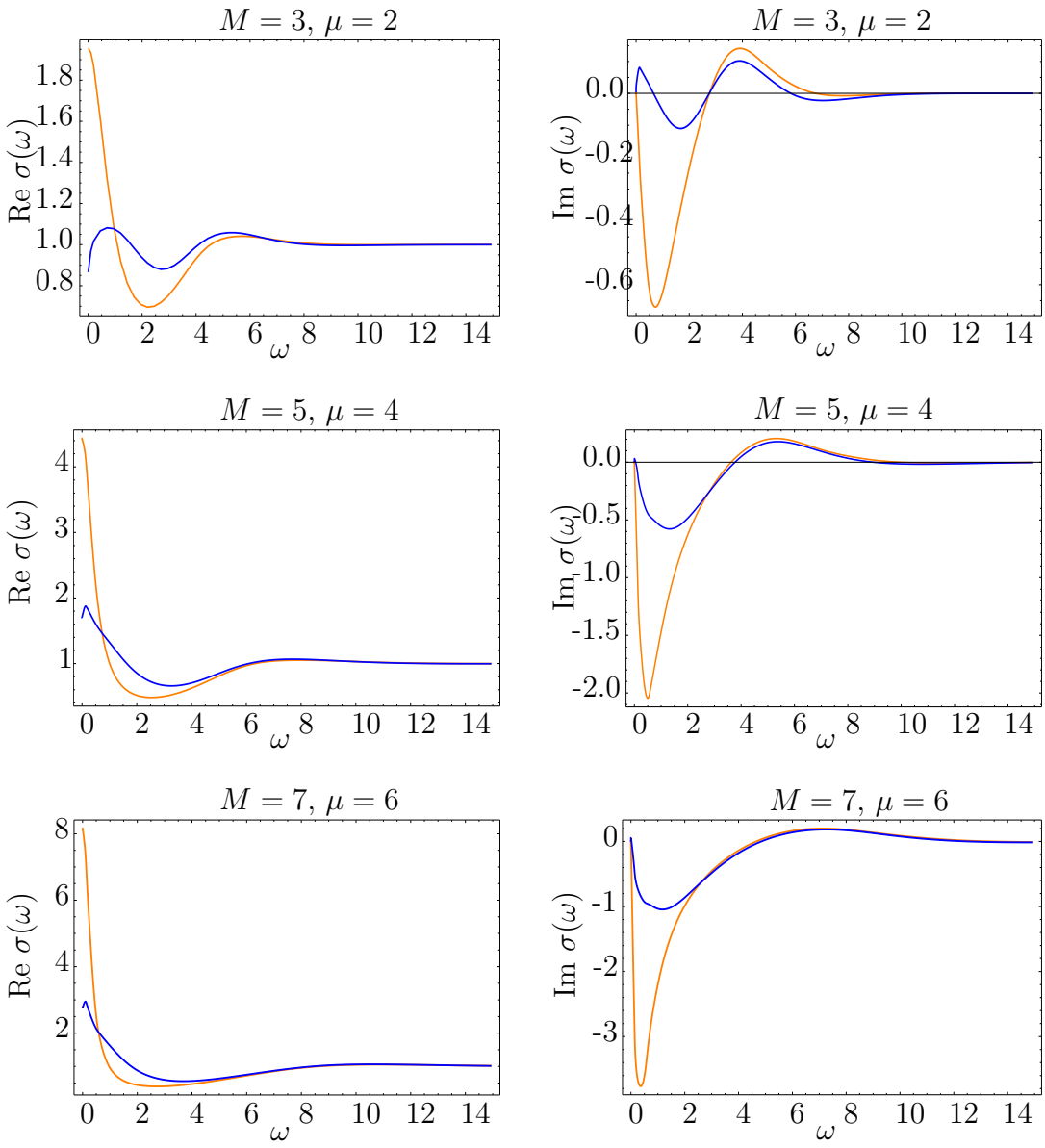

Figure 5.13: Conductivities at the interface. Plots of the conductivity $\sigma_x(x = 0, \omega)$ (blue) and $\sigma_y(x = 0, \omega)$ (orange) for different values of the background parameters M and μ. The real parts are shown on the left and the imaginary parts on the right.

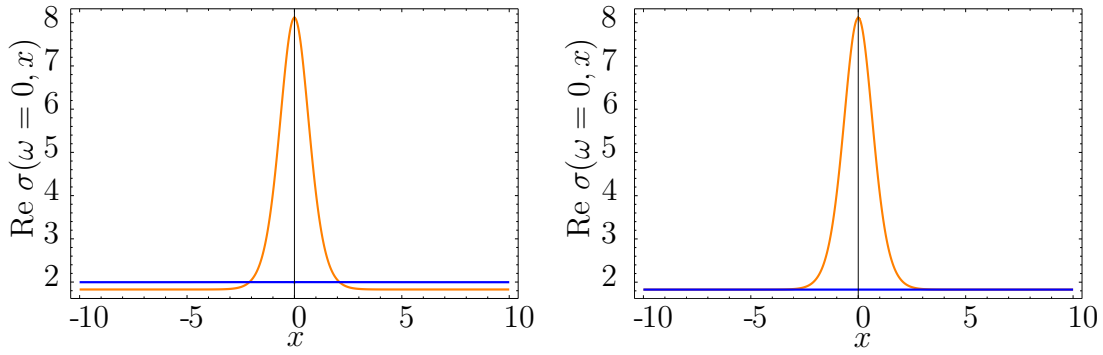

Figure 5.14: Comparison of $\sigma_x^{DC}(x)$ (blue) and $\sigma_y^{DC}(x)$ (orange) for a set-up with $\mu = 4$ and $M = 5.3$. On the left panel we plot the results for a short system, for which we set $L = 10$. The right panel corresponds to a long system where $L = 100$. In both cases we have set $a = 3$ (remember that a determines the width of the interface via eq. (5.1.12)).

DC conductivity

We now pay closer attention to the DC conductivity along the direction orthogonal to the interface, namely $\sigma_x^{\rm DC}$. As suggested by the action of the fluctuations (C.0.5), σ_x is more sensitive to the effects of translational symmetry breaking introduced by our inhomogeneous embedding. In addition, as can be seen from the current conservation equation (5.4.17), for a set-up like ours, in which the charge density does not vary with time and in the presence of a co-dimension one impurity and hence of a charge density that only depends on x, $\sigma_x^{\rm DC}$ is a constant. Moreover, as we have described in section 5.4.1, it is possible to compute $\sigma_x^{\rm DC}$ from the behaviour of the background functions at the horizon in the $\omega \to 0$ limit without having to solve the fluctuation equations. Note that eq. (5.4.36) is particularly well suited to numerical evaluation for this purpose. In fact, (5.4.36) is the expression we evaluate numerically to read out the value of $\sigma_x^{\rm DC}$ once the corresponding fluctuation fields have been computed. A field redefinition of the form

$$\phi \to (1-z)^2 \bar{\phi} \tag{5.6.2}$$

eliminates the need to evaluate a term containing a second derivative like $a^{(2)}(x)$ and replaces it by a leading term, which is always more precise than a second derivative in numerical terms.

We start by comparing the DC conductivities $\sigma_x^{\rm DC}$ and $\sigma_y^{\rm DC}$. They are plotted in figure 5.14 for the two kinds of systems introduced in section 5.5. Let us first describe what we expect for $\sigma_y^{\rm DC}$, and then discuss $\sigma_x^{\rm DC}$ in detail.

The DC conductivity along the direction parallel to the interface, $\sigma_y^{\rm DC}(x)$, is read from the $\omega \to 0$ limit of the AC conductivity $\sigma_y(\omega, x)$, for no direct equation is available as for $\sigma_x^{\rm DC}(x)$. As shown in fig. 5.11, up to a constant

[105] and to some small effects sourced by the spatial gradients of the background, $\sigma_y^{\mathrm{DC}}(x)$ is determined by the value of the charge density at each point x. Hence, it is expected to peak at the interface, where the charge density is maximal, and to asymptote to a non-zero baseline value towards the edges.

In section 5.4.1 we discussed how to compute σ_x^{DC} in terms of the horizon data. Subsequently, in section 5.5 we defined two different kinds of systems corresponding to different boundary conditions for the fluctuations at the edges. These result in slightly different behaviours of σ_x^{DC} according to whether the system can be considered to be short or long.

Long Systems

For these systems the effects of the interface fade away towards the edges. Consequently, in eq. (5.4.32) we can use the boundary condition (5.5.3),

$$\partial_x p(\pm L) = \partial_x a_t(0, \pm L) = 0, \tag{5.6.3}$$

to get

$$\sigma_x^{\mathrm{DC}} = \mathcal{F}(z = 1, x = \pm L)\,, \tag{5.6.4}$$

which is the DC conductivity of a system without an interface, since $\mathcal{F}$ at the edges agrees with that of a background with an homogeneous embedding. Notice that this is to be expected. Assuming that the effect of the interface does not reach the edges amounts to having a system where the width of the interface is negligible with respect to the total length. Therefore we expect σ_x^{DC} to be the same as $\sigma_y^{\mathrm{DC}}(x = \pm L)$, namely σ_y^{DC} at the edges.
On the right panel of figure 5.14 we plot σ_x^{DC} and σ_y^{DC} for a long system, and we observe that they overlap away from the interface.
It ought to be taken into account, that when solving a long system, L must be big enough compared to the interface, whose size is somewhat fixed by a. With our choice $a = 3$, $L = 100$ was good enoug for the assumption to be reasonable but different combinations of L and a may be taken.

Short Systems

We also considere the case of a system where the effects of the interface reach the boundary by allowing the derivatives of the fluctuations to be non-zero at the edges. In that case, it is still possible to compute σ_x^{DC} by means of the integral (5.4.35).
On the left panel of figure 5.14 we plot σ_x^{DC} and σ_y^{DC} for a short system. We see that σ_x^{DC} is slightly larger than σ_y^{DC} at the edges. The interface now represents a non negligible region along the x direction compared to the length of the system where the charge density is augmented, producing a net enhancement of the conductivity σ_x^{DC}.
In fact, in order to roughly estimate the DC conductivity σ_x^{DC}, we may draw

an analogy to electric resistors and think of the system as made up of two regions: one region of length ϵ and conductivity $\sigma^{\rm int}_{\rm DC}$, corresponding to the interface and another region of length $2L-\epsilon$ and conductivity $\sigma^0_{\rm DC} < \sigma^{\rm int}_{\rm DC}$, corresponding to the system away from the interface. One can then write

$$\frac{2L}{\sigma_x^{\rm DC}} = \frac{2L-\epsilon}{\sigma^0_{\rm DC}} + \frac{\epsilon}{\sigma^{\rm int}_{\rm DC}} \tag{5.6.5}$$

hence, when $\epsilon \ll L$, $\sigma_x^{\rm DC} = \sigma^0_{\rm DC}$. Instead for $\epsilon \lesssim L$ we have $\sigma_x^{\rm DC} \gtrsim \sigma^0_{\rm DC}$. We consider it worth mentioning that this analogy also works for non-symmetric systems having the mass profile $m(x)$ interpolating between different masses at both sides of the interface. In that case we have a composition of the form

$$\frac{2L}{\sigma_x^{\rm DC}} = \frac{L-\epsilon/2}{\sigma^1_{\rm DC}} + \frac{\epsilon}{\sigma^{\rm int}_{\rm DC}} + \frac{L-\epsilon/2}{\sigma^2_{\rm DC}}, \tag{5.6.6}$$

which in the limit of a very long system in which the size of ϵ is negligible turns into

$$\sigma_x^{\rm DC} = \frac{2\sigma^1_{\rm DC}\sigma^2_{\rm DC}}{\sigma^1_{\rm DC}+\sigma^2_{\rm DC}}, \tag{5.6.7}$$

which is the common law for the association of resistivities arranged in line. If instead ϵ has a significant size compared to the length of the system we shall have a contribution from the interface region and the resultant conductivity $\sigma_x^{\rm DC}$ will deviate from the previous equation.
Although we did check the fulfilment of the above numerically, we did not pursue this kind of embeddings further.

In figure 5.15 we illustratively summarise the behaviour of the DC conductivities in our system. As is clear from the illustration, $\sigma_y^{\rm DC}(x)$ roughly follows the charge density, which varies along x and peaks at the interface, while $\sigma_x^{\rm DC}$ is constant, its value mainly determined by the charge density away from the interface.

In figure 5.16 we study the evolution of $\sigma_x^{\rm DC}$ as a function of $1/\mu \propto T$, at fixed M/μ. We perform the analysis for a short system with $L=10$, and in order to study the effect of the interface, we compare $\sigma_x^{\rm DC}$ to the conductivity of an equivalent homogeneous system $\sigma^0_{\rm DC}$. This is the DC conductivity for an homogeneous system with the same mass M and chemical potential μ as our set-up at its edges. Notice that for the values of M/μ considered, there is a minimum value of $1/\mu$ that can be reached by our embeddings (see fig. 3.6). Both conductivities grow as we lower the temperature, $1/\mu$, until they reach a maximum, and then decrease rapidly. As is clear from the plots, the behaviour of the conductivity follows closely that of the charge density at the edges (blue dashed line). Moreover, $\sigma_x^{\rm DC}$ is always slightly larger than the homogeneous counterpart $\sigma^0_{\rm DC}$ as expected from the length of the system. Also note that, with respect to an homogeneous system, the presence of the interface has two competing effects on the DC conductivity. On the one hand, the interface

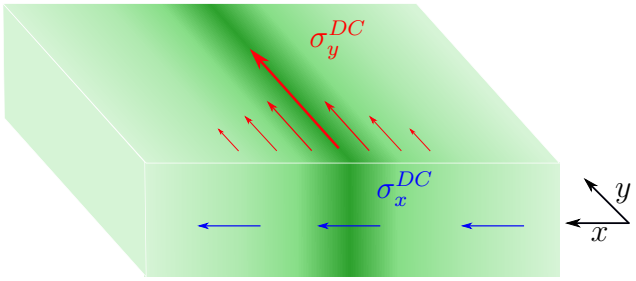

Figure 5.15: Schematic illustration of our set-up. The system is two-dimensional; the third (vertical) dimension has been added for illustrative purposes. The intensity of green encodes the x-dependence of the charge density (see fig. 5.5), with darker green standing for larger charge density. The red arrows represent the value of $\sigma_y^{\rm DC}$, which varies along the system, and the blue arrows denote the value of $\sigma_x^{\rm DC}$, which is constant.

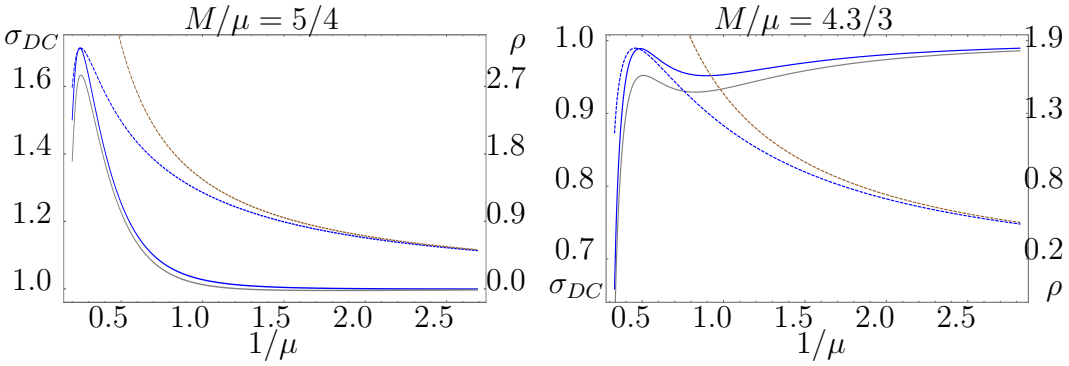

Figure 5.16: DC conductivity versus $1/\mu \propto T$. The solid blue line corresponds to $\sigma_x^{\rm DC}$, while the solid grey line represents $\sigma_{\rm DC}^0$, which corresponds to a system with no interface. For guidance we also plot the values of the charge density at the edges (blue dashed lines) and at the interface (gray dashed lines). The left panel corresponds to a set-up with $\mu/M = 4/5$. The right panel is for $\mu/M = 3/4.3$. The left vertical axes refer to the conductivity plots whereas the right ones show the scale for the charge density.

is a region of small size where the charge density is much larger than in the homogeneous system towards the edges. This fact, as we have seen when discussing the plots in fig. 5.14, should result in an enhancement of $\sigma_x^{\rm DC}$. On the other hand, the presence of the interface gives rise to inhomogeneities that, on general grounds, should impede the conductivity [32]. However, in view of our results we can assert that the enhancement of the charge density is strong enough to overcome other effects of the inhomogeneous embedding.

5.7 Concluding remarks

In this chapter we have constructed a system that realises holographically a one-dimensional charged interface in a strongly coupled medium at finite temperature and finite density of fundamental particles acting as charge carriers. The main results are:

- We have computed the AC and DC conductivities both in the direction parallel to the interface, σ^y, and in the one orthogonal to it, σ^x. Away from the interface both conductivities coincide and agree with that of an homogeneous system corresponding to an embedding with constant mass m.

- Due to current conservation, $\sigma^x_{\rm DC}$ is independent of x for a system with a co-dimension one impurity like ours. Following [42, 32], we can express $\sigma^x_{\rm DC}$ purely in terms of horizon data, *i.e.* the behaviour of the functions describing the embedding at the black hole horizon. This DC conductivity is dominated by the system away from the interface, where the charge density is very low.

- The DC conductivity is enhanced along the interface. We observe that $\sigma^y_{\rm DC}(x=0)$ is bigger than $\sigma^x_{\rm DC}$. While the latter is determined by the system away from the interface, where the charge density can be very low, $\sigma^y_{\rm DC}(x=0)$ is roughly proportional to the value of the charge density at the interface, and is therefore strongly enhanced with respect to $\sigma^x_{\rm DC}$.

- The translational symmetry breaking effects sourced by the interface result in an enhancement of $\sigma^y_{\rm DC}$ in its vicinity. Although the system is homogeneous in the y direction, owing to the non-linearities of the DBI action, a current along the y direction is sensitive to the gradients along the x direction of the embedding fields. We observe a transfer of spectral weight in σ^y from mid to low frequencies, resulting in an enhancement of $\sigma^y_{\rm DC}$.

- The balance of the competing effects that the presence of the interface has on the DC conductivity in the transverse direction, $\sigma^x_{\rm DC}$, depends on the relative width of the interface with respect to the total length of the system. When that width is negligible, $\sigma^x_{\rm DC}$ is just determined by

the homogeneous system away from the interface. On the other hand, when the interface has a sizeable width, it enhances $\sigma^x_{\rm DC}$. The interface introduces two competing effects: an increase of the charge density on the one hand and the presence of inhomogeneities along x on the other. Although, as discussed in [32], these inhomogeneities should suppress the conductivity, we observe that the interface always produces an increase of $\sigma^x_{\rm DC}$ with respect to an embedding with constant mass m.

Chapter 6

Holographic charged disorder at brane intersections

In the previous chapter we used the material presented in chapters 3 and 4 to solve real cases of holographic systems in which translation invariance is broken in one of the boundary directions, which we usually call x. There, it was the presence of a kink profile which introduced a localised inhomogeneity and hence broke translational symmetry having notable effects on physical variables like the conductivities. In this chapter, we want to build on what was made in the previous one but instead of dealing with localised inhomogeneities we turn our attention to de-localised random disorder or noise.

In realistic condensed matter systems disorder plays an eminent part. If it is sufficiently pronounced it may lead to the localised of electron wavefunctions in a metal, thereby suppressing the conductivity. Such a phenomenon is known as Anderson localisation and Anderson metal-insulator phase transition [106, 107, 108, 109], see [110] for a review.
Given the difficulties inherent to disorder, there is still no theoretical full control of many aspects of it. In particular, very little is known about disorder at strong coupling. AdS/CFT again provides a natural framework to study such systems, given that it gives us access to that regime via a weakly coupled theory of gravity. It is therefore interesting to learn how to model disorder in an holographic way so as to better understand how strongly coupled systems behave in its presence.

In this chapter, based on the author's work [44] we adapt the set up of chapter 5 ([43]) to the inclusion of random noise. Again, we consider a top-down model involving a D5 probe brane. The embedding is now exactly the same one presented in 5.1. In particular equations (5.1.1) to (5.1.11) apply here exactly as they are. The difference lies within the way in which we introduce inhomogeneities. We now wish to study the effect of impurities, whose presence we incorporate by means of a random spatial dependence in the chemical

potential. We do this inspired by previous works in the context of superconductors in [27, 28]. Given that the chemical potential defines the local energy of the charge carriers, such a construction mimics the disorder in their local energy and reproduces better the physics of real materials [28]. With this system we study the effects of the noise upon the charge density and the conductivities

The behaviour of the conductivity in 2+1 dimensional disordered systems like ours was analysed from an AdS/CFT perspective by means of D-brane probe systems in [32]. The conclusion was drawn there, that random disorder in the charge density increases the conductivity at high temperature and suppresses it as the temperature goes down. We compare our results to this prediction and find good qualitative agreement.
Our studies are furthermore motivated by attempts within condensed matter physics to better understand the transport properties of graphene in the presence of charged impurities. Graphene is a natural material to refer to when dealing with the transport properties of strongly coupled materials. At low energies, it is described by a relativistic theory in 2+1 dimensions with a chemical potential and its dynamics can be reproduced holographically [33]. The current models for graphene in condensed matter theory transport theories are not universally accepted, nor do they provide an explanation to all experimental observations. The improvement of the existing models for graphene is therefore a relevant goal in condensed matter physics given its theoretical and technological interest.
One of the most studied properties of graphene is its electrical conductivity as a function of the applied gate voltage, which is directly related to the carrier density [34]. In [35, 36], different models were presented to account for the effect of spatially correlated impurity disorder in two-dimensional graphene layers upon the dependence between the charge density and the conductivity. Here we also pay attention to this dependence between the charge density and the conductivity and compare our results with the ones in the cited works.

6.1 Introducing disorder

As in chapter 5, the solutions to the background equations of motion are characterised by two parameters, the chemical potential μ and the mass m. There, we chose a spatially varying step-like mass profile $m(x)$ while the chemical potential was kept constant. In this case, we work with a constant mass and a spatially varying chemical potential μ which contains the disorder. So as to mimic the random on-site potential use by Anderson in [106], we introduce a chemical potential of the form used in [28]

$$\mu(x) = \mu_0 + \frac{\mu_0}{25}\, w \sum_{k=k_0}^{k_*} \cos(k\, x + \delta_k)\,, \tag{6.1.1}$$

with δ_k being a random phase for each wave number k, and w a parameter that determines the strength of the disorder. The factor of $1/25$ is chosen for convenience to guarantee that the noise oscillates moderately around the mean value μ_0. In the limit of a large number of modes a noise of this form tends to a Gaussian distributed random function [28]. In figure 6.1 we show different realizations of (6.1.1) for different choices of k_* and w. Broadly speaking, the disorder strength w regulates the amplitude of the noise, whereas the number of modes in the sum, given by k_*, somewhat determines how smooth the noise is. Note though, that both parameters have an influence upon the final form of the noise.
As pointed out in [28], this choice of the noise corresponds to a low correlation, which from a condensed matter perspective is more realistic. In particular the correlation function of (6.1.1) is given by

$$\langle \mu(x)\mu(0)\rangle - \mu_0^2 = \sum_{k=k_0}^{k_*} \cos(kx) = \mathrm{Re}\,\left(e^{ik_0 x} \frac{e^{i(k_*-k_0+1)x}-1}{e^{ix}-1} \right), \tag{6.1.2}$$

so the correlation length can be seen to be inversely proportional to the number of modes included in the sum in (6.1.1), which is determined by k_*.

As opposed to the situation in the previous chapter, nothing prevents us here from using periodic boundary conditions along the x direction. Indeed this possibility is already suggested by the form of (6.1.1). So in the discrete grid of collocation points in that direction, the wave numbers k take values

$$k_n = \frac{2\pi}{L_x}(n+1) \quad \text{with} \quad 0 \leq n < N_x - 2 = \frac{k_*}{k_0}, \tag{6.1.3}$$

where the upper limit of $N_x - 1$ is explained by the fact that the N_x^{th} grid point is actually equivalent to the 1^{st} one by virtue of the periodic boundary condition. k_0 is the minimum wavenumber and k_* the maximum wavenumber at which we truncate the sum. k_* can be at most the so-called Nyquist limit, which signals half the highest frequency that can be reconstructed from a given sample, namely, that at which aliasing sets in. In our case, this limit is given by

$$k_{Nyquist} = \frac{\pi}{L_x}(N_x - 1), \tag{6.1.4}$$

Henceforth we characterise the noise by the choice of w and of κ, by which the fraction of $k_{Niquist}$ in k_* is meant

$$\kappa = \frac{k_*}{k_{Nyquist}}. \tag{6.1.5}$$

Again, as explained in section 5.1.1, we will restrict ourselves to the region of the diagram 3.6 corresponding to the black hole embeddings. Furthermore, the massless case is treated separately given the additional simplicity it offers.

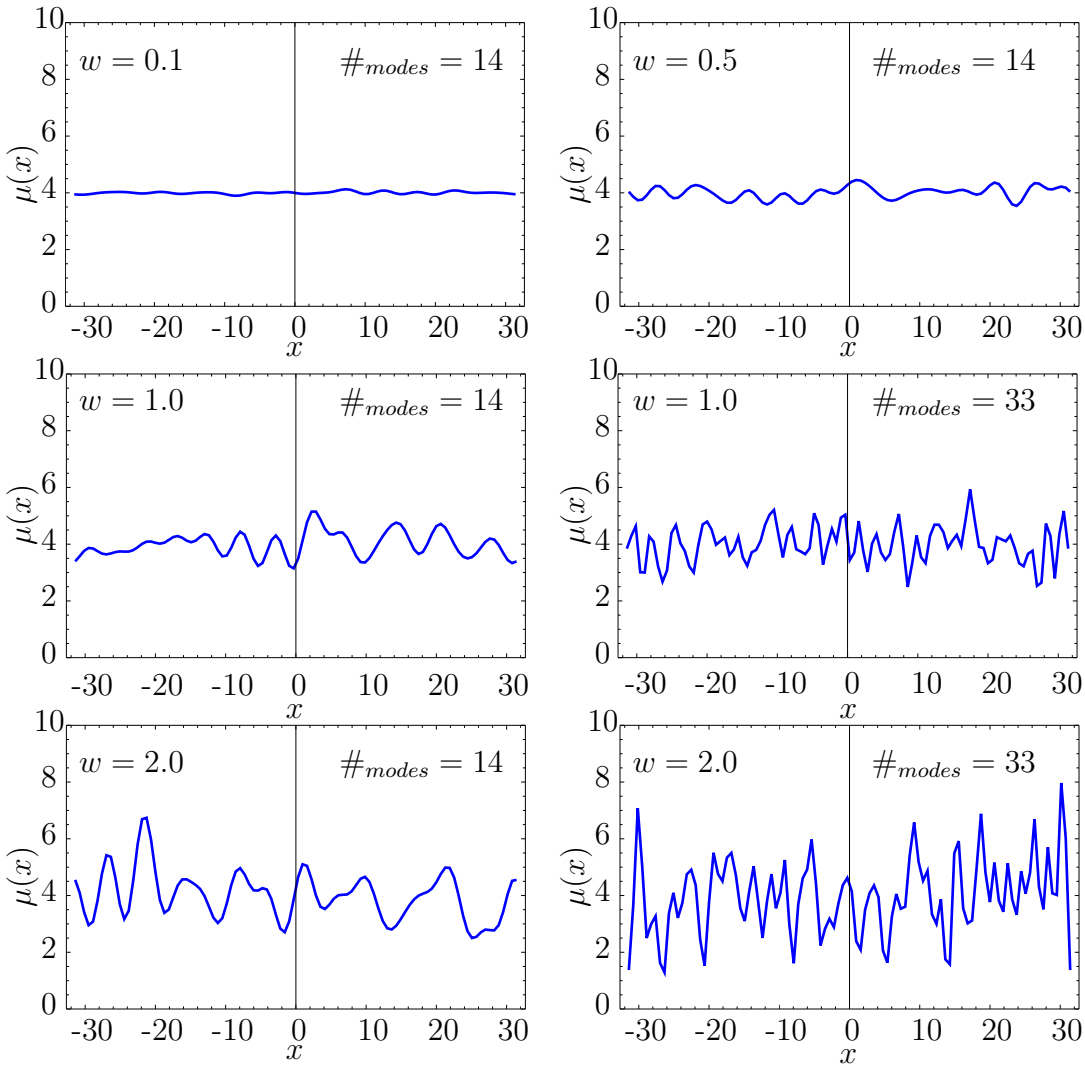

Figure 6.1: Different realizations of the noise (6.1.1) for a mean value $\mu_0 = 4$ and a system of spatial length $L_x = 20\pi$ discretised on a grid of 100 evenly spaced collocation points with different combinations of the parameters w and number of modes. The maximum number of modes allowed according to (6.1.4) is 48.

If $m = 0$, $\chi(z, x) = 0$ is a solution and only one equation of motion, that for the gauge field ϕ has to be solved. Then (B.0.1) reduces to

$$z^3 \left[\dot{\phi}^2 \left(\phi' \left(3zh' - 4h\right) + 2hz\phi''\right) - 4hz\dot{\phi}\phi'\dot{\phi}' + 2h\left(\phi'\right)^2 \left(z\ddot{\phi} + \phi'\left(zh' - 2h\right)\right)\right] - f^2\left(2\ddot{\phi} + 3h'\phi' + 2h\phi''\right) + 2fhf'\phi' = 0. \tag{6.1.6}$$

6.2 Numerics

Once it comes to the numerical resolution of the system, we proceed very similarly as in section 5.2, that is applying the numerical techniques developed in chapter 4. Again, the choice of the boundary conditions is what dictates what kind of system is being solved. This time we choose a constant mass and an inhomogeneous chemical potential that accounts for disorder, so at the boundary we impose in accordance with (5.1.11) and the noise in (6.1.1)

$$\chi'(0, x) = M\,, \qquad \phi(0, x) = \mu_0 + \frac{\mu_0}{25}\, w \sum_{k=k_0}^{k_*} \cos(k\, x + \delta_k)\,, \tag{6.2.1}$$

with M being the homogeneous mass of the embedding and μ_0 the mean value of the chemical potential. As for the black hole horizon, the requirements are the same as in chapter 5, namely

$$\phi(1, x) = 0\,, \qquad \chi'(1, x) = 0\,, \tag{6.2.2}$$

as imposed by regularity and the equations of motion themselves. Regarding the spatial boundaries, as we mentioned before, the geometry now does allow the use of periodic boundary conditions in the x direction and we choose indeed to use them. Thereby, the geometry of our space is effectively that of a cylinder of length L. The technical implementation of this change is straightforward, as shown in 4.4.2. A notable difference though, is the different choice of the grid of points. While in chapter 5 we used a grid of Chebysehv points both in the radial and in the boundary direction in this case we will only use a Chebyshev grid along the radial direction and use a standard grid of evenly spaced points in the x direction for the reasons explained in chapter 4.
All in all, we use Mathematica to discretise space-time in the (z, x)-plane on a mixed grid of 50 Chebyshev collocation points in the z direction and 100 evenly spaced points in the x direction. For the resolution of the set of non-linear algebraic equations of motion (B.0.1) and (B.0.2) we resort to our implementation of the Newton-Raphson algorithm once again. As in chapter 5, we define the variations of the fields $f = (\chi, \phi)$ in each iteration as δf and consider the accuracy of our solution to be given by Max $|\delta f|$. We work to an accuracy defined this way of 10^{-12}.

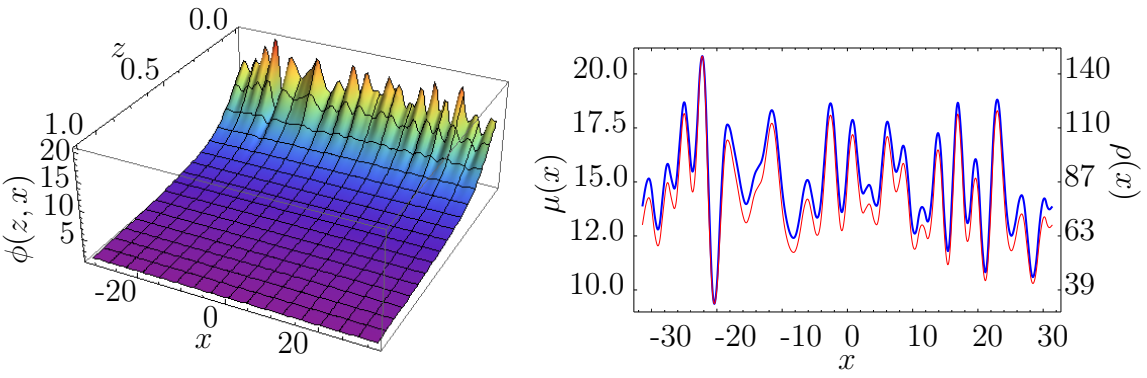

Figure 6.2: The solution of a massless background with $\mu = 15$ is shown on the left. Note that for the massless case the χ field is trivial. On the right side we show in blue the profile of the chemical potential $\mu(x)$ introduced as a boundary condition according to (6.2.1) and the resulting charge density read out by means of (6.3.1) in red.

In order to find solutions to the noisy system, we employ the technique described in chapter 4 based in first solving the homogeneous system and taking its solution as a departing point to find the non-homogeneous solution. Recall that in the massless case, we need only worry about a single equation of motion (6.1.6).

6.3 Background solution and charge density

Once the numerical framework is set, we may proceed to solve our system for the background fields χ and ϕ in the presence of a noisy chemical potential. As long as we concentrate on the massless case, the χ field has a trivial solution and it suffices to solve equation (6.1.6) for the gauge field. In figure 6.2 we show the solution obtained for the massless case with a chemical potential $\mu = 15$ and a noise characterised by $w = 1$ and $\kappa = 0.5$. After solving the background we analyse the behaviour of the charge density in the presence of the disorder and compare it to the clean homogeneous case. The read out of the charge density is done straightforwardly using again

$$\rho(x) = -\partial_z \phi|_{z=0} \,. \tag{6.3.1}$$

We compare the mean value of the charge density in the system with disorder to that of the system without disorder and see how the former is enhanced with respect to the latter in the sense that

$$\langle \rho(x) \rangle \; > \; \rho_0, \tag{6.3.2}$$

ρ_0 being the charge density computed for an homogeneous system with a clean chemical potential μ_0 in the absence of disorder. This means that, even though

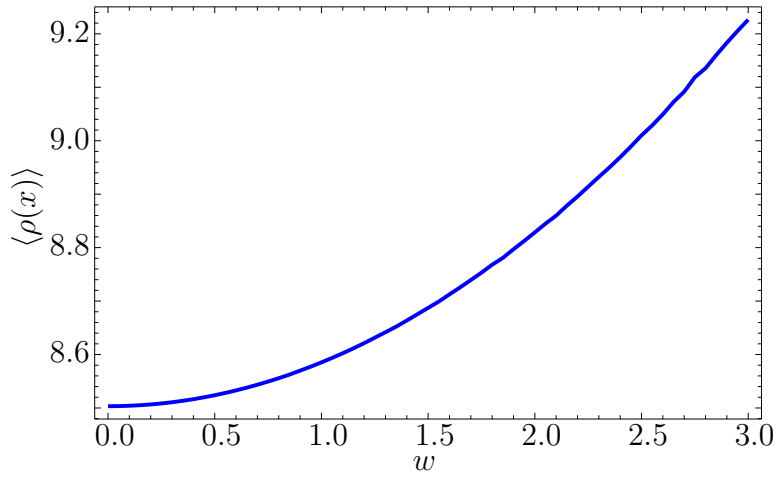

Figure 6.3: Evaluation of the mean charge density along the x direction for massless backgrounds with $\mu = 4$ and a noise characterised by a fixed number of modes given by $\kappa = 0.5$ and a varying noise strength w. It is clear how the mean value of the charge density increases quadratically with w.

the charge density locally decreases below the mean value at some points, at other points it is beyond this value and the balance is such that the overall effect is a positive growth of the charge density. Note that this is in spite of the noise not altering the mean value of the chemical potential. The increase in the charge density is observed for all values of the mean chemical potential μ_0. Thus we can state that the presence of the impurities in the chemical potential leads to an increase in the average charge density in the system. This was already seen and discussed in the context of holographic superconductors in [27, 28]. This enhancement of the charge density referred to the clean case increases quadratically with the noise strength w as shown in figure 6.3. This could have been foreseen in view of equations (5.3.3) and (6.1.1) since

$$\rho(x) \propto \mu(x)^2 \propto \left(\mu_0 + \frac{\mu_0}{25}\, w \sum_{k=k_0}^{k_*} \cos(k\,x + \delta_k)\right)^2, \tag{6.3.3}$$

hence when taking the mean value we find

$$\begin{aligned}\langle\rho(x)\rangle &\propto \left\langle \left(\mu_0 + \frac{\mu_0}{25}\, w \sum_{k=k_0}^{k_*} \cos(k\,x + \delta_k)\right)^2 \right\rangle \\ &\propto \mu_0^2 + 2\,\frac{\mu_0^2}{25} w \underbrace{\left\langle \sum_{k=k_0}^{k_*} \cos(k\,x + \delta_k) \right\rangle}_{0} + \frac{\mu_0 w^2}{25^2} \underbrace{\left\langle \left(\sum_{k=k_0}^{k_*} \cos(k\,x + \delta_k) \right)^2 \right\rangle}_{\text{constant}>0},\end{aligned} \tag{6.3.4}$$

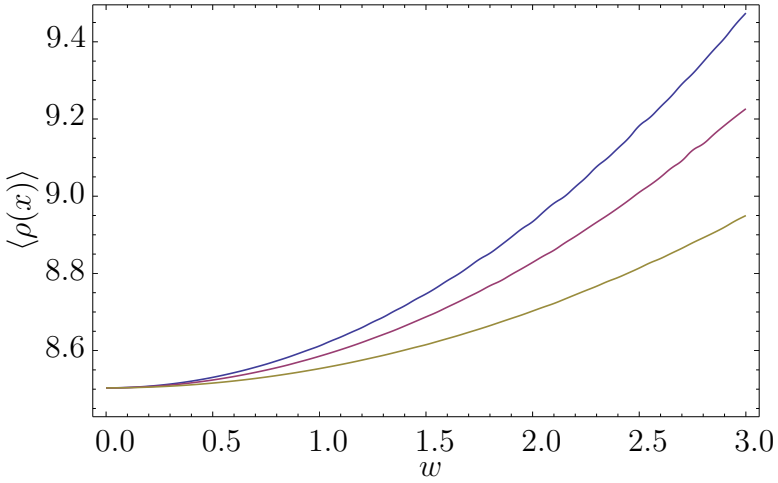

Figure 6.4: Same evaluation as in figure 6.3 but comparing the case of different values of κ. In ascending order from the bottom we have $\kappa = 0.3, 0.5, 0.7$. We see how for a given w, a bigger number of modes in the sum in (6.1.1) leads to a bigger enhancement of the charge density.

where $\langle\rho(x)\rangle$ is the mean value of the charge density averaged over the spatial interval[1]. In the last row we have made used of the fact that, since we are integrating over whole periods of the cosinus present in the sum, the second term in the last line of the equation vanishes whereas the last term is a constant dependent on the particular choice of κ. Thus this confirms our observations based on figure 6.3 that indeed

$$\langle\rho(x)\rangle \propto w^2. \tag{6.3.5}$$

Moreover, the enhancement of the charge density by the impurities also increases with the number of modes included in the sum in (6.1.1), signalled by κ for a given w, as can be seen in figure 6.4. This is understood from a qualitative perspective in the light of figure 6.1. A higher number of modes in the sum endows the disorder with a peakier structure, thereby increasing the effect that spatial derivatives play in the corresponding equations of motion. This effect is clearly a net enhancement of the charge density.

Let us now analyse the results obtained in the presence of mass. To see what the effects of the mass are upon the different quantities we compare the massless case in figure 6.2 to backgrounds with the same chemical potential, $\mu = 15$ and finite values of the mass. In figure 6.5 we show for example the solution obtained for $M = 5$ as well as the chemical potential introduced in the system and the resulting charge density distribution. The characterising parameters

[1]Note that in the computations of averages the last or the first point in the grid is excluded, since it is respectively equivalent to the first or last point by virtue of the periodic boundary condition.

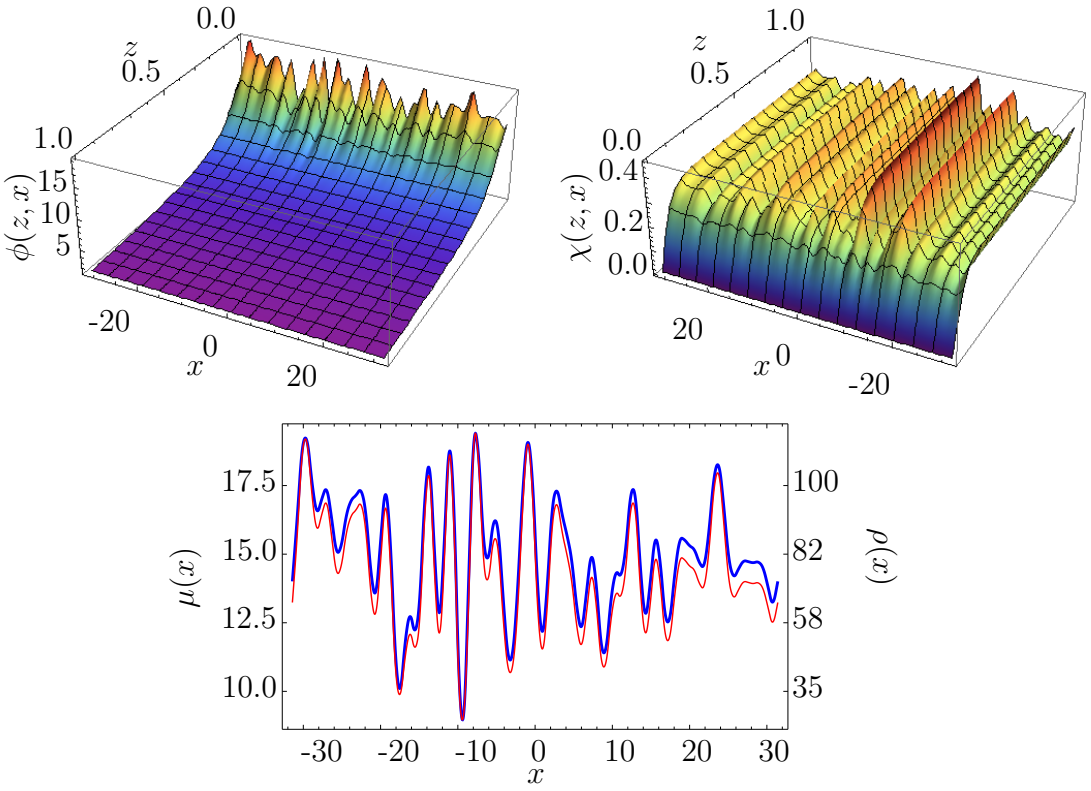

Figure 6.5: Solution for a massive background with $\mu_0 = 15$ and $M = 5$ with a disorder induced by a noise characterised by $w = 1.0$ and $\kappa = 0.5$. Note that the axes of the two top figures are inverted with respect to one another. The ϕ field is shown on the left and the χ field on the right. The bottom figure shows the exact chemical potential profile $\mu(x)$ introduced in blue and the resulting charge density $\rho(x)$ in red. Compare in particular the resulting charge density to the one in figure 6.2.

of the disorder are $\kappa = 0.5$ and $w = 1.0$. Upon comparing the results obtained for the massless case to the ones obtained in the presence of mass we found that no interesting characteristic effects are triggered in the massive case. The numerical values in the plots just reflect the different values of the charge density obtained in massive embeddings but no qualitative new physics is observed that can be attributed to the presence of mass in the system.

All in all, we see how the presence of disorder induces a net enhancement of the charge density, in the sense that its value averaged over the entire spatial range is bigger than the value of the charge density in the clean system without disorder. This enhancement increases quadratically with the noise strength w and also with the number of modes given by the parameter κ.

6.4 Solution of the fluctuations and conductivities

Once we have solved the background fields ϕ and χ we extend our analysis to their fluctuations the same way we did in the previous chapter in order to analyse the response of the system to an applied electric field, namely its electrical conductivity. We proceed exactly as in chapter 5. In particular equations (5.4.1) to (5.4.37) are as valid here as they were there. Our definition of the electrical conductivity is still given by (5.4.2).

The equations of motion for the fluctuation fields a_t, a_x, c and a_y are solved numerically on the same grid used for the computation of the background fields. We continue to make use of periodic boundary conditions for all fields. As to the boundary conditions along the radial direction, near the black hole horizon we proceed as in the previous chapters and impose the in-falling wave condition so as to preserve causality there. Hence the ansatz (3.5.12) is taken, which leads to the expressions (5.4.9). Again, we render the calculations with such boundary conditions simpler by redefining the fluctuation fields according to (5.4.10). Thus the conditions in (5.4.11) and we must bear this redefinition in mind to undo it when it comes to extracting quantities such as the conductivity.
Furthermore, we can still make use of the integral form of the expression for the DC conductivity in the direction transverse to the disorder (5.4.32) to read this quantity from near-horizon background data without having to compute the corresponding fluctuations. This notably simplifies the study of the effects of the disorder upon the conductivity in the low frequency limit.

As in the case of the charge density, we may study the changes in the behaviour of the conductivities due to the presence of the disorder by comparing its mean value to the value obtained for the corresponding clean case, that is without disorder. We first analyse the evolution of the DC conductivity when the chemical potential, the charge density and the noise strength w are modified. In the light of our results we can test the predictions formulated in [32], according the which the disorder in the charge density increases the conductivity at high temperature and is suppressed as the temperature goes down. Note that in our case the disorder is directly introduced into the chemical potential but is also reflected in the charge density. Moreover, from our analysis of the relationship between the conductivity and the charge density, we can also compare our results to the ones analysed from a condensed matter theory perspective in [35, 36].
We do not analyse in detail the conductivity in the direction parallel to the disorder σ_y, for no interesting patterns are induced on it by the presence of the noise besides the expected enhancement to the increase in the charge density. Again, we mainly focus on the study of the technically less involved massless

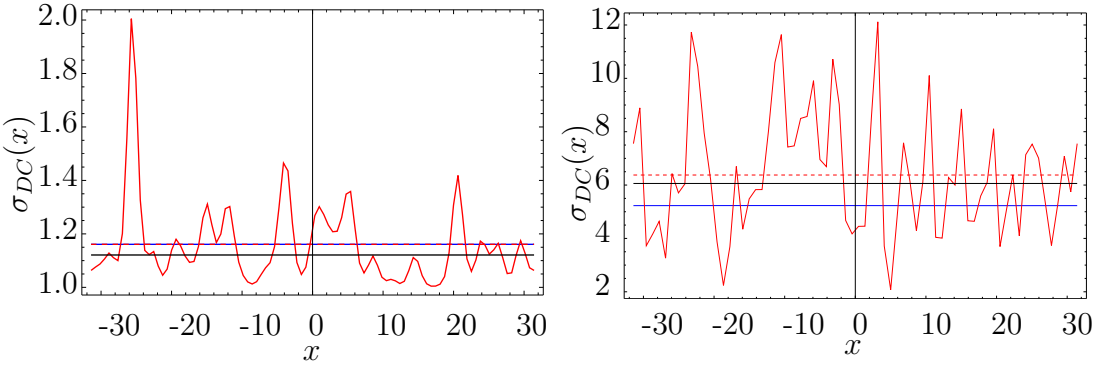

Figure 6.6: Computed conductivities for two massless backgrounds in which the different effect of the disorder upon σ_x^{DC} is shown. The black line shows the DC conductivity of the corresponding clean system σ_0^{DC}. The DC conductivity in the y direction, σ_y^{DC}, is shown in red and the dashed red line signals its mean value. The blue line stands for the constant DC conductivity in the x direction, σ_x^{DC}. On the left we plot a background with $\mu = 0.7$ and a noise characterised by $w = 5$ and $\kappa = 0.5$. The noise must be made stronger than elsewhere to make its effects more visible. Both σ_x^{DC} and σ_y^{DC} are over σ_0^{DC}. On the right we show the situation for $\mu = 5$. Here σ_x^{DC} is clearly suppressed with respect to σ_0^{DC}.

case to observe the effects the disorder has upon the conductivity and then proceed to analyse the massive case, so that we can appreciate how the presence of mass affects the results.
Our analysis of the conductivities does not extend to the AC conductivities, for we have no interesting results to report in these regards. The randomly disordered chemical potential is seen to affect only the low-frequency behaviour of the conductivities. This is consistent with the supposition that the extended disorder introduced by the noise be only noticed in the low-frequency regime when long distance scales are probed.

6.4.1 Effects of charged disorder upon the DC conductivity

The DC conductivity in the direction of the disorder, σ_x^{DC} can be extracted from the IR background data via equation (5.4.35). For information about the DC conductivity in the direction transverse to the disorder, σ_y^{DC}, the resolution of the corresponding equation of motion for the fluctuation field a_y is necessary. From this computations we find that the qualitative effect of the disorder upon the DC conductivities depends on the value of the chemical potential μ. Examples are provided in figure 6.6 for values of the chemical potential of $\mu = 0.7$ and $\mu = 5$. The disorder always enhances the charge density and the DC conductivity in the y direction compared to the clean homogeneous case. Instead the DC conductivity in the x-direction is suppressed in the first case and enhanced in the second example.

We understand this as a competition between the effect of the enhanced charge density on the one side, which lets the conductivities tend to increase and the direct effects of the gradients in x upon the conductivities. This competition was also analysed in chapter 5, see figure 5.11. When the value of the chemical potential is low, the enhancement of the charge density seems to be the dominant effect. The fact that σ_x^{DC} takes the same value as $\langle\sigma_y^{DC}\rangle$ reinforces this interpretation. Both conductivities are just feeling the enhancement in the charge density and hence are equally increased from their equal values in the clean homogeneous embedding. At bigger values of the chemical potential the direct effects of the gradients seem to overtake the dominant role and lead to a suppression of σ_x^{DC}.

The analysis may be extended to a whole range of values of the chemical potential. Recalling that, according to (3.4.43)

$$\frac{1}{\mu} \propto T, \tag{6.4.1}$$

this analysis may be performed sweeping over different values of μ and directly compared to the evolution of the DC conductivity with the temperature predicted in [32]. Our results are displayed in figure 6.7. As it can be seen there, the presence of the noise affects the low-temperature behaviour of the DC conductivity in the x-direction, notably suppressing it with respect to the clean case with no disorder. The suppression furthermore increases with the strength of the disorder w, as can be visualised in the right panel of figure 6.9. This results are physically understood as the disorder causing the charge carriers trouble to move within the conducting medium. The spatial gradients difficult the transport of charge and hence the conductivity.
At higher temperatures, we find a range of values of the chemical potential, μ, in which the DC conductivity in the x-direction is over the conductivity of the clean case. This is more difficult to see, for the numerical differences with respect to the clean case are small. The effect can be made stronger and hence more visible by increasing the strength of disorder. The corresponding values are consistently above the homogeneous clean ones and a monotonous growth in this enhancement can be observed when the strength of disorder w is increased. This excludes the possibility that it be due to numerical effects. The situation is illustrated in the left panel of figure 6.9. In the light of this we can state that there is a range of μ for which the net effect upon the DC conductivity is an enhancement with respect to the clean case. This is also illustrated in figure 6.8, which is equivalent to figure 6.7 but for a stronger noise. The range of the plot is furthermore cut so that the region at which the crossover from the enhanced to the suppressed conductivity be clearly seen.
These results may be compared to the discussion in [32]. There the prediction is formulated, that the DC conductivity should be suppressed with respect to the clean case below a given temperature while it ought to increase beyond that temperature. We confirm this expectation in the light of our numerical

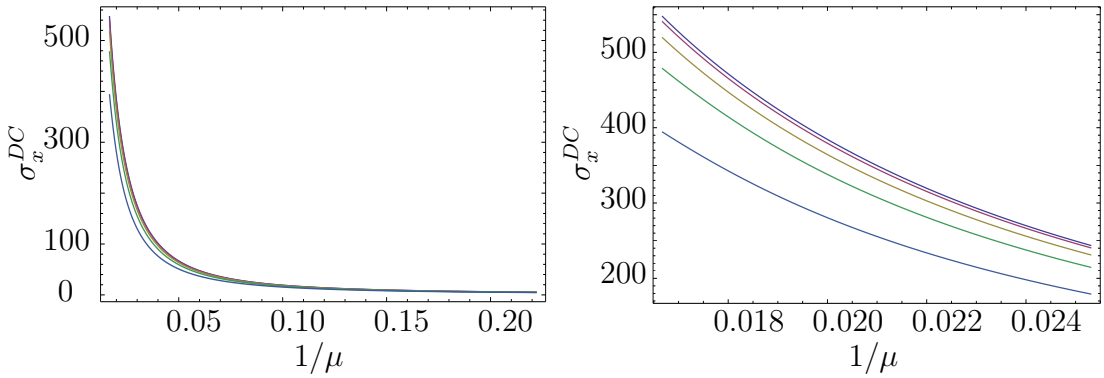

Figure 6.7: Evolution of the σ_{DC} in the x-direction computed for a massless background with $1/\mu$ with a noise characterised by $\kappa = 0.5$. The different lines stand for different values of the parameter w. The uppermost line is the clean case with no noise. The subsequent lines illustrate the cases in which $w = 0.5, 1, 1.5, 2$. The plot on the right shows the zoomed-in region of the plot on the left corresponding to low values of $1/\mu$.

results. Nevertheless we do not observe the expected suppression of the DC conductivity in the direction of the disorder all the way down to 1. Also, we observe that in the limit of very small chemical potentials both the clean and the noisy case overlap and take the standard value 1, which is explained by the effective absence of charge density in this case.

It is worth pointing out that in the mentioned reference impurities are holographically introduced as a static randomness with the important difference with respect to our case that they are placed at the horizon, not at the boundary as we do. This has the advantage of offering direct access to the energy scale at which the effects of the noise are most noticed whereas our approach provides more control over the physical meaning of the physical quantities in the dual field theory in which the disorder is introduced, in this case the chemical potential. We might be though paying the price of a smaller effect of the noise upon the physical quantities in the low-energy scale like the DC conductivity or in other words, stronger noises are required for their effects to be noticed in the low-energy regime.

6.4.2 DC conductivity as a function of the charge density

We also analyse the parallel progression of the charge density ρ and the DC conductivity, σ_{DC}. As shown in figure 6.10, we observe a linear relationship between both quantities with a proportionality coefficient or slope that is inversely proportional to the number of modes included in the sum in (6.1.1), given by κ (see (6.1.5)). The analysis of this progression was inspired by the models in [35, 36] about the conductivity of graphene in the presence of impurities. The linear relationship was also found there. This linearity is maintained

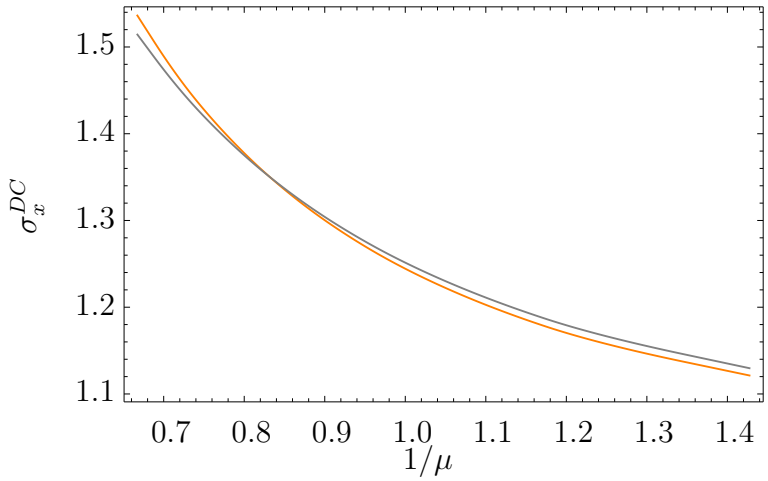

Figure 6.8: Evolution of the σ_{DC} in the x-direction computed for a massless background with $1/\mu$ with a noise characterised by $\kappa = 0.5$ and $w = 2.5$. The orange line shows the clean homogeneous case with no disorder. The grey line stands for the conductivity in the presence of the disorder. The range of the plot is furthermore cut so that the region at which the crossover from the enhanced to the suppressed conductivity be clearly seen.

over the whole range of charge densities in the clean case. As more and more modes are included in the sum in (6.1.1), that is as κ is increased, the setting in of sublinear behaviour can be observed at high charge densities, which becomes more manifest for bigger values of κ.
The linearity relation between the conductivity and the charge density, namely the density of charge carriers, was also found from the condensed matter theory models in [35, 36]. The apparition of sublinear behaviour at high charge densities was also predicted in the cited works and the observation that it ought to be more noticeable when the concentration of impurities is bigger is in agreement with our result that this sublinear behaviour becomes more and more manifest for a higher number of modes in the noise. As we saw at the beginning of this chapter, a bigger number of modes leads to a peakier spatially dependent chemical potential and can thus be assumed to reflect the situation in which more impurities are present in the material. Still, for the comparison with the cited references to be more precise, we should be comparing cases with just different correlation lengths. Changing the number of modes does not only imply a change in the correlation length but also in other properties of the disordered system as the variance. More detailed analysis along these lines is worth carrying out. Still, our results provide a first glance of agreement pointing in the right direction.

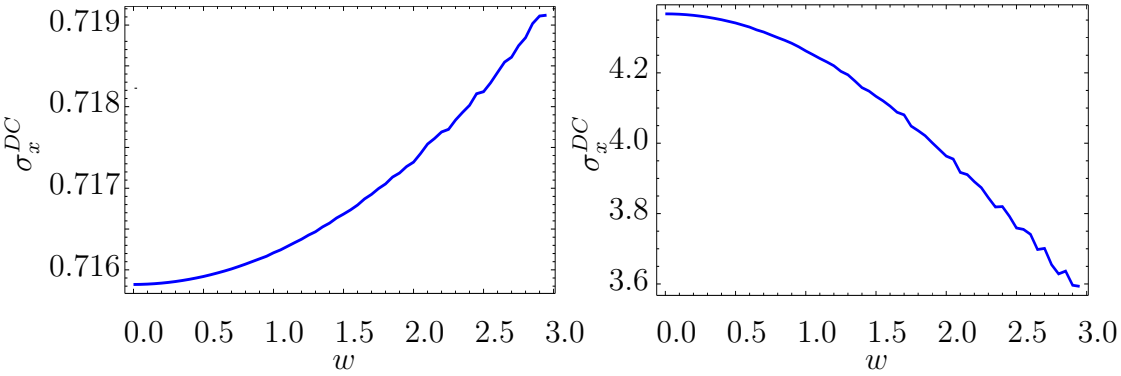

Figure 6.9: Evaluation of the DC conductivity along the x direction for massless backgrounds and a noise characterised by a fixed number of modes given by $\kappa = 0.5$ and a varying noise strength w. The figure in the left shows the case $\mu = 1$ and the case $\mu = 4$ is shown on the right.

6.5 Concluding remarks

In this chapter we have constructed a system that realises holographically a strongly coupled medium at finite temperature and finite density of fundamental particles acting as charge carriers in the presence of random disorder. The disorder is introduced in the chemical potential as a random fluctuation around a fixed mean value. This reproduces the situation in real materials in which the energy of the carge carriers has a disordered structure. Our main results are:

- We have solved the background fields in the presence of disorder and extracted from it the information about the charge density. We observe an increase in its mean value when compared to the homogeneous system in the absence of noise. The charge density undergoes a net enhancement induced by the presence of the disorder.

- We have numerically computed the conductivities of a probe brane system in the presence of disorder. We find that the DC conductivity in the direction transverse to the disorder is always enhanced by it. Instead in the direction of the disorder, the DC conductivity is enhanced for a given range of values of the chemical potential whereas it gets notably suppressed at higher chemical potentials, which in our case also means at lower temperatures. We furthermore observe that the enhancement or suppression of the conductivity is proportional to the strength of the disorder, characterised here by the parameter w.

- We have studied the relationship between the DC conductivity in the direction along which the disorder extends and the mean charge density of the system and found that they are linearly proportional to each other. The proportionality factor decreases as more modes are included in the spectrum of the noisy chemical potential. We also observe the setting

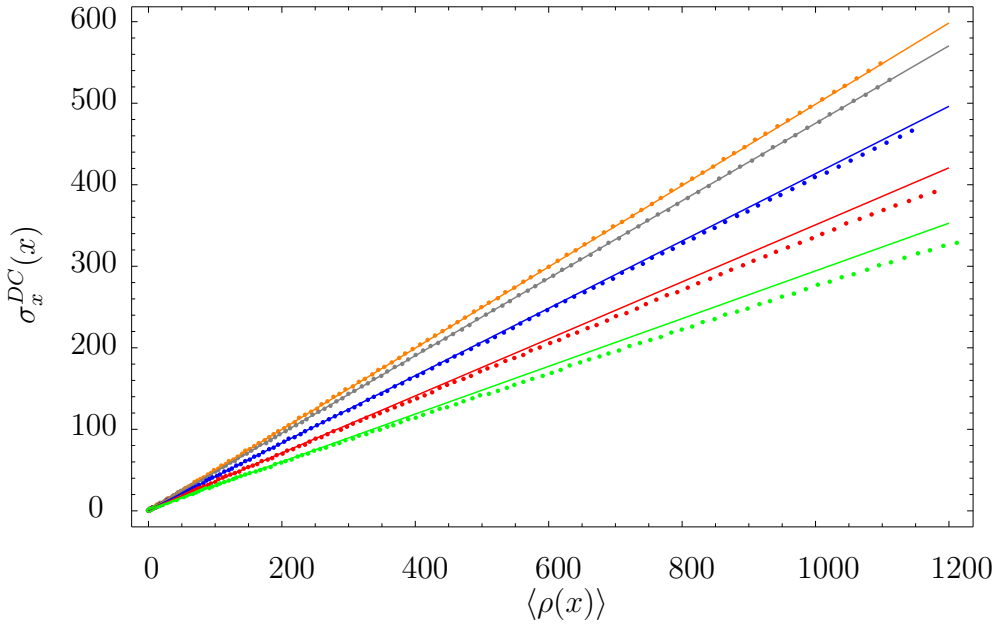

Figure 6.10: Evolution of the computed values of the σ_x^{DC} compared to the mean values obtained for the charge density $\rho(x)$. We plot both physical quantities in this way so as to enable the direct comparison with the figures in [36]. The orange points show the computed data for the clean case, that is in the absence of noise. The following sets of data points show in descending order the situation when disorder is introduced with $w = 2$ and $\kappa = 0.1, 0.3, 0.5, 0.7$. The solid lines show the linear fits corresponding to the data sets in the same colours. The line is fitted to the first 50 points of each data set, corresponding to those obtained for configurations with a chemical potential of up to $\mu = 24.5$. The linearity between σ_x^{DC} and $\langle\rho(x)\rangle$ is perfect in the clean case. The slope or linearity coefficient decreases with κ. The setting in of sublinear behaviour at higher value of κ is also manifest.

in of sublinear behaviour at high charge densities, which is more notable when more modes are included in the noise.

Chapter 7

Conclusion

In this thesis we use gauge/gravity duality and in particular the weak version of the AdS/CFT correspondence with a large number of colours $N \to \infty$ in the gauge theory and a large t'Hooft coupling $\lambda \gg 1$ to study phenomena related to the presence of inhomogeneities and noise in strongly coupled matter.
We are able to do so in spite of the complicated equations of motion arising thanks to the numerical techniques we present in chapter 4. Details on the codes employed are given in appendix D.

In chapter 5 we construct a holographic system that realises a (1+1)-dimensional charged interface in a strongly coupled medium at finite temperature and finite density of fundamental particles acting as charge carriers. We do it by means of a D5 flavour brane in the probe approximation having a step-like spatially dependent prifile.
From the numerical solutions of the background we obtain the data corresponding to the charge density profile. We check that this profile is indeed localised around the interface, being around five times larger there than at the spatial edges. The non-vanishing charge density at the spatial edges is due to our being in a black hole embedding but in principle this could be circumvented by getting closer and closer to the Minkowski embeddings.
The study of the fluctuation fields allows to compute the conductivities of the system. The analysis of their behaviour reveals agreement with broad expectations for a system with localised charge on a (1+1)-dimensional interface. The effects of the interface are mostly reflected in the low-frequency behaviour of the conductivities. In the direction of the defect, the conductivity is mainly determined by the local conditions at the interface. The DC conductivity increases its value with respect to the homogeneous case. This is likely to be a characteristic particular to strongly coupled systems, since it is induced by the form of the DBI action. In the direction transverse to the defect, the DC conductivity is influenced by the global conditions of the system and mostly determined by the properties of the system outside the interface. Its value therefore decreases with respect to the equivalent homogeneous case.

In chapter 6 we develop a system at finite temperature and finite density of fundamental particles that holographically accounts for impurities in the form of random disorder in the chemical potential. The system is a follow-up of the one in chapter 5 and also consists in the use of a D5 flavour brane in the probe approximation.
By numerically solving the background we extract information about the charge density of the system and about the effects the disorder has upon it. We observe a net enhancement in the charge density induced by the presence of the impurities. This enhancement increases quadratically with the strength of the disorder.
From the analysis of the fluctuations we obtain information about the conductivities of the system and the changes in their behaviour due to the disorder. Our analysis reveals that the DC conductivity in the direction along which the disorder extends is enhanced by the disorder within a given range of temperatures and is notably suppressed at lower temperatures. We furthermore find that said suppression increases quadratically with the strength of disorder. In the direction transverse to the disorder, the conductivity is always enhanced by the disorder. Our results along these lines are a confirmation of the predictions formulated theoretically by means of the AdS/CFT correspondence applied to systems of probe D-branes in [32].
We also analyse the relationship between the DC conductivity in the direction along which the disorder extends and the mean charge density of the system and find linearity. The coefficient of linearity decreases as the disordered chemical potential acquires a rougher spatial structure. Moreover the disorder seems to lead to a sublinear behaviour at high charge densities. These results show qualitative agreement with predictions formulated within condensed matter theory models for the transport properties of graphene reproducing experimental data [35, 36].

In spite of the limitations introduced by the conditions under which the weak version of the duality works when it comes to relating our results to real world physics, underlying universalities might underpin our predictions. Such universalities have already been unveiled in other holographic studies and shall remain our best hope of a better comprehension of some of the phenomena in strongly coupled matter as long as gauge/gravity duality is not better understood beyond the limits of its weak version.

7.1 Outlook

The use of the AdS/CFT correspondence as a tool to explore the strongly coupled regime of matter in the presence of disorder provides many interesting directions of research. The projects pursued in this thesis have possible extensions and follow-ups, which would not be very difficult to implement once the numerical techniques we have covered are mastered.

For once, the inclusion of topological terms in the action would open the door to more detailed studies of the physics of topological insulators and the quantum Hall effect. This might be done using a D7 probe brane like in [25] but is also possible using a D5-brane, as shown in [26]. The addition of a magnetic field to the system may also lead to the activation of topological effects, as explored in [111]. Another interesting continuation of our work would be the use of a system with an interface like the one in chapter 5 to analyse the predicted fermionic nature of the massless degrees of freedom at the interface. This would require the consideration of fluctuation fields with spatial momentum.
The project presented in chapter 6 also leaves room for extensions. It would be by all means interesting to study how different realisations of the disorder affect the properties of the system. The noise could for example be introduced in the IR so as to make the connection to the predictions in [32] even more direct. Morevoer, the random fluctuations that mimic the impurities in real materials could also be introduced in the mass.

There are still plenty of phenomena in condensed matter physics awaiting a theoretical explanation. AdS/CFT shall continue to prove its solidity in these regards. With the unveiling of new universalities common to strongly coupled field theories, the domain of applicability of AdS/CFT and its predictive power could be enhanced. Besides providing a better understanding of the otherwise inaccessible strongly coupled regime of matter, studies like ours may be paving the way to a better command of the duality and hence maybe to an improved grasp of string theory.

Appendix A

Group theory, Lie algebras and highest weights.

Since the very beginning of this thesis, we have been stressing how relevant a role symmetry plays in theoretical physics. Most of the time symmetries are naturally dealt with by means of mathematical group theory. Group theory can be considered to be the mathematics of symmetries. In fact, the three key mathematical properties of any symmetry, namely associativity, the existence of an identity element and of the inverse element are precisely the three defining properties of a group.
Both space-time and most of the internal field spaces are considered to have a continuous and smooth character. This is why high energy physics is mostly concerned with symmetries supported on continuous and smooth spaces or manifolds. It being so, we shall be interested in groups that intrinsically reflect this fact. These groups are quite well known in mathematics and go under the name of Lie groups. Lie groups are formally defined as groups which depend continuously on one or more parameters. Our treatment of Lie groups and their representations here focuses on their applicability to gauge theories of trivial topology (i.e. without instantons or topological terms), thus we will concentrate on compact Lie groups, whose general treatment, due to Cartan, Weyl and Dynkin is well developed.
In chapter 3, we used the highest weight formalism to analyse the properties of irreducible representations of the little group, perform dimensional reductions and tensor products. Here, we wish to present the basics of this formalism to the unfamiliar reader. For more information on the topic, we refer to [112, 113, 114].

A group is generally defined in a broad sense accepting different embodiments in terms of matrices which adjust to the definition. Each of such embodiments, that is, each map from the group elements to a set of matrices acting on a q-dimensional vector space preserving the composition law of the group is called a **representation** of the group. From all possible representations there is one

deserving special attention. This is the representation in which the generators of the group are themselves seen as vectors and goes under the name of **adjoint representation**. It is spanned by the generators of the group and hence has dimension equal to the number of generators. Since we are dealing with compact symmetry groups, their representation can be assumed to be unitary. This implies that the corresponding generators can be taken to be hermitian. Now from the generators $T_1, \ldots, T_n$ we pick the maximal set of mutually commuting elements, $H_1, \ldots, H_m$

$$[H_i, H_j] = 0. \tag{A.0.1}$$

This is called the Cartan subalgebra and the H_i are the Cartan generators. A group with m mutually commuting Cartan generators is said to be of rank m. The m Cartan generators can be diagonalised at a time and their eigenvectors span the whole vector space. This means that we may assign a set of m eigenvalues or **weights**, h_i, to each state in the vector space

$$H_i \left|h_i\right\rangle = h_i \left|h_i\right\rangle \tag{A.0.2}$$

Each vector in the space is simultaneously an eigenstate of the m Cartan generators. When referring to the adjoint representation, weights are commonly called **roots**, which we shall denote by α_i. Thus the m-component vector of roots specifies the state uniquely. Actually this is so as long as the eigenstates are non-degenerate, but this is proven by the fundamental theorem of Cartan. Since the generators form an algebra, they satisfy the Jacobi identity. The non-Cartan generators $T_{m+1}, \ldots, T_n$ can be linearly combined into a new set $E_{m+1}, \ldots, E_n$ that satisfies

$$[H_i, E_j] = \alpha_j E_j, \tag{A.0.3}$$

which suffices to assert that the E_i can be interpreted as ladder operators

$$HE \left|h\right\rangle = ([H, E] + EH) \left|h\right\rangle = E\alpha \left|h\right\rangle + Eh \left|h\right\rangle = (\alpha + h)E \left|h\right\rangle . \tag{A.0.4}$$

Note in particular that since the E_i are not hermitian

$$[H_i, E_j^\dagger] = -\alpha_j E_j^\dagger. \tag{A.0.5}$$

If the representation is finite, there must be a state in the group which is annihilated by all step operators. That state is characterised by the highest weight. Thus once the highest weight is known, all other weights may be found by laddering down using the set of E_i.

Let us recap and illustrate with an example what has been said this far with an example. If we consider an n-dimensional representation of the rank-l Lie algebra G, then the Cartan generators H_i with $i = 1, \ldots, l$ are $n \times n$ diagonal matrices with diagonal elements μ_i^a for $a = 1, \ldots, n$. Such matrices live in the

space of n-dimensional vectors, spanned by the basis $e_1, \ldots, e_n$, hence we can express the matrix form of composing by H_i by columns

$$H_i = \mu_i^a e_a, \tag{A.0.6}$$

for any H_i. Now there will be n l-vectors $|h_i\rangle$ with components $(\mu_i^1, \ldots, \mu_i^n)$ and we have

$$H_i |h_i\rangle = \mu_i^a |h_i\rangle \equiv h_i^a |h_i\rangle . \tag{A.0.7}$$

Let us see an example. Take the 3-dimensional representation of $SU(3)$. The corresponding algebra has rank 2, so there are 2 Cartan generators

$$H_1 = \begin{pmatrix} 1 & 0 & 0 \\ 0 & 1 & 0 \\ 0 & 0 & -2 \end{pmatrix}, \qquad H_2 = \begin{pmatrix} 1 & 0 & 0 \\ 0 & 0 & 0 \\ 0 & 0 & -1 \end{pmatrix}. \tag{A.0.8}$$

In this case the states $|h_i\rangle$ are labelled by $\{(1,1),(1,0),(-2,-1)\}$.

There are some important definitions we have to make us of. Given a set of roots α_i, **positive roots** are defined as those whose first non-vanishing element is positive. In the example above, $(1,1)$ and $(1,0)$ are positive roots. **Simple roots** are those positive roots that cannot be expressed as a sum of other positive roots with positive coefficients. In the example, both positive roots are also simple roots. It is known (see [114] Chapter 8) that the number of simple roots equals the rank of the Lie algebra. Simple roots form a basis of the Cartan subalgebra. If the simple roots are known, all other roots can be expressed as sums of the simple roots. Lie algebras are uniquely defined by their simple roots.

A method of presenting all the relevant information about a Lie algebra is the use of the so-called Cartan matrix A, which is defined with components A_{ij} as follows

$$A_{ij} = \frac{2\langle \alpha_i, \alpha_j \rangle}{\langle \alpha_j, \alpha_j \rangle}, \tag{A.0.9}$$

where right angle brackets signal the common form of the dot product and the *alpha*s included in the equation are meant to be the simple roots. With this, we can go on to define the **coroots** as

$$\alpha_i^* = \frac{2}{\langle \alpha_i, \alpha_i \rangle} \alpha_i, \tag{A.0.10}$$

in terms of which any dual vector h can be written

$$h = \sum_i \bar{h}_i \alpha_i^*. \tag{A.0.11}$$

With these, we introduce the Dynkin basis, in which the components of h are

$$a_i = \sum_j \bar{h}_j A_{ji}, \tag{A.0.12}$$

with A being the Cartan matrix. The a_i are known as **Dynkin coefficients** or **Dynkin labels**. This basis owes ots importance to a theorem also by Dynkin stating that in the Dynkin basis the simple roots α_i are given by the i^{th} row of the Cartan matrix, hence having integer components. A further theorem by Dynkin says that an irreducible representation is identified by its highest weight, which can be expressed such that its Dynkin labels are non-negative integers. Hence an irreducible representation is characterised by its highest weight, which is commonly represented by a vector $[a_1, \ldots, a_m]$ showing its Dynkin coefficients.

Up to this point, this appendix has been brief compendium of the great work done by Dynkin classifying semi-simple Lie algebras and producing valuable theorems about them. Our aim is to make clear what we are referring to and to make further references possible.We use the above as a set of useful techniques but formal proofs of any of the claims made here are available. Any of the cited sources contains better and more detailed coverings of the topic. Yet on behalf of self-consistency, we wanted to offer the reader a review in case it is required to follow our presentation of the supergravity theories in chapter 3.

A.1 Dynkin labels in supergravity

Highest weights are additive, this means that given a representation Λ with highest weight λ and a representation T with highest weight τ, the highest weight of the representation $\Lambda \otimes T$ is $\lambda + \tau$. This together with the knowledge about the dimension of the representations of a group provides enough information to find the correct tensor product decompositions and dimensional reductions in chapter 3. There we deal with the little group for massless states in d space-time dimensions, which is the special orthogonal group $SO(d-2)$. In the following we present a table with the representations of $SO(d-2)$ used in physics and their dimensions, according to which the fields of supergravity are classified.

Highest weight	*physical name*	*dimension*
$[0, \ldots\ldots, 0]$	scalar	1
$[1, \ldots\ldots, 0]$	vector	d-2
$[0, ..., \underset{k^{th}}{1}, ..., 0]$	k^{th} antisymmetric (k-form)	$\binom{d-2}{k}$
$[0, \ldots\ldots, 1]$	spinor	$2^{\frac{d-3}{2}}$
$[2, \ldots\ldots, 0]$	2^{nd} symmetric traceless (metric)	$\binom{d-1}{2} - 1$
$[1, \ldots\ldots, 1]$	vector and spinor (gravitino)	$(d-3)2^{\frac{d-3}{2}}$

where it is important to note that as to the spinorial representations, it makes a difference whether d is even or odd. See any of the cited references for more on this.
Of course the dimension of each of the representations, that is its number of states, can be computed formally by making use of the corresponding ladder operators or of the known resulting formulae. What we show here is a compendium of the ones which are relevant to us. With this piece of knowledge at hand, it is possible for example to derive the dimensional reduction 3.1.2. We find the reduction of the gravitino indirectly. Recall it has $(d-3)\cdot 2^{\frac{d-3}{2}}$ degrees of freedom in p+11 dimensions. Since degrees of freedom are not suppressed when dimensionally reducing, they must be the same before and after the reduction. This helps finding the correct decompositions.

$$[1,0,0,0]_9 \longrightarrow [1,0,0,0]_8 + [0,0,0,0]_8$$
$$[0,0,0,1]_9 \longrightarrow [0,0,1,0]_8 + [0,0,0,1]_8$$

Knowing

$$\begin{array}{ccccccc} [1,0,0,0]_9 & \otimes & [0,0,0,1]_9 & = & [1,0,0,1]_9 & + & [0,0,0,1]_9 \\ 9 & \times & 16 & = & 128 & + & 16 \end{array}$$

and looking at the tensor product of the decomposition

$$([1,0,0,0]_8 + [0,0,0,0]_8) \otimes ([0,0,1,0]_8 + [0,0,0,1]_8) =$$
$$\mathrm{Decomp}([[1,0,0,1]_9]) + \mathrm{Decomp}([[0,0,0,1]_9])$$

but we know

$$[0,0,0,1]_9 \longrightarrow [0,0,0,1]_8 + [0,0,1,0]_8$$

so

$$[1,0,0,1]_9 \longrightarrow [1,0,0,0]_8 \otimes ([0,0,1,0]_8 + [0,0,0,1]_8) =$$
$$[1,0,1,0]_8 + [0,0,0,1]_8 + [1,0,0,1]_8 + [0,0,1,0]_8$$

which is what we were seeking.

Appendix B

Equations of motion for the background fields

The equations of motion for the background fields $\phi(z,x)$ and $\chi(z,x)$ obtained from action (5.1.5) are

$$\eta_1(\partial_z^2\phi)+\eta_2(\partial_x^2\phi)+\eta_3(\partial_z\partial_x\phi)+\eta_4(\partial_z\phi)^3+\eta_5(\partial_z\chi\partial_x\chi\partial_x\phi)+\eta_6(\partial_z\phi)=0\,, \tag{B.0.1}$$

$$\begin{aligned}&\tau_1(\partial_z^2\chi)+\tau_2(\partial_x^2\chi)+\tau_3(\partial_z\partial_x\chi)+\tau_4(\partial_z\chi)^3+\tau_5(\partial_z\chi)^2+\tau_6(\partial_z\chi)+\tau_7(\partial_x\chi)^2\\&+\tau_8(\partial_x\chi)+\tau_9\chi=0,\end{aligned} \tag{B.0.2}$$

where the coefficients η_i, $(i=1\dots7)$, and τ_i, $(i=1\dots9)$, are given by the following functions of z and x,

$$\begin{aligned}\eta_1(z,x)=&\,2h\left[hz^4(1-\chi^2)\dot\phi^2-f^2(h(1-\chi^2)+z^2\dot\chi^2)\right],\\ \eta_2(z,x)=&\,2h\left[hz^4(1-\chi^2)\phi'^2-f^2(1-\chi^2+z^2\chi'^2)\right],\\ \eta_3(z,x)=&\,4hz^2\left[f^2\chi'\dot\chi-hz^2(1-\chi^2)\phi'\dot\phi\right],\\ \eta_4(z,x)=&\,hz^3(zh'-2h)\left[2h(1-\chi^2)+z^2\dot\chi^2\right],\\ \eta_5(z,x)=&\,4fhz(2f-zf')+2hz^5\phi'^2(2h-zh'),\\ \eta_6(z,x)=&\,hz^3\dot\phi^2\left[-h\left(4(1-\chi^2)+2z^2\chi'^2\right)+zh'\left(3(1-\chi^2)+z^2\chi'^2\right)\right]\\&-2fhf'\left[-z^2\dot\chi^2-h\left(1-\chi^2-z^2\chi'^2\right)\right]+f^2\left[-2z^2\dot\chi^2h'+6h^2z\chi'^2\right.\\&\left.+\,h\left(-2z\dot\chi^2-h'(3(1-\chi^2)+z^2\chi'^2)\right)\right],\end{aligned} \tag{B.0.3}$$

$$
\begin{aligned}
\tau_1(z,x) &= 2hz^2\left[hz^4(1-\chi^2)\dot{\phi}^2 - f^2(h(1-\chi^2)+z^2\dot{\chi}^2)\right],\\
\tau_2(z,x) &= 2hz^2\left[hz^4(1-\chi^2)\phi'^2 - f^2(1-\chi^2+z^2\chi'^2)\right],\\
\tau_3(z,x) &= 4hz^4\left[f^2\chi'\dot{\chi} - hz^2\phi'\dot{\phi}(1-\chi^2)\right],\\
\tau_4(z,x) &= hz^3\left[6f^2h - 2fhzf' - 2hz^4\dot{\phi}^2 - zh'(f^2 - z^4\dot{\phi}^2)\right]\\
\tau_5(z,x) &= 6h^2z^2\chi(-f^2 + z^4\dot{\phi}^2) + 2hz^7\phi'(2h - zh')\dot{\phi}\dot{\chi},\\
\tau_6(z,x) &= z\Big\{ -2fhz\left(h(1-\chi^2)+z^2\dot{\chi}^2\right)f' + f^2\left[4h^2(1-\chi^2) - 2z^3\dot{\chi}^2h'\right.\\
&\quad \left. + hz\left(6z\dot{\chi}^2 - (1-\chi^2)h'\right)\right] + hz^4\left[-2h\phi'\left(6z\chi\dot{\phi}\dot{\chi} - 2h\chi^2\phi' + (2h+z^2\dot{\chi}^2)\right)\right.\\
&\quad \left. + zh'\left((1-\chi^2)\dot{\phi}^2 + \left(2h(1-\chi^2)+z^2\dot{\chi}^2\right)\phi'^2\right)\right]\Big\}\\
\tau_7(z,x) &= 6hz^2\chi\left(hz^4\phi'^2 - f^2\right),\\
\tau_8(z,x) &= -2hz^5(1-\chi^2)(2h - zh')\phi'\dot{\phi},\\
\tau_9(z,x) &= 4h^2\left[z^4\left(\dot{\phi}^2 + h\phi'^2\right) - f^2\right].
\end{aligned}
\tag{B.0.4}
$$

Appendix C

Quadratic action for the fluctuations

In this appendix we present the action of the fluctuations considered in section 5.4, and which allows us to compute the conductivity of the set-up. The action results from expanding the DBI action up to second order in the fluctuations (5.4.3), and can be written as

$$S^{(2)} = -N_f T_{D5}\, L^6 \int dt\, d^2x\, dz\, d\Omega_2\, \mathcal{L}^{(2)}\,, \tag{C.0.1}$$

with the definition of the functions Υ, Σ and Ω as

$$\begin{aligned}\Upsilon = {} & hz^4\left[(2-2\chi^2+z^2\,\dot\chi^2)\phi'^2 - 2z^2\,\dot\phi\,\dot\chi\,\phi'\,\chi' + (2h\,(1-\chi^2)+z^2\chi'^2)\,\dot\phi^2\right] \\ & - f^2\left[h\,(2-2\chi^2+z^2\dot\chi^2)+z^2\,\chi'^2\right], \end{aligned}\tag{C.0.2}$$

$$\begin{aligned}\Sigma = {} & (1-\chi^2)^2\Big\{h\,z^4\left[(1-\chi^2+z^2\,\dot\chi^2)\,\phi'^2 - 2z^2\,\dot\phi\,\dot\chi\,\phi'\,\chi' + \left(h\,(1-\chi^2)+z^2\,\chi'^2\right)\dot\phi^2\right] \\ & - f^2\left[h\,(1-\chi^2+z^2\,\dot\chi^2)+z^2\,\chi'^2\right]\Big\}, \end{aligned}\tag{C.0.3}$$

$$\begin{aligned}\Omega = {} & \Big\{hz^4\left[(2-6\chi^2+z^2\,\dot\chi^2)\,\phi'^2 - 2z^2\,\dot\phi\,\dot\chi\,\phi'\,\chi' + (2h\,(1-3\chi^2)+z^2\,\chi'^2)\,\dot\phi^2\right] \\ & - f^2\left[h\,(2-6\chi^2+z^2\,\dot\chi^2)+z^2\,\chi'^2\right]\Big\}. \end{aligned}\tag{C.0.4}$$

Then one has

$$\begin{aligned}
\mathcal{L}^{(2)} = &-\Delta\Bigg\{\Bigg[c\Upsilon\chi - z^2(1-\chi^2)(1-\chi^2)(a_t' - i\omega a_z)h^2z^2\dot{\phi} - f^2\chi'\dot{c} + h\Bigg(z^4\dot{\phi}\dot{c}(\dot{\phi}\chi' - \dot{\chi}\phi') \\
&- c'\left(\dot{\chi}(f^2 - z^4\phi'^2) + z^4\dot{\phi}\phi'\chi'\right) + z^4\chi'(\dot{\phi}\chi' - \dot{\chi}\phi')(a_t' - i\omega a_z) \\
&+ \left(z^4\dot{\phi}\dot{\chi}\chi' - z^2(1-\chi^2+z^2\dot{\chi}^2)\right)(i\omega a_x - \dot{a}_t)\Bigg)\Bigg]^2 \\
&- \frac{\Sigma}{h(1-\chi^2)}\Bigg[\Omega hc^2 - 4hz^2\chi c\dot{c}\left(hz^4\chi'\dot{\phi}^2 - f^2\chi' - hz^4\dot{\phi}\dot{\chi}\phi'\right) \\
&- h\left(z^4\dot{\phi}\phi'\chi' + \dot{\chi}(f^2 - z^4\phi'^2)\right)c' + hz^2\left(\dot{\phi}\left(2h(1-\chi^2) + z^2\chi'^2\right) - z^2\dot{\chi}\phi'\chi'\right)(a_t' - i\omega a_z) \\
&+ \left(hz^4\dot{\phi}\dot{\chi}\chi' - hz^2(2 - 2\chi^2 + z^2\dot{\chi}^2)\right)(i\omega a_x - \dot{a}_t) \\
&- z^2(1-\chi^2)\Bigg(h^3\left(2z^2i\omega(1-\chi^2)a_t'a_z - z^2(1-\chi^2)a_t'^2 + \omega^2\left(c^2 + z^2(1-\chi^2)\right)a_z^2\right) \\
&+ f^2z^2\left(z^2\chi'^2a_y'^2 - 2z^2\dot{\chi}\chi'a_y'\dot{a}_y + (1-\chi^2+z^2\dot{\chi}^2)\dot{a}_y^2\right) + h\Bigg(f^2z^2(1-\chi^2)a_x'^2 + f^2\dot{c}^2 \\
&+ z^2(1-\chi^2)(f^2 - z^4\phi'^2)a_y'^2 + z^4\omega^2\chi'^2a_y^2 + 2z^6(1-\chi^2)\dot{\phi}\phi'a_y'\dot{a}_y - z^6\dot{\phi}^2\dot{a}_y^2 + z^6\chi^2\dot{\phi}^2\dot{a}_y^2 \\
&- 2f^2z^2(1-\chi^2)a_x'a_z' + f^2z^2a_z'^2 - f^2z^2\chi^2a_z'^2\Bigg) - h^2\Bigg(2z^4\dot{\phi}\phi'c'\dot{c} - (f^2 - z^4\phi'^2)c'^2 \\
&- \phi'\chi'(a_t' - i\omega a_z) + (\dot{\phi}\chi' - 2\dot{\chi}\phi')(i\omega a_x - \dot{a}_t) \\
&+ z^2\Big(z^2\dot{\phi}^2\dot{c}^2 + 2z^2\dot{\chi}\phi'(i\omega ca_x' - \dot{c}a_t' + i\omega\dot{c}a_z) - (1-\chi^2+z^2\dot{\chi}^2)\omega^2(a_x^2 + a_y^2) \\
&+ 2z^2\dot{\phi}\chi'(2\dot{c}a_t' - i\omega\dot{c}a_z - i\omega ca_x') + z^2\chi'^2(a_t'^2 - 2i\omega a_t'a_z - \omega^2a_z^2) \\
&+ 2z^2\dot{\phi}\dot{\chi}\left((i\omega a_x - \dot{a}_t)\dot{c}\right) - 2z^2\dot{\chi}\chi'\left((i\omega a_z - a_t')(i\omega a_x - \dot{a}_t)\right) \\
&+ (1-\chi^2+z^2\dot{\chi}^2)(\dot{a}_t^2 - 2i\omega a_x\dot{a}_t) - 2z^2\left(\dot{\chi}\phi' + \dot{\phi}\chi'\right)i\omega ca_z\Big)\Bigg)\Bigg]\Bigg\},
\end{aligned} \tag{C.0.5}$$

where

$$\Delta = \frac{1}{2\,z^{16}\,\mathcal{L}^{(0)\,3}}, \tag{C.0.6}$$

$\mathcal{L}^{(0)}$ being the Lagrangian of the zeroth order DBI action, (5.1.5).
Note that we gauge away the radial gauge field component a_z once the equations of motion for the fluctuation fields have been found.

Appendix D

Schematic presentation of Mathematica codes

In this appendix we sketch the structure of the codes we use to get our results in chapters 5 and 6.

D.1 Codes for chapter 5

D.1.1 Setting up the grid

This part of the code is common similar for both chapters. It sets up the grid of collocation points, defines the spatial intervals and the derivative operators. It also generates the splitting in the grid along the x direction announced in (5.2.4) in `gridy1` and `gridy2`. In our definition of the equations of motion, the fields χ and ϕ are labelled `Chi[z,x]` and `A0[z,x]`.

```
SetGrid[Nradial_, Nspatial_, SpatialOrigin_, SpatialLength_,
 steepness_] := Block[{},
 Nx = Nradial;
 Ny = Nspatial;
 Nyh = IntegerPart[Ny/2];
 aa = steepness;
 ChebPoints[x0_, L_, n_Integer /; n > 1] :=
  x0 + L/2 (1 - Cos[\[Pi] Range[0, n - 1]/(n - 1)]);
 gridy1 = ChebPoints[SpatialOrigin, SpatialLength/2, Nyh] // N;
 gridy2 =
  ChebPoints[SpatialOrigin + SpatialLength/2, SpatialLength/2, Nyh] // N;
 gridy = Join[gridy1, gridy2];
 gridx = ChebPoints[0, 1, Nx] // N;
 grid1 = Table[{gridx[[i]], gridy1[[j]]}, {i, 1, Nx}, {j, 1, Nyh}];
 grid2 = Table[{gridx[[i]], gridy2[[j]]}, {i, 1, Nx}, {j, 1, Nyh}];
 (*The following quantities are defined on numerical purposes,
 since they pop up all the time*)
 rhonum2 = gridx^2;
 rhonum3 = gridx^3;
 rhonum4 = gridx^4;
 rhonum5 = gridx^5;
 rhonum6 = gridx^6;
 rhonum7 = gridx^7;
 rhonum8 = gridx^8;
 rhonum9 = gridx^9;
```

```
  rhonum10 = gridx^10;
  rhonum11 = gridx^11;
  rhonum12 = gridx^12;
  rhonum13 = gridx^13;
  hnum = 1 + rhonum4;
  hnumdr = 4 rhonum3;
  hnumdr2 = 12 rhonum2;
  fnum = 1 - rhonum4;
  fnumdr = -4 rhonum3;
  fnumdr2 = -12 rhonum2;
  (*Here the derivation matrices are found using the Mathematica
built-in definition.*)
    d1[1, 0] =
   NDSolve`FiniteDifferenceDerivative[{1, 0}, {gridx, gridy1},
    "DifferenceOrder" -> {"Pseudospectral", "Pseudospectral"},
    PeriodicInterpolation -> {False, False}];
  d1[0, 1] =
   NDSolve`FiniteDifferenceDerivative[{0, 1}, {gridx, gridy1},
    "DifferenceOrder" -> {"Pseudospectral", "Pseudospectral"},
    PeriodicInterpolation -> {False, False}];
  d1[2, 0] =
   NDSolve`FiniteDifferenceDerivative[{2, 0}, {gridx, gridy1},
    "DifferenceOrder" -> {"Pseudospectral", "Pseudospectral"},
    PeriodicInterpolation -> {False, False}];
  d1[0, 2] =
   NDSolve`FiniteDifferenceDerivative[{0, 2}, {gridx, gridy1},
    "DifferenceOrder" -> {"Pseudospectral", "Pseudospectral"},
    PeriodicInterpolation -> {False, False}];
  d1[1, 1] =
   NDSolve`FiniteDifferenceDerivative[{1, 1}, {gridx, gridy1},
    "DifferenceOrder" -> {"Pseudospectral", "Pseudospectral"},

  (*Here the EOMs are turned into a discrete numerical expression. *)
  EqnlistlocAb =
   Compile[{{{ChiNum1, _Real, {Nx, Nyh}}}, {{A0Num1, _Real, {Nx,
        Nyh}}}}, EqA2b /. numvalues];
  EqnlistlocCb =
   Compile[{{{ChiNum1, _Real, {Nx, Nyh}}}, {{A0Num1, _Real, {Nx,
        Nyh}}}}, EqC2b /. numvalues];

  (*Here the 2 EOMs are merged and the boundary condition equations \
substitute the corresponding lines *)
  Eqnlistdisb =
   Compile[{{{ChiNum1, _Real, {Nx, Nyh}}}, {{A0Num1, _Real, {Nx,
        Nyh}}}, {mass, _Real, 0}},
    Join[Transpose[
      Join[{Take[Transpose[d1[0, 1][A0Num1]][[1]], {2, Nx - 1}]},
       Transpose[
        Take[EqnlistlocAb[ChiNum1, A0Num1], {2, Nx - 1}, {2,
          Nyh - 1}]], {Take[
         Transpose[d1[0, 1][A0Num1]][[-1]], {2, Nx - 1}]}]], {d1[1,
        0][A0Num1][[-1]] + A0Num1[[-1]]}, {d1[1, 0][ChiNum1][[1]] -
       mass (2/(1 + Exp[-aa gridy1]) - 1)},
     Transpose[
      Join[{Take[Transpose[d1[0, 1][ChiNum1]][[1]], {2, Nx - 1}]},
       Transpose[
        Take[EqnlistlocCb[ChiNum1, A0Num1], {2, Nx - 1}, {2,
          Nyh - 1}]], {Take[
         Transpose[ChiNum1][[-1]], {2, Nx - 1}]}]], {d1[1, 0][
       ChiNum1][[-1]]}]];
  ]
```

where `numvalues` is the replacement

```
numvalues= {D[Chi[z, x], {x, 2}] -> d1[0, 2][ChiNum],
D[Chi[z, x], {z, 2}] -> d1[2, 0][ChiNum],
D[Chi[z, x], {z, 2}] -> d1[2, 0][ChiNum],
D[Chi[z, x], {z, 1}] -> d1[1, 0][ChiNum],
```

```
D[Chi[z, x], {x, 1}] -> d1[0, 1][ChiNum],
D[Chi[z, x], {z, 1}, {x, 1}] -> d1[1, 1][ChiNum], Chi[z, x] ->
 ChiNum, D[A0[z, x], {x, 2}] -> d1[0, 2][A0Num],
D[A0[z, x], {z, 2}] -> d1[2, 0][A0Num],
D[A0[z, x], {z, 2}] -> d1[2, 0][A0Num],
D[A0[z, x], {z, 1}] -> d1[1, 0][A0Num],
D[A0[z, x], {x, 1}] -> d1[0, 1][A0Num],
D[A0[z, x], {z, 1}, {x, 1}] -> d1[1, 1][A0Num], A0[z, x] -> A0Num,
h[z] -> hnum, h'[z] -> hnumdr, h''[z] -> hnumdr2, f[z] -> fnum,
f'[z] -> fnumdr, f''[z] -> fnumdr2, z^2 -> gridx2, z^3 -> gridx3,
z^4 -> gridx4, z^5 -> gridx5, z^6 -> gridx6, z^7 -> gridx7,
z^8 -> gridx8, z^9 -> gridx9, z^10 -> gridx10, z^11 -> gridx11,
z^12 -> gridx12, z^13 -> gridx13, z -> gridx, x -> gridy};
```

that assigns numerical values to the analytical variables. There is a further routine which sets up an auxiliary grid for the initial guess

```
SetGridguess[Nradial2_, Nspatial2_, SpatialOrigin_, SpatialLength_, ]
:= Module[{},   gridxguess = ChebPoints[0, 1, Nradial2] // N;
  gridy1guess =
   ChebPoints[SpatialOrigin, SpatialLength/2,
     IntegerPart[Nspatial2/2]] // N;
  gridy2guess =
   ChebPoints[SpatialOrigin + SpatialLength/2, SpatialLength/2,
     IntegerPart[Nspatial2/2]] // N;
  ];
```

which is used in first place before switching to the complete grid with the number of collocation points desired. It is one of the methods we mentioned in section 4.5 for getting a good seed.

D.1.2 Solving the background equations of motion

We then use the grid to solve for the background fields χ and ϕ which are numerically represented on the first half-interval by `ChiNum1` and `A0Num1`

```
SolveEOMs[Nradial_, Nspatial_, SpatialOrigin_, SpatialLength_,
 Accur_, ChemicalPotential_, Chimass_, MaxIter_, steepness_] :=
Block[{},
 time0 = AbsoluteTime[];
 Nxguess = 15;
 Nyguess = 30;
 SetGrid[Nxguess, Nyguess, SpatialOrigin,  SpatialLength,
  steepness];
 \[Delta] = 1/100000;
 accurwish = 10*Accur;
 chempot = ChemicalPotential;
 chibdy = Chimass; (*Must be small*)

 ChiNum1 =
  Table[chibdy gridx[[
     1]] (2/(1 + Exp[-steepness gridy1[[j]]]) - 1), {i, 1, Nx}, {j,
    1, Nyh}];
 A0Num1 = Table[chempot (1 - gridx[[i]]), {i, 1, Nx}, {j, 1, Nyh}];
 FieldNum = Join[A0Num1, ChiNum1];
 iter = 0;
 accur = 10.;]
  While[accur > accurwish,
   M1 = Eqnlistdisb[ChiNum1, A0Num1, chibdy];
   Jacob = {};
   For[m = 1, m < 2 Nx, m++;
    For[n = 0, n < Nyh, n++;
     FieldNum[[m, n]] = FieldNum[[m, n]] + \[Delta];
     A0Num1 = Take[FieldNum, {1, Nx}];
```

```
      ChiNum1 = Take[FieldNum, {Nx + 1, 2 Nx}];
      M2 = Eqnlistdisb[ChiNum1, A0Num1, chibdy];
      Jacob = Join[Jacob, {Flatten[(M2 - M1)/\[Delta]]}];
      FieldNum[[m, n]] = FieldNum[[m, n]] - \[Delta];, Null;];];
    sol = LinearSolve[Transpose[Jacob], -Flatten[M1]];
    solm = Partition[sol, Nyh];
    dFieldNum =
     Join[{Table[0., {i, 1, Nyh}]}, Take[solm, {1, 2 Nx - 1}]];
    FieldNum = FieldNum + dFieldNum;
    A0Num1 = Take[FieldNum, {1, Nx}];
    ChiNum1 = Take[FieldNum, {Nx + 1, 2 Nx}];
    iter++;
    accur = Max[Abs[dFieldNum]]/Max[Abs[FieldNum]];
    \[Delta] = Max[Abs[dFieldNum]]/1000;
    If[iter > MaxIter,
     Print["Maximum␣number␣of␣iterations␣allowed␣achieved␣in␣\
pre-run."]; Abort[];];
    ];
  Print["Pre-run␣ended␣after␣", iter, "␣iterations.␣and␣",
   AbsoluteTime[] - time0, "␣seconds." ];
  accurwish = Accur;
  SetGrid[Nradial, Nspatial, SpatialOrigin,  SpatialLength, steepness];
  SetGridguess[Nxguess, Nyguess, SpatialOrigin, SpatialLength];
  ChiNum1 =
   Table[Interpolation[
     Partition[
      Flatten[Table[{gridxguess[[i]], gridy1guess[[j]],
         ChiNum1[[i, j]]}, {i, 1, Nxguess}, {j, 1,
         IntegerPart[Nyguess/2]}]], 3], grid1[[k, j]]], {k, 1,
     Nx}, {j, 1, Nyh}];
  A0Num1 =
   Table[Interpolation[
     Partition[
      Flatten[Table[{gridxguess[[i]], gridy1guess[[j]],
         A0Num1[[i, j]]}, {i, 1, Nxguess}, {j, 1,
         IntegerPart[Nyguess/2]}]], 3], grid1[[k, j]]], {k, 1,
     Nx}, {j, 1, Nyh}];
  FieldNum = Join[A0Num1, ChiNum1];
  iter = 0;
  accur = 10.;
  \[Delta] = 1/1000000;
  While[accur > accurwish,
   M1 = Eqnlistdisb[ChiNum1, A0Num1, chibdy];
   Jacob = {};
   For[m = 1, m < 2 Nx, m++;
    For[n = 0, n < Nyh, n++;
     FieldNum[[m, n]] = FieldNum[[m, n]] + \[Delta];
     A0Num1 = Take[FieldNum, {1, Nx}];
     ChiNum1 = Take[FieldNum, {Nx + 1, 2 Nx}];
     M2 = Eqnlistdisb[ChiNum1, A0Num1, chibdy];
     Jacob = Join[Jacob, {Flatten[(M2 - M1)/\[Delta]]}];
     FieldNum[[m, n]] = FieldNum[[m, n]] - \[Delta];
     , Null;];];
   sol = LinearSolve[Transpose[Jacob], -Flatten[M1]];
   solm = Partition[sol, Nyh];
   dFieldNum =
    Join[{Table[0., {i, 1, Nyh}]}, Take[solm, {1, 2 Nx - 1}]];
   FieldNum = FieldNum + dFieldNum;
   A0Num1 = Take[FieldNum, {1, Nx}];
   ChiNum1 = Take[FieldNum, {Nx + 1, 2 Nx}];
   iter++;
   accur = Max[Abs[dFieldNum]]/Max[Abs[FieldNum]];
   \[Delta] = Max[Abs[dFieldNum]]/1000;
   If[iter > MaxIter,
    Print["Maximum␣number␣of␣iterations␣allowed␣achieved␣in␣\
pre-run."]; Abort[];];
   ];
```

```
A0Num2 = Transpose[Reverse[Transpose[A0Num1]]];
ChiNum2 = -Transpose[Reverse[Transpose[ChiNum1]]];
]
```

Where it must be taken into account that we are using a redefined version of the gauge field in (5.6.2). So for example when it comes to reading out the charge density we shall be interested in the quantity

```
2 A0Num1 - d1[1, 0][A0Num1]
```

Notice also that we feed into the auxiliary grid as an initial seed the fields

```
ChiNum1 =
  Table[chibdy gridx[[
     1]] (2/(1 + Exp[-steepness gridy1[[j]]]) - 1), {i, 1, Nx}, {j,
    1, Nyh}];
 A0Num1 = Table[chempot (1 - gridx[[i]]), {i, 1, Nx}, {j, 1, Nyh}];
```

which turn out to work out quite well.
We have another routine to look for solutions using a previous computed solution as a seed. This is useful when trying to obtain numerically complicated solutions like the ones which are close to the transition to the Minkowski embedding. We can then depart from an available solution and proceed towards the new one stepwise.

```
SolveEOMsUpon[Nradial_, Nspatial_, SpatialOrigin_, SpatialLength_,
 Accur_, ChemicalPotential_, Chimass_, MaxIter_] := Module[{},
 time0 = AbsoluteTime[];
 accurwish = Accur;
 chempot = ChemicalPotential;
 chibdy = Chimass;
 FieldNum[[1, 1 ;; Nyh]] = chempot;
 A0Num1[[1, 1 ;; Nyh]] = chempot;
 iter = 0;
 accur = 10.;
 \[Delta] = 1/1000000;
 While[accur > accurwish,
  M1 = Eqnlistdisb[ChiNum1, A0Num1, chibdy];
  Jacob = {};
  For[m = 1, m < 2 Nx, m++;
   For[n = 0, n < Nyh, n++;
    FieldNum[[m, n]] = FieldNum[[m, n]] + \[Delta];
    A0Num1 = Take[FieldNum, {1, Nx}];
    ChiNum1 = Take[FieldNum, {Nx + 1, 2 Nx}];
    M2 = Eqnlistdisb[ChiNum1, A0Num1, chibdy];
    Jacob = Join[Jacob, {Flatten[(M2 - M1)/\[Delta]]}];
    FieldNum[[m, n]] = FieldNum[[m, n]] - \[Delta];
    , Null;];];
  sol = LinearSolve[Transpose[Jacob], -Flatten[M1]];
  solm = Partition[sol, Nyh];
  dFieldNum =
   Join[{Table[0., {i, 1, Nyh}]}, Take[solm, {1, 2 Nx - 1}]];
  FieldNum = FieldNum + dFieldNum;
  A0Num1 = Take[FieldNum, {1, Nx}];
  ChiNum1 = Take[FieldNum, {Nx + 1, 2 Nx}];
  iter++;
  accur = Max[Abs[dFieldNum]]/Max[Abs[FieldNum]];
  If[iter > MaxIter,
   Print["Maximum␣number␣of␣iterations␣allowed␣achieved␣in␣\
pre-run."]; Abort[];];
  ];
 A0Num2 = Transpose[Reverse[Transpose[A0Num1]]];
 ChiNum2 = -Transpose[Reverse[Transpose[ChiNum1]]];
 ]
```

So for example in order to get the embedding we show in figure 5.3 we could proceed as follows

```
SolveEOMs[50, 100, -10, 20, 10^-12, 4., 3., 50, 3]
SolveEOMsUpon[50, 100, -10, 20, 10^-12, 4., 5., 50]
SolveEOMsUpon[50, 100, -10, 20, 10^-12, 4., 5.1, 50]
SolveEOMsUpon[50, 100, -10, 20, 10^-12, 4., 5.2, 50]
SolveEOMsUpon[50, 100, -10, 20, 10^-12, 4., 5.3, 50]
```

since getting the solution for $\mu = 4$ and $M = 3$ is possible, whereas getting directly the results for $M = 5.3$ is numerically more involved. Indeed, more steps are required as one gets closer to the most complicated embeddings, namely those which are closest to the Minkowski embeddings.
With the codes presented here and a grid of 50 collocation points along the radial direction and 100 points along the spatial direction x the resolution of the background data takes an average of around 400 seconds.

D.1.3 Solving the equations of motion for the fluctuations

Once we have solved for the background fields `ChiNum1` and `A0Num1` we can proceed to solve for the fluctuation fields a_y on the one hand and a_t, a_x and c on the other. Since they are linear differential equations, it is in principle possible to solve them by inverting matrices without resorting to iterative methods. Still, since our Newton-Raphson algorithm is already ready and working we stick to it and use it to solve for the fluctuations as well.
In our definition of the analytic equations of motion we label the fields `DAy[z,x]`, `DAt[z,x]`, `DAx[z,x]` and `DChi[z,x]`. They correspond to the fields defined in (5.4.10). They are numerically represented by the matrices `FlucNum`, `dAtNum`, `dAxNum` and `dChiNum` respectively. We first focus on the simpler case of a_y

Solving for a_y

We first store the background numerical data and the equations of motion to be solved together with the boundary conditions

```
GetNumbersY := Module[{},
 STORENUMERICALDATAFLUC[];
 Termsy = coefficientsay;
 Coefsay1 =
  Table[Coefficient[EqAyb, Termsy[[i]]], {i, 1, Length[Termsy]}] /.
   numvalues;
 Termsynum1 =
  Compile[{{FlucNum1, _Complex, {Nx, Nyh}}},
   Termsy /. numvaluesflucy];
 Eqnlistlocdy1 =
  Compile[{{FlucNum1, _Complex, {Nx, Ny}}},
   Total[Coefsay1 Termsynum1[FlucNum1]]];
 BCinwavey =
  Compile[{{FlucNum1, _Complex,
     2}}, {Last[d1[1, 0][FlucNum1]] + (I \[Omega] )/(4 Sqrt[2])
       Last[FlucNum1]}];
 BCvNl =
  Compile[{{FlucNum1, _Complex, 2}},
   Take[First[Transpose[d1[0, 1][FlucNum1]]], {2, Nx - 1}]];
 Even = Compile[{{FlucNum1, _Complex, 2}},
```

```
    Take[Transpose[d1[0, 1][FlucNum1]][[-1]], {2, Nx - 1}]];
  Odd = Compile[{{FlucNum1, _Complex, 2}},
    Take[Transpose[FlucNum1][[-1]], {2, Nx - 1}]];
  (*In case a Dirichlet BC is to be imposed*)
  prepeq1y =
   Compile[{{FlucNum1, _Complex, {Nx, Nyh}}},
    Transpose[
     Take[Eqnlistlocdy1[FlucNum1], {2, Nx - 1}, {2, Nyh - 1}]]];
  prepeqy =
   Compile[{{FlucNum1, _Complex, 2}},
    Transpose[
     Join[{BCvNl[FlucNum1]}, prepeq1y[FlucNum1], {Even[FlucNum1]}]]];
  Eqnlistdisflucy =
   Compile[{{FlucNum1, _Complex, 2}},
    Join[prepeqy[FlucNum1], BCinwavey[FlucNum1]]];
  ]
```

where `STORENUMERICALDATAFLUC` stores the common factors of the equations of motion for the fluctuation fields which contain just background data so that they do not have to be computed over and over. `coefficientsay` is just a list of the terms appearing in the equation of motion for a_y

```
coefficientsay={(DAy^(2,0))[z,x],(DAy^(0,2))[z,x],(DAy^(1,1))[z,x],
(DAy^(0,1))[z,x],(DAy^(1,0))[z,x],DAy[z,x]};
```

and `numvaluesflucy` stands for the substitution list that assigns to a_y the corresponding numerical values

```
numvaluesflucy={D[DAy[z,x],{x,2}]->d1[0,2][FlucNum1],
D[DAy[z],{z,2}]->d1[2,0][FlucNum1], D[DAy[z,x],{z,2}]->d1[2,0][FlucNum1],
D[DAy[z,x],{z,1}]->d1[1,0][FlucNum1], D[DAy[z,x],{x,1}]->d1[0,1][FlucNum1],
D[DAy[z,x],{z,1},{x,1}]->d1[1,1][FlucNum1],DAy[z,x]-> FlucNum1}
```

With all of this it is possible to proceed to solve the equation of motion for a_y and obtain a solution using

```
FlucRunC[InitialValue_, Accur_, freq_, MaxIter_] := Module[{},
 time0 = AbsoluteTime[];
 FlucNum1 = Table[InitialValue, {i, 1, Nx}, {j, 1, Nyh}];
 accur = 10;
 \[Delta] = 1/1000000;
 accurwish = Accur;
 \[Omega] = freq;
 \[Alpha] = freq/(2 Sqrt[2]);
 iter = 0;
 GetNumbersY;
 While[accur > accurwish,
  M1 = Eqnlistdisflucy[FlucNum1];
  dEqnlistdis = {};
  For[m = 1, m < Nx, m++;
   For[n = 0, n < Nyh, n++;
    FlucNum1[[m, n]] = FlucNum1[[m, n]] + \[Delta];
    M2 = Eqnlistdisflucy[FlucNum1];
    dEqnlistdis = Join[dEqnlistdis, {Flatten[(M2 - M1)/\[Delta]]}];
    FlucNum1[[m, n]] = FlucNum1[[m, n]] - \[Delta];];];
  sol = LinearSolve[Transpose[dEqnlistdis], -Flatten[M1]];
  solm = Partition[sol, Nyh];
  dFlucNum = Join[{Table[0., {i, 1, Nyh}]}, solm];
  FlucNum1 = FlucNum1 + dFlucNum;
  iter++;
  accur = Max[Abs[dFlucNum]]/Max[Abs[FlucNum1]];
  \[Delta] = Max[Abs[dFlucNum]]/1000;
  If[iter > MaxIter,
   Print["Maximum␣number␣of␣iterations␣allowed␣achieved␣in␣\
pre-run."]; Abort[];];];
  FlucNum2 = Transpose[Reverse[Transpose[FlucNum1]]];
```

```
]
```

From which the information about the charge density can be extracted and plotted, like

```
Flatten[Join[
 Table[-((I \[Alpha] FlucNum1[[1, i]]/(gridx[[1]] - 1) +
    d1[1, 0][FlucNum1][[1, i]])/(I \[Omega] FlucNum1[[1, i]])), {i,
   1, Nyh}],
 Table[-((I \[Alpha] FlucNum2[[1, i]]/(gridx[[1]] - 1) +
    d2[1, 0][FlucNum2][[1, i]])/(I \[Omega] FlucNum1[[1, i]])), {i,
   1, Nyh}]]]
```

With the codes presented here and a grid of 50 collocation points along the radial direction and 100 points along the spatial direction x the resolution of the equation of motion for a_y takes an average of around 45 seconds.

Solving for a_t, a_x and c

Let us now present the more involved code we use to solve the set of coupled partial differential equations of the fluctuations a_t, a_x and c in a short system (the adaptation to solve the long system is straightforward).

```
GetNumbersX := Module[{},
STORENUMERICALDATAFLUCX[];
 Terms = coefficientsx;
  Coefsat1 =
    Table[Coefficient[EqAtb, Terms[[i]]], {i, 1, Length[Terms]}] /.
     backgroundnum1;
  Coefsax1 =
    Table[Coefficient[EqAxb, Terms[[i]]], {i, 1, Length[Terms]}] /.
     backgroundnum1;
  Coefsdc1 =
    Table[Coefficient[EqdCb, Terms[[i]]], {i, 1, Length[Terms]}] /.
     backgroundnum1;
  Coefsaz1 =
    Table[Coefficient[EqAzb, Terms[[i]]], {i, 1, Length[Terms]}] /.
     backgroundnum1;
  Termsnum1 =
    Compile[{{{dAtNum1, _Complex, {Nx,
         Ny}}}, {{dAxNum1, _Complex, {Nx,
         Ny}}}, {{dChiNum1, _Complex, {Nx, Ny}}}},
     Terms /. numvaluesflucx];
  Eqnlistlocdt1 =
    Compile[{{{dAtNum1, _Complex, {Nx,
         Ny}}}, {{dAxNum1, _Complex, {Nx,
         Ny}}}, {{dChiNum1, _Complex, {Nx, Ny}}}},
     Total[Coefsat1 Termsnum1[dAtNum1, dAxNum1, dChiNum1]]];
  Eqnlistlocdx1 =
    Compile[{{{dAtNum1, _Complex, {Nx,
         Ny}}}, {{dAxNum1, _Complex, {Nx,
         Ny}}}, {{dChiNum1, _Complex, {Nx, Ny}}}},
     Total[Coefsax1 Termsnum1[dAtNum1, dAxNum1, dChiNum1]]];
  Eqnlistlocdc1 =
    Compile[{{{dAtNum1, _Complex, {Nx,
         Ny}}}, {{dAxNum1, _Complex, {Nx,
         Ny}}}, {{dChiNum1, _Complex, {Nx, Ny}}}},
     Total[Coefsdc1 Termsnum1[dAtNum1, dAxNum1, dChiNum1]]];
  Eqnlistlocaz1 =
    Compile[{{{dAtNum1, _Complex, {Nx,
         Ny}}}, {{dAxNum1, _Complex, {Nx,
         Ny}}}, {{dChiNum1, _Complex, {Nx, Ny}}}},
     Total[Coefsaz1 Termsnum1[dAtNum1, dAxNum1, dChiNum1]]];
  Even = Compile[{{FlucNum1, _Complex, 2}},
```

```
   Take[Transpose[d1[0, 1][FlucNum1]][[-1]], {2, Nx - 1}]];
Odd = Compile[{{FlucNum1, _Complex, 2}},
   Take[Transpose[FlucNum1][[-1]], {2, Nx - 1}]];
ConstantE =
  Compile[{{{dAtNum1, _Complex, 2}}, {{dAxNum1, _Complex,
      2}}}, {I \[Omega] dAxNum1[[1]] - d1[0, 1][dAtNum1][[1]] -
     I \[Omega]}];
BCspatt =
  Compile[{{dAtNum1, _Complex, 2}}, {Take[
     Transpose[dAtNum1][[1]], {2, Nx - 1}]}];
(*In case we need it for the long system*)
BCspatx =
  Compile[{{dAxNum1, _Complex, 2}}, {Take[
     First[Transpose[d1[0, 1][dAxNum1]]], {2, Nx - 1}]}];
BCspatc =
  Compile[{{dChiNum1, _Complex, 2}}, {Take[
     First[Transpose[d1[0, 1][dChiNum1]]], {2, Nx - 1}]}];
BCinwavex =
  Compile[{{dAxNum1, _Complex,
     2}}, {d1[1, 0][dAxNum1][[-1]] + (I \[Omega])/(4 R)
       dAxNum1[[-1]]}];
BCinwavec =
  Compile[{{dChiNum1, _Complex,
     2}}, {d1[1, 0][dChiNum1][[-1]] + (I \[Omega])/(4 R)
       dChiNum1[[-1]]}];
ConstraintUV =
  Compile[{{{dAtNum1, _Complex, 2}}, {{dAxNum1, _Complex,
      2}}}, {\[Alpha] \[Omega] dAtNum1[[1]] +
     I \[Omega] d1[1, 0][dAtNum1][[1]] +
     I \[Alpha] d1[0, 1][dAxNum1][[1]] - d1[1, 1][dAxNum1][[1]]}];
ConstantM =
  Compile[{{dChiNum1, _Complex, 2}}, {d1[1, 0][dChiNum1][[1]] -
     I \[Alpha] dChiNum1[[1]]}];
prepeqt =
  Compile[{{{dAtNum1, _Complex, 2}}, {{dAxNum1, _Complex,
      2}}, {{dChiNum1, _Complex, 2}}},
   Join[BCspatt[dAtNum1],
    prepeqt[dAtNum1, dAxNum1, dChiNum1], {Odd[dAtNum1]}]];
prepeqc =
  Compile[{{{dAtNum1, _Complex, 2}}, {{dAxNum1, _Complex,
      2}}, {{dChiNum1, _Complex, 2}}},
   Join[BCspatc[dChiNum1],
    prepeqc[dAtNum1, dAxNum1, dChiNum1], {Even[dChiNum1]}]];
prepeqx =
  Compile[{{{dAtNum1, _Complex, 2}}, {{dAxNum1, _Complex,
      2}}, {{dChiNum1, _Complex, 2}}},
   Join[prepeqx[dAtNum1, dAxNum1, dChiNum1], {Even[dAxNum1]}]];
eomt = Compile[{{{dAtNum1, _Complex, 2}}, {{dAxNum1, _Complex,
      2}}, {{dChiNum1, _Complex, 2}}},
   Transpose[prepeqt[dAtNum1, dAxNum1, dChiNum1]]];
eomc = Compile[{{{dAtNum1, _Complex, 2}}, {{dAxNum1, _Complex,
      2}}, {{dChiNum1, _Complex, 2}}},
   Join[Transpose[prepeqc[dAtNum1, dAxNum1, dChiNum1]],
    BCinwavec[dChiNum1]]];
eomx = Compile[{{{dAtNum1, _Complex, 2}}, {{dAxNum1, _Complex,
      2}}, {{dChiNum1, _Complex, 2}}},
   Join[Transpose[prepeqx[dAtNum1, dAxNum1, dChiNum1]],
    BCinwavex[dAxNum1]]];
Eqnlistdisfluc =
  Compile[{{{dAtNum1, _Complex, {Nx,
       Nyh}}}, {{dAxNum1, _Complex, {Nx,
       Nyh}}}, {{dChiNum1, _Complex, {Nx, Nyh}}}},
   Join[ConstantE[dAtNum1, dAxNum1],
    eomt[dAtNum1, dAxNum1, dChiNum1],
    ConstraintUV[dAtNum1, dAxNum1],
    eomx[dAtNum1, dAxNum1, dChiNum1], ConstantM[dChiNum1],
    eomc[dAtNum1, dAxNum1, dChiNum1]
```

```
    ]];
];
```

where `STORENUMERICALDATAFLUCX` stores the common factors of the equations of motion for the fluctuation fields which contain just background data so that they do not have to be computed over and over. `coefficientsax` is just a list of the terms appearing in the equation of motion for the fields

```
coefficientsax{(DAt^(2,0))[z,x],(DAt^(0,2))[z,x],(DAt^(1,1))[z,x],(DAt^(0,1))[z,x],
(DAt^(1,0))[z,x],DAt[z,x],(DAx^(2,0))[z,x],(DAx^(0,2))[z,x],(DAx^(1,1))[z,x],
(DAx^(0,1))[z,x],(DAx^(1,0))[z,x],DAx[z,x],(DChi^(2,0))[z,x],(DChi^(0,2))[z,x],
(DChi^(1,1))[z,x],(DChi^(0,1))[z,x],(DChi^(1,0))[z,x],DChi[z,x]}
```

With this code it is possible to proceed to solve the equations of motion of the fluctuation fields a_t, a_x and c by means of

```
FlucRunXOut[InitialValuet_, InitialValuex_, InitialValuec_, Accur_,
 freq_, MaxIter_] := Block[{},
 time0 = AbsoluteTime[];
 dAtNum1 = Table[InitialValuet, {i, 1, Nx}, {j, 1, Nyh}];
 dAxNum1 = Table[InitialValuex, {i, 1, Nx}, {j, 1, Nyh}];
 dChiNum1 = Table[InitialValuec, {i, 1, Nx}, {j, 1, Nyh}];
 accur = 10;
 accurwish = Accur;
 \[Omega] = freq;
 \[Alpha] = freq/(2 R);
 GetNumbersX;
 iter = 0;
 \[Delta] = 1/1000000;
 FlucNum = Join[dAtNum1, dAxNum1, dChiNum1];
 While[accur > accurwish,
  M1 = Eqnlistdisfluc[dAtNum1, dAxNum1, dChiNum1];
  dEqnlistdis = {};
  For[m = 0, m < 3 Nx, m++;
   If[m != Nx ,
    For[n = 0, n < Nyh, n++;
      FlucNum[[m, n]] = FlucNum[[m, n]] + \[Delta];
      dAtNum1 = Take[FlucNum, {1, Nx}];
      dAxNum1 = Take[FlucNum, {Nx + 1, 2 Nx}];
      dChiNum1 = Take[FlucNum, {2 Nx + 1, 3 Nx}];
      M2 = Eqnlistdisfluc[dAtNum1, dAxNum1, dChiNum1];
      dEqnlistdis =
       Join[dEqnlistdis, {Flatten[(M2 - M1)/\[Delta]]}];
      FlucNum[[m, n]] = FlucNum[[m, n]] - \[Delta];, Null;];];];
  sol = LinearSolve[Transpose[dEqnlistdis], -Flatten[M1]];
  solm = Partition[sol, Nyh];
  dFlucNum =
   Join[Take[solm, {1, Nx - 1}], {Table[0., {i, 1, Nyh}]},
    Take[solm, {Nx, 3 Nx - 1}]];
  FlucNum = FlucNum + dFlucNum;
  dAtNum1 = Take[FlucNum, {1, Nx}];
  dAxNum1 = Take[FlucNum, {Nx + 1, 2 Nx}];
  dChiNum1 = Take[FlucNum, {2 Nx + 1, 3 Nx}];
  iter++;
  accur = Max[Abs[dFlucNum]]/Max[Abs[FlucNum]];
  (*Print[" accur= ",accur,
  " \[Delta]= ", \[Delta]];*)
  \[Delta] = Max[Abs[dFlucNum]]/1000;
  If[iter > MaxIter,
   Print["Maximum number of iterations allowed achieved."]; Abort[];];
  ];
 dAtNum2 = -Transpose[Reverse[Transpose[dAtNum1]]];
 dAxNum2 = Transpose[Reverse[Transpose[dAxNum1]]];
 dChiNum2 = Transpose[Reverse[Transpose[dChiNum1]]];
 ]
```

from which the information about the conductivity along the direction transverse to the interface can be extracted as

```
Flatten[
Join[Table[(
  I \[Alpha] dAxNum1[[1, i]]/(gridx[[1]] - 1) +
   d1[1, 0][dAxNum1][[1, i]])/(-I \[Omega] dAxNum1[[1, i]] +
   d1[0, 1][dAtNum1][[1, i]]), {i, 1, Nyh}],
 Table[(I \[Alpha] dAxNum2[[1, i]]/(gridx[[1]] - 1) +
   d2[1, 0][dAxNum2][[1, i]])/(-I \[Omega] dAxNum2[[1, i]] +
   d2[0, 1][dAtNum2][[1, i]]), {i, 1, Nyh}]]]
```

It is furthermore convenient to keep an eye on the numerical fulfilment of the constraint equation as a sign of good numerical work

```
ListPlot3D[
Partition[
 Flatten[Table[{gridx[[i]], gridy[[j]],
    If[j <= Nyh,
     Re[Eqnlistlocaz1[dAtNum1, dAxNum1, dChiNum1][[i, j]]],
     Re[Eqnlistlocaz1[dAtNum2, dAxNum2, dChiNum2][[i,
       Nyh - j]]]]}, {i, 1, Nx - 1}, {j, 1, 2 Nyh}]], 3]]
```

With the codes presented here and a grid of 50 collocation points along the radial direction and 100 points along the spatial direction x the resolution of the coupled equations of motion for a_t, a_x and c takes an average of around 2000 seconds.

D.2 Codes for chapter 6

There are minimal differences in the codes we use in the resolution of the equations of motion of chapter 6 compared to the codes above. These basically respond to the different boundary conditions at the spatial boundaries, which are now periodic, and to the way in which solutions in the presence of disorder are found departing from homogeneous solutions.

D.2.1 Setting up the grid

The grid is set up by the same routine as in the previous section, with the only difference that periodic boundary conditions are required when invoking the differentiation matrices

```
d[1, 0] =
 NDSolve`FiniteDifferenceDerivative[{1, 0}, {gridx, gridy},
  "DifferenceOrder" -> {"Pseudospectral", "Pseudospectral"},
  PeriodicInterpolation -> {False, True}];
d[0, 1] =
 NDSolve`FiniteDifferenceDerivative[{0, 1}, {gridx, gridy},
  "DifferenceOrder" -> {"Pseudospectral", "Pseudospectral"},
  PeriodicInterpolation -> {False, True}];
d[2, 0] =
 NDSolve`FiniteDifferenceDerivative[{2, 0}, {gridx, gridy},
  "DifferenceOrder" -> {"Pseudospectral", "Pseudospectral"},
  PeriodicInterpolation -> {False, True}];
d[0, 2] =
 NDSolve`FiniteDifferenceDerivative[{0, 2}, {gridx, gridy},
  "DifferenceOrder" -> {"Pseudospectral", "Pseudospectral"},
  PeriodicInterpolation -> {False, True}];
```

```
d[1, 1] =
  NDSolve`FiniteDifferenceDerivative[{1, 1}, {gridx, gridy},
   "DifferenceOrder" -> {"Pseudospectral", "Pseudospectral"},
   PeriodicInterpolation -> {False, True}];
d[1] = NDSolve`FiniteDifferenceDerivative[{1}, {gridx},
   "DifferenceOrder" -> {"Pseudospectral"},
   PeriodicInterpolation -> {False}];
d[2] = NDSolve`FiniteDifferenceDerivative[{2}, {gridx},
   "DifferenceOrder" -> {"Pseudospectral"},
   PeriodicInterpolation -> {False}];
```

and that the homogeneous equation of motion and that of the massless case are considered separately for practical reasons, that is we also define

```
 Eqnlistloc1hom =
  Compile[{{ChiNumhom, _Real, {Nx}}, {{A0Numhom, _Real, {Nx}}}},
   EqAhom /. numericalvalueshomog];
Eqnlistloc2hom =
  Compile[{{ChiNumhom, _Real, {Nx,
      Ny}}, {{A0Numhom, _Real, {Nx, Ny}}}},
   EqChom /. numericalvalueshomog];
Eqnlistdishom[ChiNumhom_, A0Numhom_, mass_] :=
  Join[Take[
    Eqnlistloc1hom[ChiNumhom, A0Numhom], {2,
     Nx - 1}], {d[1][A0Numhom][[-1]] +
     A0Numhom[[-1]]}, {d[1][ChiNumhom][[1]] - mass},
   Take[Eqnlistloc2hom[ChiNumhom, A0Numhom], {2,
     Nx - 1}], {d[1][ChiNumhom][[-1]]}];
```

with `numericalvalueshomog` standing for

```
{D[Chi[z], {z, 2}] -> d[2][ChiNumhom],
D[Chi[z], {z, 1}] -> d[1][ChiNumhom], Chi[z] -> ChiNumhom,
D[A0[z], {z, 2}] -> d[2][A0Numhom],
D[A0[z], {z, 1}] ->
 d[1][A0Numhom], A0[z] -> A0Numhom, h[z] -> hnum,
h'[z] -> hnumdr, h''[z] -> hnumdr2, f[z] -> fnum, f'[z] -> fnumdr,
f''[z] -> fnumdr2, z^2 -> rhonum2, z^3 -> rhonum3, z^4 -> rhonum4,
z^5 -> rhonum5, z^6 -> rhonum6, z^7 -> rhonum7, z^8 -> rhonum8,
z^9 -> rhonum9, z^10 -> rhonum10, z^11 -> rhonum11, z^12 -> rhonum12,
 z^13 -> rhonum13, z -> gridx}
```

and `EqAhom` and `EqChom` are the analytic expressions for the homogeneous background equations of motion, that is those with no x dependence.

D.2.2 Solving the background and the fluctuation equations of motion

Apart from the differences in the output, which now mainly consists of mean values and from structure changes due to the different way in which solutions are found by building upon the homogeneous clean solution, no relevant modifications of the codes that solve the equations of motion are necessary. The same codes may be used as in chapter 5.

Bibliography

[1] A. Burov and L. Burov, *Genesis of a Pythagorean Universe.*, .

[2] M. S. Leifer, *Mathematics Is Physics*, *ArXiv e-prints* (Aug., 2015) [1508.02770].

[3] E. Wigner, *The Unreasonable Effectiveness of Mathematics in the Natural Sciences*, *Communications in Pure and Applied Mathematics* **13** (Feb., 1960).

[4] J. Earman, *Laws, symmetry, and symmetry breaking: Invariance, conservation principles, and objectivity*, *Philosophy of Science* **71** (2004), no. 5 1227–1241.

[5] B. C. Van Fraassen, *Laws and Symmetry*. Oxford University Press, 1989.

[6] **ATLAS** Collaboration, G. Aad *et. al.*, *Observation of a new particle in the search for the Standard Model Higgs boson with the ATLAS detector at the LHC*, *Phys. Lett.* **B716** (2012) 1–29 [1207.7214].

[7] **CMS** Collaboration, S. Chatrchyan *et. al.*, *Observation of a new boson at a mass of 125 GeV with the CMS experiment at the LHC*, *Phys. Lett.* **B716** (2012) 30–61 [1207.7235].

[8] F. Englert and R. Brout, *Broken Symmetry and the Mass of Gauge Vector Mesons*, *Physical Review Letters* **13** (Aug., 1964) 321–323.

[9] P. W. Higgs, *Broken symmetries and the masses of gauge bosons*, *Phys. Rev. Lett.* **13** (Oct, 1964) 508–509.

[10] G. S. Guralnik, C. R. Hagen and T. W. B. Kibble, *Global conservation laws and massless particles*, *Phys. Rev. Lett.* **13** (Nov, 1964) 585–587.

[11] A. S. Alexandrov, *Strong-Coupling Theory of High Temperature Superconductivity*, *eprint arXiv:cond-mat/0508769* (Aug., 2005) [cond-mat/0508769].

[12] H. L. Stormer, D. C. Tsui and A. C. Gossard, *The fractional quantum hall effect*, *Rev. Mod. Phys.* **71** (Mar, 1999) S298–S305.

[13] **BICEP2** Collaboration, P. A. R. Ade *et. al.*, *Detection of B-Mode Polarization at Degree Angular Scales by BICEP2*, *Phys. Rev. Lett.* **112** (2014), no. 24 241101 [1403.3985].

[14] **BICEP2** Collaboration, P. A. R. Ade *et. al.*, *BICEP2 II: Experiment and Three-Year Data Set*, *Astrophys. J.* **792** (2014), no. 1 62 [1403.4302].

[15] **ATLAS** Collaboration, G. Aad *et. al.*, *Summary of the ATLAS experiment's sensitivity to supersymmetry after LHC Run 1 - interpreted in the phenomenological MSSM*, 1508.06608.

[16] **CMS** Collaboration, V. Khachatryan *et. al.*, *Search for supersymmetry with photons in pp collisions at* $\sqrt{s} = 8$ *TeV*, 1507.02898.

[17] L. Ibáñez and A. Uranga, *String Theory and Particle Physics: An Introduction to String Phenomenology*. Cambridge University Press, 2012.

[18] J. M. Maldacena, *The Large N limit of superconformal field theories and supergravity*, *Int.J.Theor.Phys.* **38** (1999) 1113–1133 [hep-th/9711200].

[19] E. Witten, *Anti-de Sitter space and holography*, *Adv. Theor. Math. Phys.* **2** (1998) 253–291 [hep-th/9802150].

[20] S. Gubser, I. R. Klebanov and A. M. Polyakov, *Gauge theory correlators from noncritical string theory*, *Phys.Lett.* **B428** (1998) 105–114 [hep-th/9802109].

[21] P. Kovtun, D. T. Son and A. O. Starinets, *Viscosity in strongly interacting quantum field theories from black hole physics*, *Phys. Rev. Lett.* **94** (2005) 111601 [hep-th/0405231].

[22] D. K. OKeeffe and A. W. Peet, *Perturbatively charged holographic disorder*, *Phys. Rev.* **D92** (2015), no. 4 046004 [1504.03288].

[23] U. A. M. Ibáñez, Luís E., *String Theory and Particle Physics. An Introduction to String Phenomenology*. Cambridge University Press, 2012.

[24] M. Rozali, *Compressible Matter at an Holographic Interface*, *Phys.Rev.Lett.* **109** (2012) 231601 [1210.0029].

[25] C. Hoyos-Badajoz, K. Jensen and A. Karch, *A Holographic Fractional Topological Insulator*, *Phys.Rev.* **D82** (2010) 086001 [1007.3253].

[26] A. Karch, J. Maciejko and T. Takayanagi, *Holographic fractional topological insulators in 2+1 and 1+1 dimensions*, *Phys.Rev.* **D82** (2010) 126003 [1009.2991].

[27] D. Arean, A. Farahi, L. A. Pando Zayas, I. S. Landea and A. Scardicchio, *A Dirty Holographic Superconductor*, *Phys.Rev.* **D89** (2014) 106003 [1308.1920].

[28] D. Arean, A. Farahi, L. A. Pando Zayas, I. S. Landea and A. Scardicchio, *Holographic p-wave Superconductor with Disorder*, *JHEP* **07** (2015) 046 [1407.7526].

[29] H. B. Zeng, *Possible Anderson localization in a holographic superconductor*, *Phys. Rev.* **D88** (2013), no. 12 126004 [1310.5753].

[30] S. A. Hartnoll and J. E. Santos, *Disordered horizons: Holography of randomly disordered fixed points*, *Phys.Rev.Lett.* **112** (2014) 231601 [1402.0872].

[31] A. Lucas, S. Sachdev and K. Schalm, *Scale-invariant hyperscaling-violating holographic theories and the resistivity of strange metals with random-field disorder*, *Phys. Rev.* **D89** (2014), no. 6 066018 [1401.7993].

[32] S. Ryu, T. Takayanagi and T. Ugajin, *Holographic Conductivity in Disordered Systems*, *JHEP* **1104** (2011) 115 [1103.6068].

[33] S. A. Hartnoll, *Lectures on holographic methods for condensed matter physics*, *Class. Quant. Grav.* **26** (2009) 224002 [0903.3246].

[34] S. Das Sarma, S. Adam, E. H. Hwang and E. Rossi, *Electronic transport in two-dimensional graphene*, *Rev. Mod. Phys.* **83** (May, 2011) 407–470.

[35] E. H. Hwang, S. Adam and S. D. Sarma, *Carrier transport in two-dimensional graphene layers*, *Phys. Rev. Lett.* **98** (May, 2007) 186806.

[36] Q. Li, E. H. Hwang, E. Rossi and S. Das Sarma, *Theory of 2d transport in graphene for correlated disorder*, *Phys. Rev. Lett.* **107** (Oct, 2011) 156601.

[37] S. A. Hartnoll and D. M. Hofman, *Locally Critical Resistivities from Umklapp Scattering*, *Phys. Rev. Lett.* **108** (2012) 241601 [1201.3917].

[38] J. Sonner, *On universality of charge transport in AdS/CFT*, *JHEP* **07** (2013) 145 [1304.7774].

[39] C. P. Herzog, K.-W. Huang and R. Vaz, *Linear Resistivity from Non-Abelian Black Holes*, *JHEP* **11** (2014) 066 [1405.3714].

[40] D. Vegh, *Holography without translational symmetry*, 1301.0537.

[41] M. Blake, D. Tong and D. Vegh, *Holographic Lattices Give the Graviton an Effective Mass*, *Phys.Rev.Lett.* **112** (2014), no. 7 071602 [1310.3832].

[42] N. Iqbal and H. Liu, *Universality of the hydrodynamic limit in AdS/CFT and the membrane paradigm*, *Phys.Rev.* **D79** (2009) 025023 [0809.3808].

[43] M. Araujo, D. Arean, J. Erdmenger and J. M. Lizana, *Holographic charge localization at brane intersections*, *JHEP* **08** (2015) 146 [1505.05883].

[44] M. Araujo, D. Arean and J. M. Lizana, *Noisy brane intersections*, To appear.

[45] M. Ammon and J. Erdmenger, *Gauge/Gravity Duality. Foundations and Applications.* Cambridge University Press, 2015.

[46] O. Aharony, S. S. Gubser, J. M. Maldacena, H. Ooguri and Y. Oz, *Large N field theories, string theory and gravity*, *Phys.Rept.* **323** (2000) 183–386 [hep-th/9905111].

[47] E. D'Hoker and D. Z. Freedman, *Supersymmetric gauge theories and the AdS / CFT correspondence*, hep-th/0201253.

[48] F. Quevedo, S. Krippendorf and O. Schlotterer, *Cambridge Lectures on Supersymmetry and Extra Dimensions*, 1011.1491.

[49] J. A. Minahan, *Review of AdS/CFT Integrability, Chapter I.1: Spin Chains in N=4 Super Yang-Mills*, *Lett. Math. Phys.* **99** (2012) 33–58 [1012.3983].

[50] D. Serban, *Integrability and the AdS/CFT correspondence*, *J. Phys.* **A44** (2011) 124001 [1003.4214].

[51] R. Grimm, M. Sohnius and J. Wess, *Extended Supersymmetry and Gauge Theories*, *Nucl. Phys.* **B133** (1978) 275.

[52] C. G. Callan, Jr., J. A. Harvey and A. Strominger, *Worldbrane actions for string solitons*, *Nucl. Phys.* **B367** (1991) 60–82.

[53] D. M. Kaplan and J. Michelson, *Zero modes for the D = 11 membrane and five-brane*, *Phys. Rev.* **D53** (1996) 3474–3476 [hep-th/9510053].

[54] T. Adawi, M. Cederwall, U. Gran, B. E. W. Nilsson and B. Razaznejad, *Goldstone tensor modes*, *JHEP* **02** (1999) 001 [hep-th/9811145].

[55] E. Witten, *Bound states of strings and p-branes*, *Nucl. Phys.* **B460** (1996) 335–350 [hep-th/9510135].

[56] E. Witten, *Baryons in the 1n expansion*, *Nuclear Physics B* **160** (1979), no. 1 57 – 115.

[57] L. Brink, J. H. Schwarz and J. Scherk, *Supersymmetric yang-mills theories*, *Nuclear Physics B* **121** (1977), no. 1 77 – 92.

[58] F. Gliozzi, J. Scherk and D. Olive, *Supersymmetry, supergravity theories and the dual spinor model*, *Nuclear Physics B* **122** (1977), no. 2 253 – 290.

[59] J. Casalderrey-Solana, H. Liu, D. Mateos, K. Rajagopal and U. A. Wiedemann, *Gauge/String Duality, Hot QCD and Heavy Ion Collisions*, 1101.0618.

[60] G. 't Hooft, *A Planar Diagram Theory for Strong Interactions*, *Nucl. Phys.* **B72** (1974) 461.

[61] A. Beraudo, J. P. Blaizot and C. Ratti, *Real and imaginary-time Q anti-Q correlators in a thermal medium*, *Nucl. Phys.* **A806** (2008) 312–338 [0712.4394].

[62] K. Becker, M. Becker and J. Schwarz, *String Theory and M-Theory: A Modern Introduction*. Cambridge University Press, 2006.

[63] E. Witten, *Anti-de Sitter space, thermal phase transition, and confinement in gauge theories*, *Adv. Theor. Math. Phys.* **2** (1998) 505–532 [hep-th/9803131].

[64] G. W. Gibbons and S. W. Hawking, *Action Integrals and Partition Functions in Quantum Gravity*, *Phys. Rev.* **D15** (1977) 2752–2756.

[65] D. Tong, *String Theory*, 0908.0333.

[66] J. Polchinski, *String Theory, Voluyme I*. Cambridge University Press, 2007.

[67] S. Kobayashi, D. Mateos, S. Matsuura, R. C. Myers and R. M. Thomson, *Holographic phase transitions at finite baryon density*, *JHEP* **0702** (2007) 016 [hep-th/0611099].

[68] D. Mateos, S. Matsuura, R. C. Myers and R. M. Thomson, *Holographic phase transitions at finite chemical potential*, *JHEP* **0711** (2007) 085 [0709.1225].

[69] J. Mas, J. P. Shock, J. Tarrio and D. Zoakos, *Holographic Spectral Functions at Finite Baryon Density*, *JHEP* **0809** (2008) 009 [0805.2601].

[70] J. Erdmenger, M. Kaminski and F. Rust, *Holographic vector mesons from spectral functions at finite baryon or isospin density*, *Phys.Rev.* **D77** (2008) 046005 [0710.0334].

[71] D. Mateos, R. C. Myers and R. M. Thomson, *Holographic phase transitions with fundamental matter*, *Phys.Rev.Lett.* **97** (2006) 091601 [hep-th/0605046].

[72] D. Mateos, R. C. Myers and R. M. Thomson, *Thermodynamics of the brane*, *JHEP* **0705** (2007) 067 [hep-th/0701132].

[73] M. Kruczenski, D. Mateos, R. C. Myers and D. J. Winters, *Towards a holographic dual of large N(c) QCD*, *JHEP* **05** (2004) 041 [hep-th/0311270].

[74] D. Arean and A. V. Ramallo, *Open string modes at brane intersections*, *JHEP* **0604** (2006) 037 [hep-th/0602174].

[75] R. C. Myers and R. M. Thomson, *Holographic mesons in various dimensions*, *JHEP* **0609** (2006) 066 [hep-th/0605017].

[76] J. Erdmenger, N. Evans, I. Kirsch and E. Threlfall, *Mesons in Gauge/Gravity Duals - A Review*, *Eur. Phys. J.* **A35** (2008) 81–133 [0711.4467].

[77] J. Babington, J. Erdmenger, N. J. Evans, Z. Guralnik and I. Kirsch, *Chiral symmetry breaking and pions in nonsupersymmetric gauge / gravity duals*, *Phys.Rev.* **D69** (2004) 066007 [hep-th/0306018].

[78] N. Evans and E. Threlfall, *Chemical Potential in the Gravity Dual of a 2+1 Dimensional System*, *Phys.Rev.* **D79** (2009) 066008 [0812.3273].

[79] D. T. Son and A. O. Starinets, *Minkowski space correlators in AdS / CFT correspondence: Recipe and applications*, *JHEP* **09** (2002) 042 [hep-th/0205051].

[80] J. P. Boyd, *Chebyshev and Fourier Spectral Methods*. DOVER Publications Inc., 2000.

[81] L. N. Trefethen, *Spectral Methods in Matlab*. Society for Industrial and Applied Mathematics, 2000.

[82] P. M. J. B. C. C. Landau, Rubin H., *Computational Physics*. Wiley-VCH, 2013.

[83] S. Kachru, A. Karch and S. Yaida, *Holographic Lattices, Dimers, and Glasses*, *Phys.Rev.* **D81** (2010) 026007 [0909.2639].

[84] S. Kachru, A. Karch and S. Yaida, *Adventures in Holographic Dimer Models*, *New J.Phys.* **13** (2011) 035004 [1009.3268].

[85] G. T. Horowitz, J. E. Santos and D. Tong, *Optical Conductivity with Holographic Lattices*, *JHEP* **1207** (2012) 168 [1204.0519].

[86] G. T. Horowitz, J. E. Santos and D. Tong, *Further Evidence for Lattice-Induced Scaling*, *JHEP* **1211** (2012) 102 [1209.1098].

[87] G. T. Horowitz and J. E. Santos, *General Relativity and the Cuprates*, *JHEP* **1306** (2013) 087 [1302.6586].

[88] S. A. Hartnoll and J. E. Santos, *Cold planar horizons are floppy*, *Phys.Rev.* **D89** (2014), no. 12 126002 [1403.4612].

[89] A. Donos and J. P. Gauntlett, *The thermoelectric properties of inhomogeneous holographic lattices*, 1409.6875.

[90] S. A. Hartnoll, D. M. Ramirez and J. E. Santos, *Emergent scale invariance of disordered horizons*, 1504.03324.

[91] S. R. Coleman, *Q Balls*, *Nucl.Phys.* **B262** (1985) 263.

[92] A. Donos and J. P. Gauntlett, *Holographic Q-lattices*, *JHEP* **1404** (2014) 040 [1311.3292].

[93] A. Donos and J. P. Gauntlett, *Novel metals and insulators from holography*, *JHEP* **1406** (2014) 007 [1401.5077].

[94] Y. Ling, P. Liu, C. Niu, J.-P. Wu and Z.-Y. Xian, *Holographic Superconductor on Q-lattice*, *JHEP* **1502** (2015) 059 [1410.6761].

[95] T. Andrade and B. Withers, *A simple holographic model of momentum relaxation*, *JHEP* **1405** (2014) 101 [1311.5157].

[96] B. Goutéraux, *Charge transport in holography with momentum dissipation*, *JHEP* **1404** (2014) 181 [1401.5436].

[97] E. Mefford and G. T. Horowitz, *Simple holographic insulator*, *Phys.Rev.* **D90** (2014), no. 8 084042 [1406.4188].

[98] M. Taylor and W. Woodhead, *Inhomogeneity simplified*, 1406.4870.

[99] K.-Y. Kim, K. K. Kim, Y. Seo and S.-J. Sin, *Coherent/incoherent metal transition in a holographic model*, *JHEP* **1412** (2014) 170 [1409.8346].

[100] R. A. Davison and B. Goutéraux, *Momentum dissipation and effective theories of coherent and incoherent transport*, *JHEP* **1501** (2015) 039 [1411.1062].

[101] T. Andrade and S. A. Gentle, *Relaxed superconductors*, 1412.6521.

[102] R. A. Davison and B. Goutraux, *Dissecting holographic conductivities*, 1505.05092.

[103] F. Nogueira and J. B. Stang, *Density versus chemical potential in holographic field theories*, *Phys.Rev.* **D86** (2012) 026001 [1111.2806].

[104] M. Kruczenski, D. Mateos, R. C. Myers and D. J. Winters, *Meson spectroscopy in AdS / CFT with flavor*, *JHEP* **0307** (2003) 049 [hep-th/0304032].

[105] A. Karch and A. O'Bannon, *Metallic AdS/CFT*, *JHEP* **0709** (2007) 024 [0705.3870].

[106] P. W. Anderson, *Absence of Diffusion in Certain Random Lattices*, *Phys. Rev.* **109** (1958) 1492–1505.

[107] E. Abrahams, P. W. Anderson, D. C. Licciardello and T. V. Ramakrishnan, *Scaling Theory of Localization: Absence of Quantum Diffusion in Two Dimensions*, *Phys. Rev. Lett.* **42** (1979) 673–676.

[108] P. A. Lee and T. V. Ramakrishnan, *Disordered electronic systems*, *Rev. Mod. Phys.* **57** (1985) 287–337.

[109] D. Belitz and T. R. Kirkpatrick, *The Anderson-Mott transition*, *Rev. Mod. Phys.* **66** (1994) 261–380.

[110] F. Evers and A. D. Mirlin, *Anderson transitions*, *Rev. Mod. Phys.* **80** (2008) 1355–1417.

[111] C. Kristjansen and G. W. Semenoff, *Giant D5 Brane Holographic Hall State*, *JHEP* **06** (2013) 048 [1212.5609].

[112] H. Jones, *Groups, Representations and Physics*. CRC Press, 1998.

[113] H. Samelson, *Notes on Lie Algebras*. Universitext. Springer New York, 2012.

[114] H. Georgi, *Lie Algebras in Particle Physics: From Isospin to Unified Theories*. Frontiers in Physics Series. Westview Press, 1999.

Acknowledgments

Little can single individuals achieve by themselves. The completion of this doctoral thesis turned out to be more of a challenge than I had initially expected. Both at a scientific and at a personal level, difficulties were found along the way and I sincerely doubt I would have been able to overpower them, had it not been for the long list of people to whom I feel very much indebted.

I would like to thank Prof. Bartomeu Fiol, without whose encouragement, help and advice, this brief but exciting career in theoretical physics would not have ever been even considered at all.
I am most thankful to my supervisor Prof. Dr. Johanna Erdmenger for giving me the opportunity to work in her research group and supporting me in the pursue of this doctoral thesis. I am indebted to Prof. Dr. Dieter Lüst, for being my second supervisor and for providing such an unmatched environment for the exercise of theoretical physics in the lovely city of Munich. My gratitude goes to Frank Steffen for directing the IMPRS program and organising our incredible Workshops in the paradisiac Castle Ringberg. Many tanks to Monika Goldammer and Rosita Jurgeleit for being the best secretaries one can imagine: competent, nice, effective, always helpful and smiling. I am thankful that whenever my computer decided to strike for a while, Thomas Hahn was promptly able to fix it magically within seconds. I can think of no better working environment than the Max Planck Institute for Physics in Munich. A long list of technicians and people working in the building make it possible, from co-workers in the administration, to cleaning ladies and the personnel of the canteen. I am thankful for their job.

In this travel along the motivational roller coaster of a doctoral thesis, past the beauties of physics and against the head wind of frustration, I had the privilege of being accompanied among others by Andreas Deser, Charlotte Sleight, Cyril Pietsch, Daniela Herrschmann, Felix Rennecke, Hansjörg Zeller, Hendrik Vogel, Jan Keitel, Julia Stadler, Mario Flory, Mathias Weissenbacher, Maximilian Totzauer, Migael Strydom, Severin Lüst, Steffen Klug, Stephan Hassenberger, Stephan Steinfurt, and Tania Geib. It was furthermore a pleasure to epically

work alongside Daniel Areán and Javier Lizana. A special mention is in order for Max-Niklas Nerzwella and Ann-Kathrin Straub, who in addition to it all, had to put up with my presence in their office during all this time, making it much more pleasant and enjoyable. They also helped a lot by proofreading this thesis. Getting to know all these people and being given the chance to learn from them and disscus with them was for sure the most satisfactory aspect of my job as a physicist.

Ich möchte mich außerdem ganz herzlich bei all denjenigen bedanken, die dazu beigetragen haben, dass ich mich in den letzten drei Jahren weit weg von der Heimat und zugleich in der Heimat gefühlt habe. Vielen Dank an Isabelle, die immer wieder irgendwie da war. Danke auch an Sascha, dass er ob für Bergwanderungen oder spontanes Weintrinken immer zu haben war. Danke an Felix und Eva, dass sie einen dermaßen spießiegen Mitbewohner ausgehalten haben. An Herrn Dr. Manhart für die sehr erleuchtenden Gespräche und Lebensweissheiten. Danke auch an Judith, von der ich eine Menge gelernt habe.
Gràcies a l'Ana. És un plaer tenir-la a prop després dels anys. Gracias a Ignacio, por sus empeños en llevarme por el buen mal camino y por trepar conmigo a lo más alto de la autoironía.

Por último, pero sin duda alguna por encima de todo, mi agradecimiento más profundo a mi familia: a mis padres, Juan Carlos y Gloria, a mi hermano Daniel, a Laura, a mis tíos y primos. A todos ellos debo lo que soy. La certeza de tenerlos a mi lado donde quiera que esté, su cariño y apoyo incondicional y la tranquilidad del hogar al que siempre regresar son la mayor fuente de fuerza y felicidad que puede tenerse.

To each and everyone of them goes my sincerest gratitude.

Gracias.

Munich, 30th september 2015.